Micromechanical modelling of polyethylene

by

José Andrés Alvarado Contreras

A thesis
presented to the University of Waterloo
in fulfilment of the thesis requirement for the degree of
Doctor of Philosophy
in
Civil Engineering

Waterloo, Ontario, Canada, 2007

I hereby declare that I am the sole author of this thesis. This is a true copy of the thesis, including any required final revisions, as accepted by my examiners.

I understand that my thesis may be made electronically available to the public.

ABSTRACT

The increasing use of polyethylene in diverse applications motivates the need for understanding how its molecular properties relate to the overall behaviour of the material. Although microstructure and mechanical properties of polymers have been the subject of several studies, the irreversible microstructural rearrangements occurring at large deformations are not completely understood. The purpose of this thesis is to describe how the concepts of Continuum Damage Mechanics can be applied to modelling of polyethylene materials under different loading conditions.

The first part of the thesis consists of the theoretical formulation and numerical implementation of a three-dimensional micromechanical model for crystalline polyethylene. Based on the theory of shear slip on crystallographic planes, the proposed model is expressed in the framework of viscoplasticity coupled with degradation at large deformations. Earlier models aid in the interpretation of the mechanical behaviour of crystalline polyethylene under different loading conditions; however, they cannot predict the microstructural damage caused by deformation. The model, originally due to Parks and Ahzi (1990), was further developed in the light of the concept of Continuum Damage Mechanics to consider the original microstructure, the particular irreversible rearrangements, and the deformation mechanisms. Damage mechanics has been a matter of intensive research by many authors, yet it has not been introduced to the micromodelling of semicrystalline polymeric materials such as polyethylene. Regarding the material representation, the microstructure is simplified as an aggregate of randomly oriented and perfectly bonded crystals. To simulate large deformations, the new constitutive model attempts to take into account existence of intracrystalline microcracks.

The second part of the work presents the theoretical formulation and numerical implementation of a three-dimensional constitutive model for the mechanical behaviour of semicrystalline polyethylene. The model proposed herein attempts to describe the

deformation and degradation process in semicrystalline polyethylene following the approach of damage mechanics. Structural degradation, an important phenomenon at large deformations, has not received sufficient attention in the literature. The modifications to the constitutive equations consist essentially of introducing the concept of Continuum Damage Mechanics to describe the rupture of the intermolecular (van der Waals) bonds that hold crystals as coherent structures. In order to model the mechanical behaviour, the material morphology is simplified as a collection of inclusions comprising the crystalline and amorphous phases with their characteristic average volume fractions. In the spatial arrangement, each inclusion consists of crystalline material lying in a thin lamella attached to an amorphous layer. To consider microstructural damage, two different approaches are analyzed. The first approach assumes damage occurs only in the crystalline phase, *i.e.*, degradation of the amorphous phase is ignored. The second approach considers the effect of damage on the mechanical behaviour of both the amorphous and crystalline phases.

To illustrate the proposed constitutive formulations, the models were used to predict the responses of crystalline and semicrystalline polyethylene under uniaxial tension and simple shear. The numerical simulations were compared with experimental data previously obtained by Bartczak et al. (1994), G'Sell and Jonas (1981), G'Sell et al. (1983), Hillmansen et al. (2000), and Li et al. (2001). Our model's predictions show a consistently good agreement with the experimental results and a significant improvement with respect to the ones obtained by Parks and Ahzi (1990), Schoenfeld et al. (1995), Yang and Chen (2001), Lee et al. (1993b), Lee et al. (1993a), and Nikolov et al. (2006). The newly proposed formulations demonstrate that these types of constitutive models based on Continuum Damage Mechanics are appropriate for predicting large deformations and failure in polyethylene materials.

ACKNOWLEDGEMENTS

I would like to thank deeply my supervisor Dr. Maria Anna Polak for all of her guidance and support throughout this project. Also, I would like to extend a special acknowledgement to Dr. Alexander Penlidis for his support and insightful commentaries during our frequent meetings. I consider myself quite privileged to have been granted the opportunity to work under the advisement of Dr. Polak and Dr. Penlidis, who gave me nearly complete freedom concerning my research work and great support whenever I needed it.

I am grateful to the University of the Andes in Venezuela for granting me study leave and for providing most part of the financial support for completing my doctoral studies in Canada. Also, I thank my colleagues in the Department of Technology and Design of the University of the Andes for their encouragement and support during this leave. I also thank Imperial Oil Canada for their funding and support.

I want to thank my friends and everybody who has supported and helped me personally and professionally along the way. I am especially indebted to Gerardo Granado, Lorena Suárez, Celza Bonilla, Yarubí Franco, Robert (Bob) Reinhart, Rubén Chacón, Rafael Muñoz-Márquez, Marisa Ortiz, and Louann Miller for their unwavering support and great kindness all these years.

My special thanks go to my wife Mónica, I thank you so much for your patience, constant support, and encouragement which have helped me to attain this goal. *20 puntos !*. Finally, I want to thank my family for their love, motivational support, and prayers throughout this project.

To God

To Mónica and Faith

To my parents

TABLE OF CONTENTS

LIST OF FIGURES

LIST OF TABLES

CHAPTER
ONE

Introduction

1.1 Micromechanical modelling of polyethylene

Mechanical and structural components are usually subjected to complex interaction of load and environmental conditions that can cause failure. Although the number of structural failures is low, the incurred costs as well as the human and environmental consequences are considerable. There has been an increased interest in gaining insight not only into the macroscopic behaviour of materials but also into the different processes occurring at the microstructural level that may affect end-use mechanical performance.

The research presented in this thesis concerns the micromechanical modelling of the behaviour of semicrystalline polyethylene. Particularly, the study involves the development and implementation of a micromechanical model for describing the damage processes in polyethylene materials. The mechanical properties of these materials are studied considering not only the original microstructure but also the particular mechanisms activated at various steps in the plastic deformation. Since macromolecules in polyethylene materials are capable of adopting two basic arrangements, the crystalline and amorphous phases, microscopic degradation processes are modelled taking consistently into account the participation of these two regions.

The mechanical behaviour of polymers has been the subject of considerable studies in the past. An important aim of polymeric materials research consists in developing mathematical models for understanding the dependence between the various structural and morphological factors and the mechanical properties at the microscopic level. Also, of particular interest is the improvement of material processability and product performance; for instance, in industrial and medical applications.

As indicated by Budiansky (1983), the adjective *micromechanical* is commonly used to designate a class of analytical models which emphasize the relation between the macroscopic state of a material and its microstructure. Implicit to this definition is that the change of the macroscopic state of a material is related to the irreversible rearrangements of its microstructure. A precise definition of what constitutes a microstructure is dependent on the considered material, problem, scale, selected resolution and required accuracy. The microstructure of polymeric materials and its changes are, in general, non-deterministic. The same is true for the fluctuations in stresses and strains attributable to the random geometry and chemical composition of the microstructure.

The mechanical performance of polyethylene materials depends not only on operating conditions but also on many phenomena occurring at the microscopic level (*e.g.*, G'Sell and Dahoun, 1994; Lin and Argon, 1994; Schrauwen, 2003; G'Sell et al., 2002). In recent years, there has been an increasing concern in developing reliable experimental techniques and mathematical models to investigate the mechanical response of polyethylene and other polymeric materials at different length scales. This particular interest is due to the many practical applications where polyethylene in its different grades is taking the place of other materials. These applications include packing films, containers, and pipes. In a variety of studies, constitutive equations have been proposed to describe experimental observations and to predict molecular features and macroscopic properties in polymeric materials. Researchers have focussed on understanding the nonlinear behaviour of crystalline and semicrystalline polyethylene by relating microstructure with the macroscopic performance under both small (Nikolov and Doghri, 2000; Nikolov et al., 2002) and large (Cowking et al., 1968; Cowking and Rider, 1969; Keller and Pope, 1971; Young et al., 1973; Parks and Ahzi, 1990; Lee et al., 1993a; Lin and Argon, 1994; Ahzi et al., 1994; Lee et al., 1995; Argon, 1997; Hiss et al., 1999), deformations. Lee et al. (1993a,b) and Argon (1997) pioneered the micromechanically-based modelling of semicrystalline polyethylene at large deformations. Other micromechanical models accounting for the physical microstructure of kinematically constrained polycrystals have been proposed by Parks and Ahzi (1990); Ahzi et al. (1994); Lee et al. (1995); Schoenfeld et al. (1995); van Dommelen et al. (2000). Although these existing constitutive models are able to predict the mechanical behaviour of polyethylene partially, to our knowledge, researchers have not investigated the application of Continuum Damage Mechanics Theory (*e.g.*, Rabotnov, 1969; Kachanov, 1986; Lemaitre, 1996) to this problem.

1.2 Objectives and scope

The object of this thesis is twofold. First, the thesis is concerned with the development and numerical implementation of a damage model for crystalline polyethylene. Second, it is related to the introduction of a damage-coupled constitutive model for describing the links between the microstructural degradation processes and the macroscopic stress-strain response of semicrystalline polyethylene.

The goal of the first part of the thesis is to consider damage and texture evolution related to deformation by chain and transverse slip in idealized 100% crystalline polyethylene. To simulate large deformation, the micromechanical model proposed earlier by Parks and Ahzi (1990) is modified to take into account the effects of atomic debonding on the overall mechanical behaviour, neglecting the contribution from the amorphous phase. This part is devoted to the following aims:

1. Description of a constitutive law for the mechanical behaviour of crystalline polyethylene using concepts from Continuum Damage Mechanics
2. Implementation of the model into a computer program
3. Estimation of the material parameters using information available in the literature
4. Numerical solution of uniaxial tension and simple shear cases to predicting (1) the macroscopic behaviour and typical stress-strain curves, (2) the damage accumulation at the different stages of deformation, and (3) the influence of damage on texture evolution of the different slip systems
5. Comparison of the model results with those obtained numerically by Parks and Ahzi (1990) and Yang and Chen (2001), and experimentally by Hillmansen et al. (2000) and G'Sell et al. (1983)

In the second part, a damage-coupled model for the amorphous polyethylene material is considered. The constitutive equations are developed using the incompressible non-Gaussian network theory and Arruda and Boyce's (1993) eight-chain model. The microscopic deterioration of a representative volume element is modelled considering an isotropic damage variable. The evolution of this variable is linked to the evolution of the deformation and growth processes of small voids (volume discontinuities in the form of cavities) in the amorphous polymer material.

Once the micromechanical constitutive equations for the crystalline and amorphous phases have been developed, a damage model for composite inclusion is proposed.

The improved model takes into account the fact that the presence of crystallites confines the amorphous phase. Additionally, the micromechanical model should not only be able to reproduce the mechanisms of deformations and texture evolution in semicrystalline polyethylene but also to give physical insight into the damaged microstructure of this material. In this part, the work involves:

1. Description of a model based on Continuum Damage Mechanics for the amorphous phase of semicrystalline polyethylene
2. Development of the combined behaviour model for both crystalline and amorphous phases in a composite inclusion
3. Description of (1) the compatibility and traction equilibrium conditions on the interface of the composite inclusion, and (2) the local-global inclusion interaction law that relates the mechanical behaviour of each composite inclusion to the imposed boundary conditions for an aggregate of inclusions. Implementation of the homogenization technique.
4. Numerical implementation of the constitutive equations
5. Numerical simulation of uniaxial tension and simple shear problems to evaluate the composite model
6. Comparison of the model results with those obtained by Lee et al. (1993b) and Nikolov et al. (2006)

1.3 Contributions of the thesis

The overall research effort of the thesis focuses on two major topics containing the following original work:

1. The theoretical formulation and numerical implementation of a three-dimensional micromechanical model for crystalline polyethylene (no amorphous phase considered). Based on the theory of shear slip on crystallographic planes, the proposed model is expressed in the framework of viscoplasticity coupled with degradation at large deformations. Earlier models aid in the interpretation of the mechanical behaviour of crystalline polyethylene under different loading conditions; however, they cannot predict the microstructural damage caused by deformation. The model, originally due to Parks and Ahzi (1990), was further developed in the light of the concept of Continuum Damage Mechanics to consider the original microstructure,

the particular irreversible rearrangements, and the deformation mechanisms. Damage mechanics has been a matter of intensive research by many authors, yet it has not been introduced to the micromodelling of semicrystalline polymeric materials such as polyethylene. Regarding the material representation, the microstructure is simplified as an aggregate of randomly oriented and perfectly bonded crystals. To simulate large deformations, the new constitutive model attempts to take into account existence of intracrystalline microcracks. The following journal and conference papers show the novel contributions to the modelling of polyethylene: Alvarado-Contreras et al. (2005, 2006a,b, 2007a,e)

2. The theoretical formulation and numerical implementation of a three-dimensional constitutive model for the mechanical behaviour of semicrystalline polyethylene (both crystalline and amorphous phases). In this part of the work, the model attempts to describe the deformation and degradation process in semicrystalline polyethylene following the approach of damage mechanics. Structural degradation, an important phenomenon at large deformations, has not received sufficient attention in the literature. The modifications to the constitutive equations consist essentially of introducing the concept of Continuum Damage Mechanics to describe the rupture of the intermolecular (van der Waals) bonds that hold crystals as coherent structures. In order to model the mechanical behaviour, the material morphology is simplified as a collection of inclusions comprising both the crystalline and amorphous phases with their characteristic average volume fractions. In the spatial arrangement, each inclusion consists of crystalline material lying in a thin lamella attached to an amorphous layer. To consider microstructural damage, two different approaches are analyzed. The first approach assumes damage occurs only in the crystalline phase, *i.e.*, degradation of the amorphous phase is ignored. The second approach considers the effect of damage on the mechanical behaviour of both the amorphous and crystalline phases. Papers currently under review (with abstracts) or in preparation for presenting the proposed model for semicrystalline polyethylene include: Alvarado-Contreras et al. (2007c,b,d, 2008)

1.4 Chapter contents

The present thesis is divided into eight chapters. The first part, comprising *Chapters* 2 and 3, is the exposition and development of the fundamentals of micromechanical modelling

of polymeric materials. The following four chapters present the proposed models and details of the numerical implementation. The last chapter summarizes the conclusions. In detail, the thesis is organized as follows:

Chapter 2 introduces a literature review of the physical-chemical structure of semicrystalline polyethylene. The chapter provides a brief summary of the molecular weight distribution, thermoplastic and thermosetting behaviour, and types of polyethylene materials. Aspects of the mechanics of deformation in crystalline and amorphous phases of polyethylene are also presented.

Chapter 3 reviews the models developed to date for describing the micromechanical behaviour of polyethylene materials. Different models for predicting small and large deformations in semicrystalline polyethylene and large deformations in idealized 100% crystalline polyethylene are introduced.

Chapter 4 describes how the concepts of Continuum Damage Mechanics can be applied to modelling of crystalline polyethylene. The material is analyzed from a microscopic viewpoint and considered as an aggregate of crystals. The model regards the crystals as rigid-viscoplastic and incorporates the effects of atomic debonding on the overall mechanical behaviour. To illustrate the capability of the proposed model, two simulations are carried out to capture the macroscopic stress-strain behaviour and texture evolution under uniaxial tension and simple shear loading conditions. The results are compared with experimental data and numerical simulations from other references.

Chapter 5 presents the numerical implementation of the model proposed for crystalline polyethylene, as well as, a study on the influence on the model performance of the assumptions regarding aggregate size, crystal orientations, and material parameters. Consequently, a detailed explanation of the algorithms and a general description of material modelling in terms of microstructure evolution are given.

Chapter 6 concentrates on the modelling of semicrystalline polyethylene at large deformations. Using damage-coupled models for the crystalline and amorphous phases, the main challenge within this chapter is the prediction of mechanical behaviour of semicrystalline polyethylene considering a more detailed description of the complex microstructure and of the degradation processes occurring in the material. Uniaxial tension and simple shear cases are solved numerically using the proposed constitutive model and the results are compared against experimental and numerical data found in the literature.

Chapter 7 contains the description of the algorithms used for modelling the semi-

crystalline material. Additionally, some of the model parameters are analyzed to gain insight into their influence on the stress state and damage evolution.

Chapter 8 presents the major conclusions of the present research work, discusses the main contributions, and suggests some recommendations for future research.

1.5 Notation

For simplicity, equations are written using index notation (*e.g.*, Malvern, 1969). By means of the range convention, vectors can be expressed as v_i, where the index i labels the coordinate directions 1, 2, and 3. Second- and fourth-order tensors such as stresses and compliances are respectively written as σ_{ij} and M_{ijkl}, where all the indexes range from 1 to 3 to give correspondingly nine and 81 components. In the expressions, we use the Einstein summation convention, where a repeated index implies summation over the index range. Therefore, the product rules for tensors can be written as $A_{ij} = b_i\, c_j$ (tensor product), $A_{ij} = B_{ik}\, C_{kj}$ (inner product), and $A_{ij} = B_{ijkl}\, C_{lk}$ (double inner product). Additionally, the volume average of a quantity and the inverse of a tensor are given as $\langle \bullet \rangle$ and $(\bullet)^{-1}$, respectively. Other notations are defined as they appear in the sections.

CHAPTER
TWO

Structure and plastic deformation of polyethylene

2.1 Introduction

Polymers are materials made of large molecules, and they can be shaped into a variety of products. The molecules that compose polymers are long hydrocarbon chains that give them many of their useful mechanical and chemical properties (Andrews, 1972). Polyethylene represents one of the most important polymeric materials which has now become ever-present in applications in modern life. The first part of this chapter is principally concerned with the physical and chemical structures, molecular weight distributions, thermoplastic and thermosetting behaviour, and types of semicrystalline polyethylene. Likewise, some aspects of the mechanisms of deformation in the crystalline and amorphous phases of polyethylene are presented.

2.2 Structure of polyethylene

Polymers, from the Greek words *poly* and *mer* meaning *many* and *part*, respectively, are substances consisting of macromolecules made of many small units or monomers chemically joined end to end. Polyethylene, the simplest hydrocarbon polymer, is a macromolecular solid in which the molecular units are long chain-like molecules with carbon and hydrogen atoms forming a zigzag arrangement along a backbone, as shown in *Figure* 2.1. In polyethylene chains, the monomer unit is an ethylene (C_2H_4 or $CH_2 = CH_2$), a colourless gas composed of two double-bonded carbon atoms and four hydrogen atoms. A typical polyethylene molecule may contain from hundreds to millions of these monomers (Young, 1981).

The most elemental structure of any polyethylene material is a linear long chain. In a chain, carbon atoms are covalently bonded[1] together using two of their four bonds per atom; the remaining bonds are covalently shared with two hydrogen atoms. Another type of bond is the *van der Waals bonding*, which is attributed to the attraction that all molecules have for each other (Coulombic attraction). Van der Waals forces are dependent upon molecule masses and distances. Since molecules are so small, van der Waals attractions occur at very short distances; even then, these forces are quite weak and several times lower than those corresponding to covalent bondings.

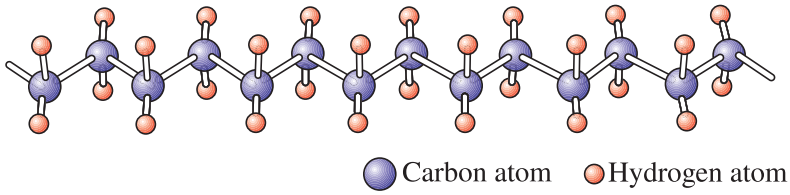

Figure 2.1: Segment of a polyethylene molecule showing the zigzag backbone structure.

The chemical reaction in which macromolecules are made is known as *polymerization*. One of the most common types of polymerization is the *chain-growth polymerization*. It is a three-step process involving two chemical species, as shown in *Figure* 2.2. The first species is an ethylene monomer, added in high concentration. The other species is a catalyst or initiator, which starts the polymerization reaction. It is added in relatively low concentrations and under appropriate conditions of temperature and pressure. A common catalyst is a peroxide (R_2O_2), which is a molecule or functional group[2] containing an oxygen-oxygen single bond. In the peroxide polymerization of ethylene, the oxygen-oxygen bond with a bond enthalpy[3] of 146 kJ mol^{-1} decomposes before the carbon-carbon (348 kJ mol^{-1}) or carbon-hydrogen (412 kJ mol^{-1}) bonds to form a pair of free-radicals (electrons), denoted by • in *Figure* 2.2. The first step, *initiation*, occurs when a free-radical reacts with an ethylene monomer and initiates the chain. The double carbon-carbon bond in an ethylene monomer breaks apart and pairs up to the free-radical. The other radical site is transferred to the terminal carbon atom, so one free-radical leads to

[1]Two atoms that are covalently bonded will each other contribute at least one electron to the bond. The shared electron is considered to belong to both atoms.
[2]Functional groups are specific groups of atoms within molecules responsible for the characteristic chemical reactions of those molecules.
[3]The bond enthalpy is the energy required to break a chemical bond, and is usually expressed in units of kJ mol^{-1} and measured at 298 K.

another with a monomer unit attached to it. The next step, *propagation*, is a repetitive operation in which the growing chain is formed. The double bonds of successive ethylene monomers are opened up as they are added to the reactive polyethylene radical chain. The free electrons are successively passed to each ethylene end as they are linked to the growing chain. The last step, *termination*, occurs after the addition of many ethylene units when two radical chains pair up together. Because chains quickly become so long, the presence of initiator fragments on chain ends has no influence on material properties. Polymer chains with only one type of monomer, as the case explained herein, are known as *homopolymers*. On the other hand, the resulting polymer is called *copolymer* when its molecules are made of two or more different species, arranged into diverse configurations or patterns along the chains.

2.2.1 Polyethylene chemical structure

Polyethylene properties depend not only on overall chain lengths, but also on the way monomers are ordered along chains. Depending on the polymerization conditions such as temperature, pressure, and catalyst type, monomers in a polymer can be arranged in a number of different ways: *linear*, *branched*, or *crosslinked*, as illustrated in *Figure* 2.3. Linear polymers are made up of long continuous chains without any side attachments; that is, mer units are joined together end to end in single chains. Branched polymers have a chain structure that consists of chain molecules with side molecular chains branching from them. In polyethylene, branching may occur by the replacement of some of the hydrogen atoms by covalently bonded polyethylene chains. A branched structure tends to increase the tie-molecule density (Butler et al., 1997). The concept of a tie-molecule will become clear in the following subsection. Crosslinked polymers occur when linear chains are joined to one another at various positions by covalent bonds (Horie et al., 2004), forming three-dimensional network-type molecules (Jenkins et al., 1996). This process is accomplished by breaking molecule bonds through a radiation-, chemical-, or silane compound-induced crosslinking method (Lewis, 2001).

2.2.2 Polyethylene physical structure

When a polyethylene melt cools, molecules arrange themselves into two distinct physical structures: *crystalline* and *amorphous*. The two phases are chemically indistinguishable from each other; however, they form separate discrete regions. Because polyethylene

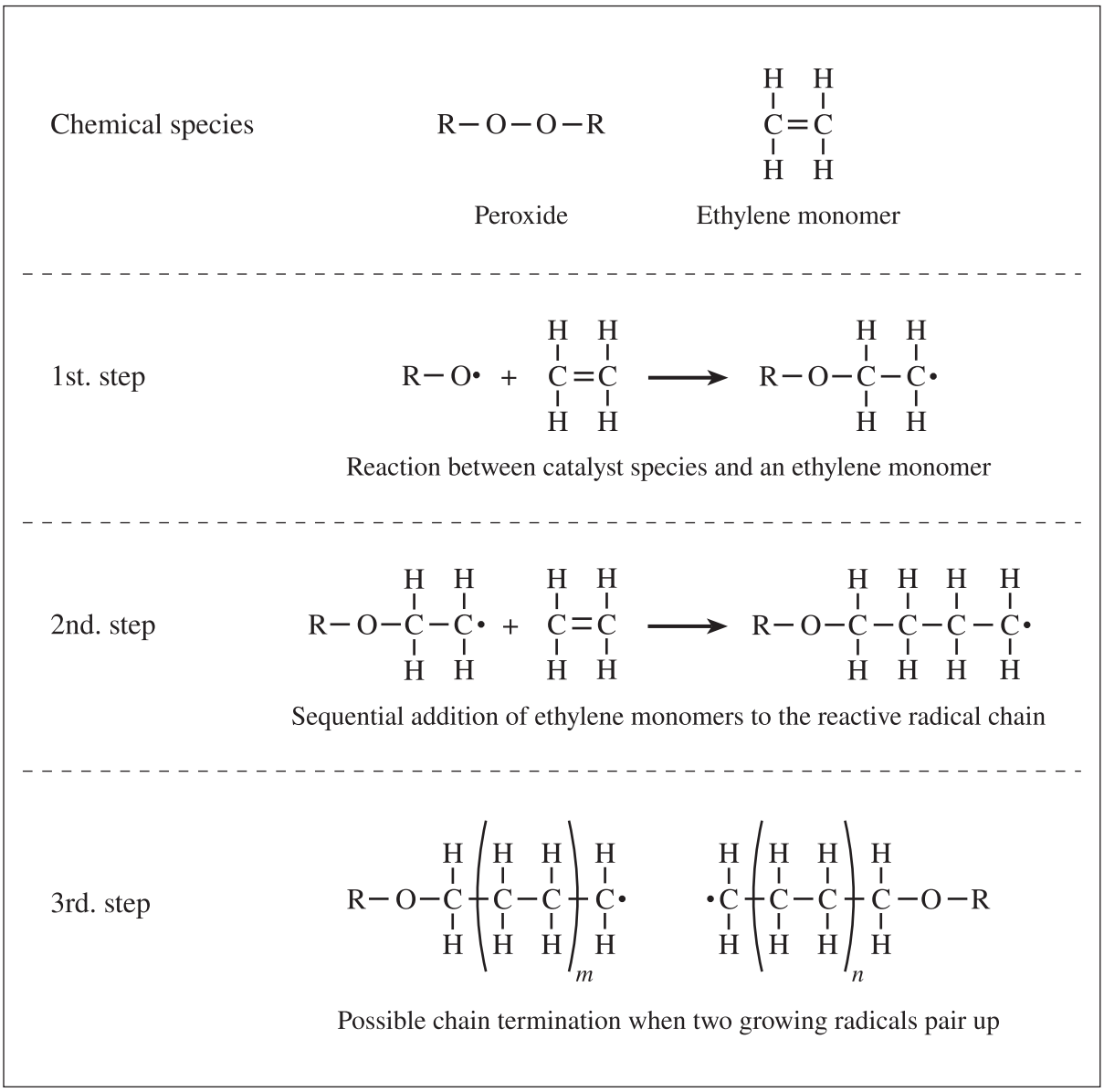

Figure 2.2: Possible polymerization scheme for ethylene.

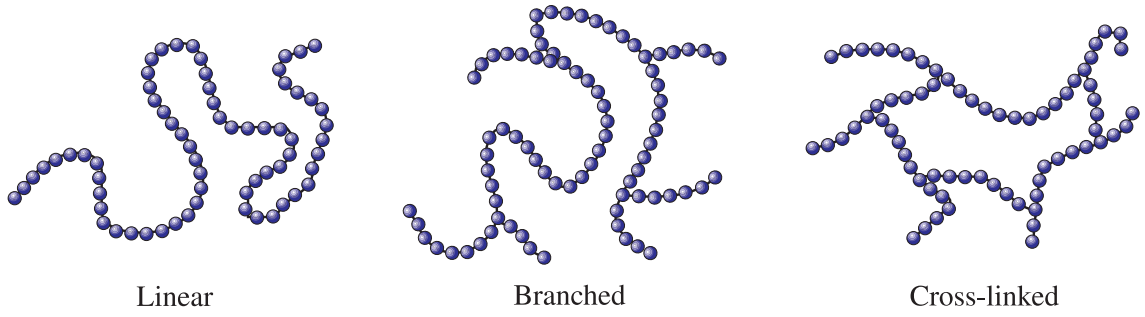

Figure 2.3: Schematic representation of linear, branched, and crosslinked molecular structures.

contains both phases, it is known as a *semicrystalline polymer*. The crystalline phase, embedded within amorphous material, is only possible if chains adopt highly ordered and aligned arrangements. These structures form thin lamellae with thickness orders of magnitude smaller than extended chain dimensions. Crystallinity is favoured in symmetrical and linear polymer chains; however, it is never completely present. The amorphous phase consists of anisotropic and highly entangled molecules, which could not be resolved during the crystallization process. The entanglements and lamellae adjacent to the amorphous material form the physical crosslinks of the network (Brady and Thomas, 1989).

Polyethylene crystals form by folding molecules alternately up and down and by arranging the straight segments between folds into periodic arrays. Consequently, crystalline regions are denser than amorphous ones. Lamella thicknesses range from 20 to 170 Å, and lateral dimensions are from one to 50 μm long. Straight segments between folds may include only few tens of monomers (Lin and Argon, 1994). The structure of polyethylene crystals is orthorhombic, as shown in *Figure* 2.4. The lengths a=7.41 Å, b=4.94 Å, and c=2.55 Å are the lattice parameters of the polyethylene crystal, where the c-axis is parallel to the main molecule axis (Bunn, 1944, 1954).

Locally, crystalline and amorphous phases are packed together forming spherulitic structures, as the one shown in *Figure* 2.5a. A spherulite consists of several lamellae growing along the b-axis. Lamellae are separated by layers of amorphous material and bound together by the so-called *tie-molecules*, as shown in *Figure* 2.5b. Tie-molecules are chains long enough to run through several neighbouring lamellar and amorphous regions, giving the required cohesiveness to prevent the two phases from separating under loading (Brown and Ward, 1983). Two more different molecular morphologies have

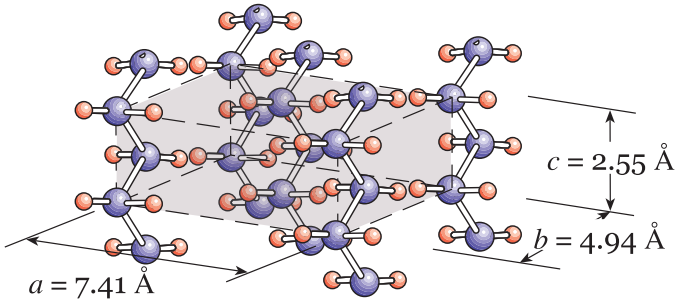

Figure 2.4: An orthorhombic polyethylene crystal (Keller, 1968).

been identified experimentally, known as *loose loops* and *cilia*, shown also in *Figure* 2.5b. A loose loop is a molecule with both ends within the same lamella and the central part in the amorphous material. On the other hand, a cilium is a short chain with one end within a lamella and the other one in the amorphous material. Apparently, none of these two morphologies contributes significantly to increasing entanglement density or material strength.

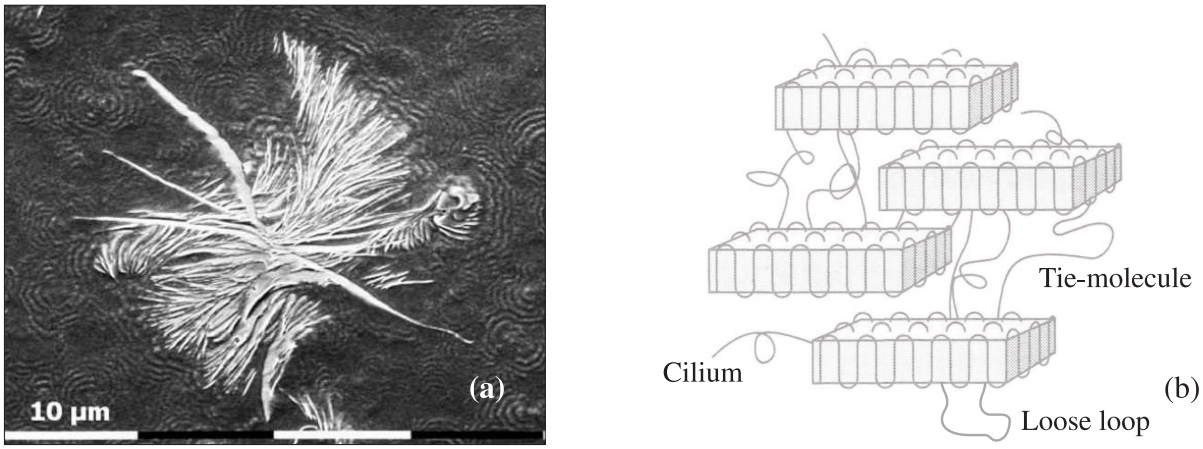

Figure 2.5: (*a*) Polyethylene spherulite in the undeformed state (Lee et al., 2003) and (*b*) different interlamellar molecules (adapted from Callister, 1996)

2.2.3 Molecular weight distribution

Unlike other chemical compounds, polymers do not have a unique molecular weight, but rather, a distribution of molecular weights. Depending on the way a polymer is produced, the resulting molecules differ not only in degree of branching or composition, but

also in molecular weight. A *molecular weight distribution* denotes the statistical distribution of molecule weights in a material and characterizes the number or weight of chains with n repeating monomers. Molecular weight distributions can be *narrow*, *broad*, *skewed*, or *multi-modal*, as illustrated in Figure 2.6. When closely grouped around some mean molecular weight, the distribution is termed narrow. A greater dispersion of weights around the average indicates a broader distribution. A skewed distribution is an unequal distribution of heavier or lighter molecules to either side of the average. Modality is an indication that there is more than one classes of molecular weight in the distribution. Materials with two classes are bi-modal, and those with multiple classes are multi-modal. The molecular weight distribution has a considerable impact on the mechanical properties of polymers (*e.g.*, Popov and Bal'tenas, 1974; Perkins et al., 1976; Rennie, 1997; Carr et al., 1998). For instance, at low molecular weights, mechanical strengths can be so low that the material is not suitable to carry loads. On the other hand, at high molecular weights, strengths increase up to certain saturation values beyond which material processability becomes extremely difficult (*e.g.*, Capaccio and Ward, 1975; Nichetti and Manas-Zloczower, 1999).

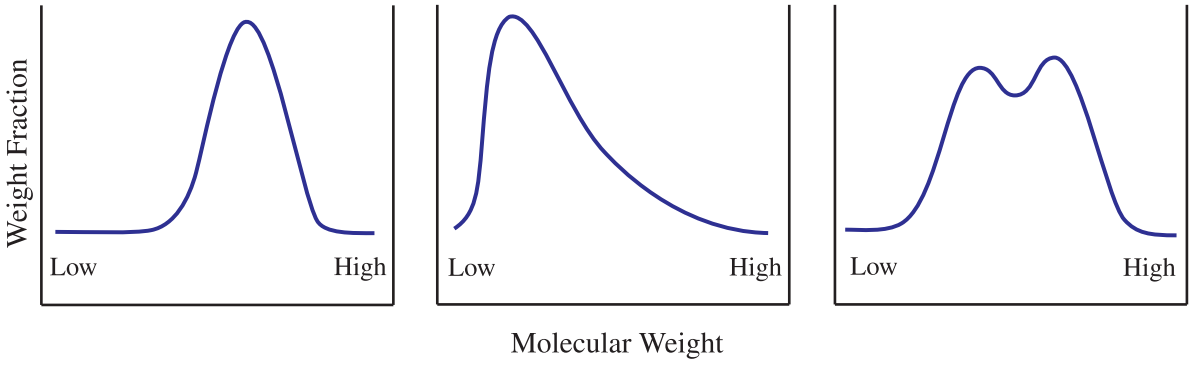

Figure 2.6: Typical molecular weight distributions: narrow, skewed, and bimodal.

2.2.4 Thermoplastic and thermosetting behaviour

Depending on their behaviour at elevated temperatures, polymers can be separated into two different groups: *thermoplastics* and *thermosettings*. Thermoplastic polymers are substances that can withstand many melting and solidifying cycles with only minimal degradation of their properties after each cycle. This characteristic makes thermoplastics suitable for remoulding and reuse. Molecules in thermoplastic polymers are linear or slightly

branched, but not crosslinked. On the other hand, thermosetting polymers are substances that harden permanently and do not soften under heat. The molecular structure is crosslinked through covalent bonding, creating a permanent network where only limited chain entanglements and vibrational chain motion occur at elevated temperatures, but flow or melting are not possible (Acharya and Bassani, 2000). Thermosetting polymers may exhibit some softening upon temperature increases, but cannot be remoulded because they just decompose or burn when heated. As expected, thermoset materials are generally stronger than thermoplastic materials.

2.2.5 Low- and high-density polyethylene

Polyethylene can be categorized as a family of similar materials made in low- and high-density forms. According to the American Society for Testing and Materials (ASTM), polyethylene materials can be classified into four distinct types; however, polyethylene manufacturers use different material designations based mostly on density or molecular weight, as shown in *Table* 2.1

Table 2.1: ASTM and industrial polyethylene density-based classification.

	ASTM		Industrial
Type	**Density**	**Terminology**	**Acronym**
I	0.910 - 0.925	low	ULLDPE, LLDPE, LDPE
II	0.926 - 0.940	medium	MDPE
III	0.941 - 0.959	high	HDPE
IV	0.960 and above	high - homopolymer	HMWPE, UHMWPE

Low-density polyethylene (LDPE), the first synthesized polyethylene, is made by a high pressure process using a free-radical initiator (oxygen or a peroxide). Its molecules have long side chain branches on 1.5 to 2.5 percent of the carbon atoms. Thus, the structure is predominantly amorphous with crystallinity as low as 45 percent, and a density ranging from 0.91 to 0.93 g/cm^3. LDPE is the most widely used of all plastics, because of its low manufacturing costs and good performance. It is flexible, tough, and chemically-resistant and is mostly used in food and industrial packaging (Pickover,

1983). *Medium-density polyethylene* (MDPE), produced either by low- or high-pressure, has average densities from 0.93 to 0.94 g/cm^3 and is from 70 to 90 percent crystalline. It is produced by chromium-silica, metallocene, or Ziegler-Natta catalysts. This material is extensively used in gas and water pipes. *High-density polyethylene* (HDPE) is made by Ziegler-Natta catalysts at lower pressures and moderate temperatures. Molecules in HDPE have a linear structure (700 to 1,800 monomer units per molecule) with very few short branched chains. As a result, molecules align into more compact arrangements with 70 to 90 percent crystalline regions, and the material has densities of 0.94 g/cm^3 and above. HDPE is stiffer, stronger, abrasion resistant, and less translucent than low- and medium-density polyethylene. HDPE is formed into grocery bags, blow-moulded household and industrial bottles, injection-moulded food containers, high performance piping, and other durable and disposable goods.

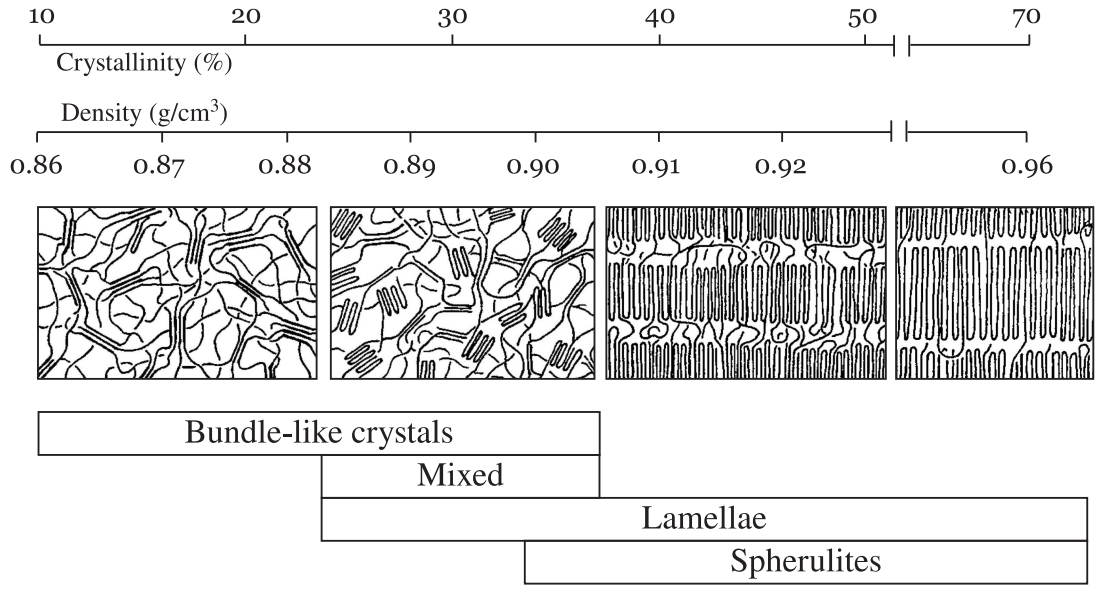

Figure 2.7: Crystal structure classification of polymers (Bensason et al., 1996).

Existing technology allows making closely related polyethylene materials with properties between LDPE and HDPE, but improved molecular weight or branching type specifications. The most used materials are: *ultra low-density polyethylene* (ULDPE), *linear low-density polyethylene* (LLDPE) (Kim et al., 1992), *high molecular weight polyethylene* (HMWPE), *ultra high molecular weight polyethylene* (UHMWPE) (Kim et al., 1992; Lewis, 2001), *crosslinked polyethylene* (PEX) and *high density crosslinked polyethylene* (HDXLPE). For instance, ULDPE and LLDPE are made by a conventional Ziegler-Natta process; how-

ever, molecules show longer and more branches than HDPE. These materials are about 50 percent crystalline with densities lower than 0.915 g/cm^3 (Dohrer et al., 1988). This results in a soft, flexible, and strong material for a wide range of temperatures. The main applications are containers, coatings, wraps packaging, and wire sheaths. UHMWPE, also known as high modulus or high performance polyethylene, has molecular weights ranging in the millions (3-6 million) and a highly crystalline structure (close to 85%). Its outstanding toughness and chemical and wear resistance make the material excellent for applications such as machinery parts, bearings, gears, artificial joints (Kurtz, 2004), among others. The product can easily be recycled.

Figure 2.7 shows the arrangements of the crystal lamellae at different density levels. When density increases, stiffness, hardness, and strength also increases. Increases in these mechanical properties are usually considered beneficial for some purpose, but increasing density also has some drawbacks. For instance, by increasing density, the polymer material becomes less ductile, more sensitive to impact, and more sensitive to cracking; no desired characteristics for some practical applications.

2.3 Plastic deformation of polyethylene

Deformation is one of the key phenomena altering the mechanical properties of semicrystalline polyethylene (Kasatkin and Grinyuk, 1968; Hobeika et al., 2000), because of the microstructural changes it induces. Deformation depends not only on the loading conditions, but also on the material morphology. The elastic and inelastic behaviour of polyethylene have been the subject of several experimental and numerical studied on the macro- and micro-scales. At the macroscopic scale, for instance, a typical stress-strain curve for uniaxial tension at room temperature shows three major deformation regions, as illustrated in *Figure* 2.8. First, the material exhibits a linear elastic behaviour. Under increasing loading, the initial reversible response eventually gives way to an inelastic behaviour. At the beginning of this region, the stress remains more o less constant despite the large deformations. At the end, the stress rises abruptly under limited deformation before the material fails.

At the microscopic scale, deformation mechanisms are different for the crystalline and amorphous phases. The elastic deformation of semicrystalline polyethylene at room temperature is related to the reversible changes in the equilibrium interatomic and intermolecular distances. On the other hand, the inelastic response begins with deformation

of the amorphous component, as shown in *Figure* 2.8. At low strain, amorphous regions carry less stress and deform considerably more rapidly than crystallites. The deformation mechanisms in the amorphous regions are a combination of interlamellar sliding and separation. As deformation progresses, the amorphous phase hardens due to network locking, and the crystalline phase starts deforming by various crystallographic processes up to large inelastic strains. Because of continuity conditions, deformation mechanisms acting in the amorphous regions must continue to occur as crystalline lamellae deform simultaneously. After a certain deformation level, the molecular network cannot be pulled out any further, and lamellae start to break up gradually into mosaic blocks. One of the most notorious differences between the behaviour of the two phases is that deformation of the amorphous regions is partially reversible, while no evidence of reversibility has been found in the lamellae at room temperature (Bartczak et al., 1992b,a).

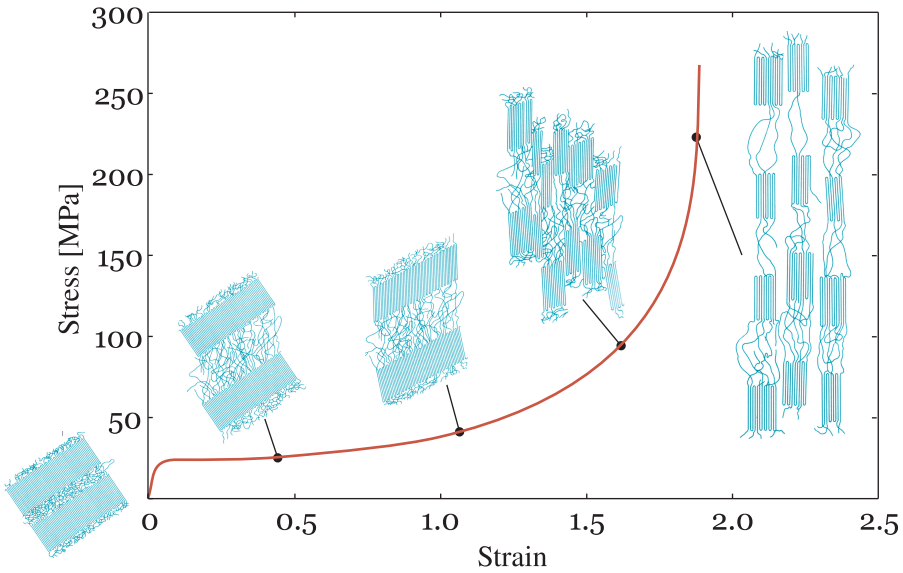

Figure 2.8: Typical stress-strain curve and the corresponding microstructural changes for a uniaxial loading case.

2.3.1 Deformation of crystalline lamellae

The network stretching is accompanied by characteristic changes in the texture and fragmentation of the original lamellae. As mentioned before, lamellae are tightly bound by tie-molecules to some of their neighbouring ones. When a spherulite deforms, lamellae develop texture along certain slip systems, becoming preferentially oriented relative to

the loading direction. The observed inelastic deformation mechanisms in polyethylene crystallites involve predominantly *crystallographic slip* and, to a lesser degree, *twinning* and *stress-induced martensitic transformations* (*e.g.*, Bowden and Young, 1974; Argon, 1997). When constraints imposed by the local neighbourhood permit, slip can result in larger levels of inelastic deformation than any other mechanism (*e.g.*, Krause and Hosford, 1989; Bartczak et al., 1992a,b, 1994, 1996a). Sets of two vectors are used to identify the available slip systems; a normal and a tangential vector representing the *slip plane* (*hkl*) and *slip direction* [*uvw*], respectively. The slip plane is the crystallographic plane along which gliding takes place. The nature of the material requires that the most preferred slip planes contain the molecular chains. The slip direction is the direction in the slip plane in which deformation occurs.

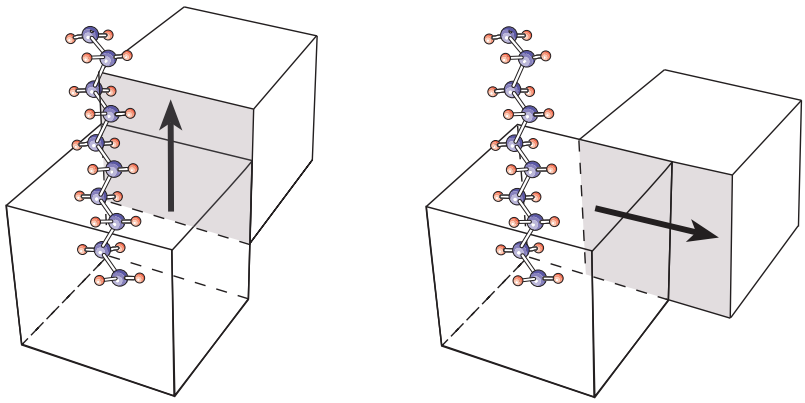

Figure 2.9: Crystal deformation mechanisms by (left) chain and (right) transverse slip.

Two slip categories operate in the orthorhombic unit cell of polyethylene crystals; these are, the *chain* and *transverse* slip systems, as shown in *Figure* 2.9. Crystal deformation by chain slip involves a translation of molecules past each other parallel to the chain direction. It follows that the chain slip systems are given by (100)[001], (010)[001], and {110}[001], as illustrated in *Figure* 2.10. On the other hand, transverse slip involves the sliding of molecules over each other in a direction perpendicular to the chain axes. Experiments carried out on polyethylene materials have established that transverse slip occurs in the (100)[010], (010)[100], and {110} $\langle 1\bar{1}0 \rangle$ slip systems (*Figure* 2.10). Chain slip and transverse slip can occur simultaneously on a common slip plane.

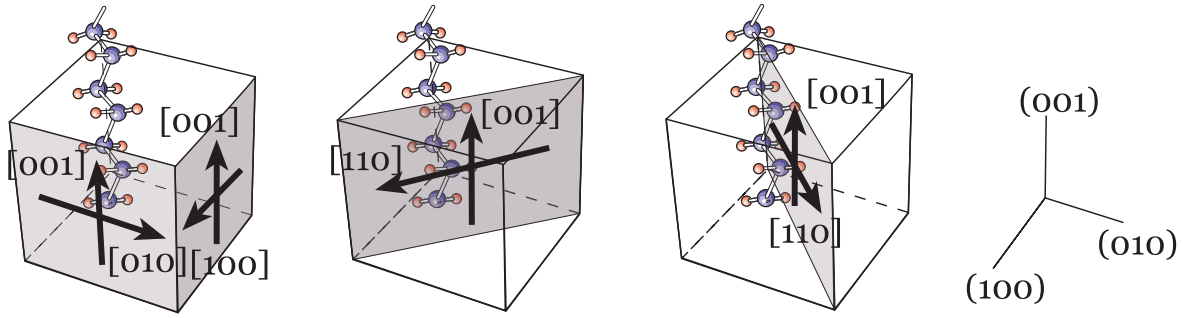

Figure 2.10: Slip systems in a polyethylene crystal.

Before transferring the material into a fibrillar morphology[4] (Peterlin, 1971), lamellae can experience large stresses along the chain directions, and crystals can react with two distinct distorting structural changes: *twinning* (Frank et al., 1958) and *martensitic transition* (Yamada et al., 1971); however, experiments have shown no evidence for the occurrence of twinning or martensitic transformation in anything more than trace amounts and at very late stages of deformation (*e.g.*, Bartczak et al., 1992a,b, 1994, 1996a; Galeski et al., 1992).

Twinning may occur in polymer crystals if the crystal structure is of sufficiently low symmetry. In polyethylene crystals, the two basic twinning modes expected to occur are the {310} and {110}. The {110} twinning mode produces a rotation of the lattice by -67° about ⟨001⟩; whereas the {310} one rotates the lattice by 55° about ⟨001⟩ (Bevis and Crellin, 1971). Martensitic transformations occur as crystals change from orthorhombic to monoclinic (Russell et al., 1997). This deformation mechanism happens only in certain crystal orientations and leaves the crystal's chains inextensible.

2.3.2 Deformation of amorphous layers

For the morphology of a crystalline-amorphous material held together by tie-molecules, three modes of interlamellar deformation have been identified experimentally: *interlamellar shear*, *interlamellar separation*, and *lamella-stack rotation*. These deformation mechanisms, and hence the associated strengths, depend upon the detailed material structure; including the number and distribution of active tie-molecules and the lateral dimension of lamellae. These modes are also nearly reversible, which is consistent with the hypothesis

[4]Transformation process at the late stage of deformation in which molecules align along the loading direction after lamella fragmentation and just before rupture.

that tie-molecules should become extended with straining and tend to return to their coiled geometries once stresses are released (Bowden and Young, 1974).

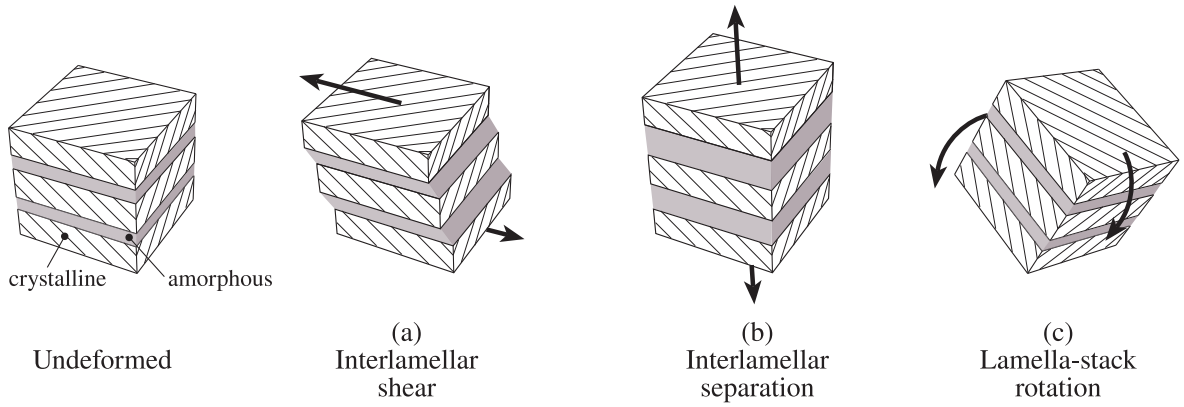

Figure 2.11: Deformation modes in amorphous phase.

Deformation by interlamellar shear (*Figure* 2.11a) involves simple shear of the interlamellar material with the shear direction being parallel to lamellae. This process results in a gradual alignment of molecules along the shear direction. When compared with other deformation modes, interlamellar shear is the easiest mechanism to activate in the early phase of straining at room temperature (Cowking and Rider, 1969; Keller and Pope, 1971). Interlamellar separation (*Figure* 2.11b) refers to changes on the interlamellar spacing. In bulk, the amorphous material has to flow into the interlamellar gaps; otherwise, large density changes in the form of crazing occur (Lin and Argon, 1994). Besides the rubbery-like behaviour, reversibility is also governed by the residual stresses resulting from the block-like relative displacements of lamellae. In contrast, irreversible interlamellar separation is associated with voiding or interlamellar rupture due to the stress component normal to the lamellae. As shown in *Figure* 2.11c, lamellae, in the form of stacks, are free to rotate in a process similar to flow alignment, and the surrounding amorphous material is able to take up any distortion caused by deformation. Lamella rotation is geometrically necessary in the overall kinematics of deformation and does not constitute an independent mechanism (Bowden and Young, 1974; Lin and Argon, 1994).

CHAPTER
THREE

Existing micromechanical constitutive models for the behaviour of polyethylene

3.1 Introduction

Significant progress has been made in both experimental and modelling aspects of the nonlinear behaviour and deformation mechanisms of polyethylene materials. There are a number of articles dealing with experimental observations and testing methodologies for polyethylene to understand the links between its molecular and macroscopic properties, using mostly small- and wide-angle X-rays. Extensive reviews and references can be found in Cowking et al. (1968), Keller (1968), Cowking and Rider (1969), Keller and Pope (1971), Young et al. (1973), Bowden and Young (1974), Bartczak et al. (1992a,b, 1994, 1996a,b), Lin and Argon (1994), Argon (1997), Hiss et al. (1999), Bartczak (2002, 2005a,b), Galeski and Bartczak (2003), Lee et al. (2003), Bartczak and Kozanecki (2005), Bartczak and Lezak (2005), Argon et al. (2005), among others. Likewise, relatively recent attempts to model semicrystalline polymeric materials as well as their crystalline and amorphous phases have been reported in Parks and Ahzi (1990, 1991), Ahzi et al. (1994), Lee et al. (1995), Schoenfeld et al. (1995), Tomita et al. (1997), Ahzi (1999), Tomita (2000), Nikolov and Doghri (2000), Nikolov et al. (2002), van Dommelen et al. (2000, 2003b,a, 2004), Tomita and Uchida (2003), Nikolov et al. (2006), and van Dommelen et al. (2007). In these publications, different constitutive formulations for small and large deformation behaviour from a microscopic viewpoint using either elasto- or rigid-viscoplastic frameworks are proposed. Even though these models aid in the interpretation of structural observations under different loading conditions, no specific attention is given to the degradation processes taking place in the material microstructure (*e.g.*, G'Sell and Dahoun, 1994; G'Sell

et al., 2002). The aim of this chapter is to present the general ideas behind the most cited micromechanical models proposed for describing the behaviour of polyethylene.

3.2 Large deformation models

Microstructure-based modelling of polyethylene faces the challenge of efficiently representing the properties and interplays of crystalline and amorphous regions. Much research has been focused on understanding the viscoplastic behaviour of semicrystalline polymers by relating the macroscopic behaviour to the morphology. In the following sections, a summary of the models proposed to date for describing the micromechanical behaviour of polyethylene in large deformation is given.

3.2.1 Idealized 100% crystalline models

Micromechanical models accounting for the physical microstructure of kinematically constrained polycrystals (Groves and Kelly, 1963; Cotton and Kaufman, 1991) have been proposed by Parks and Ahzi (1990), Ahzi et al. (1994), Lee et al. (1995), Schoenfeld et al. (1995), and van Dommelen et al. (2000). These models neglect the contribution from the amorphous phase, crystal interactions, and lamella geometry. Nevertheless, the results of the mechanical response and crystallographic texture for different modes of loading capture reasonably the main trends of the experiments.

Parks and Ahzi (1990) proposed a so-called *constrained hybrid model* for simulating the stress-strain behaviour and texture evolution of polycrystals under nonhomogeneous deformations. To determine the local mechanical response, the model takes account of molecule inextensibility and of low crystal symmetry. Based on a Taylor-type approach (Taylor, 1934), the model handles through a *projection tensor* (mapping tensor) the internal constraints that leave crystals with less than five independent slip systems. The projection tensor formulation allows each crystal to deform as its slip systems permit and neighbouring crystals to accommodate the remainder of deformation. As a consequence, local compatibility is ignored partially. The stress state is obtained by approximating the global stress as an average of the projection of the constraint (local) stresses. Parks and Ahzi's model has been used to predict the mechanical behaviour of polyethylene, olivine, bismuth strontium calcium copper oxide (Ahzi et al., 1993), NiAl polycrystals (Ahzi, 1999), Nylon-6, poly(ethylene terephthalate), and polypropylene (Ahzi et al., 1994); however, it

has been proved that the model predicts a faster texture development than that observed experimentally.

Ahzi et al. (1994) and Lee et al. (1995) re-formulated the model proposed by Parks and Ahzi (1990). These models provide explicit solution of the kinematic constraints associated with the insufficiency of independent slip systems; however, Lee et al.'s formulation can only be applied to crystals in which the number of physically distinct slip systems equals the number of independent ones. Ahzi et al. used the model to simulate plane strain compression and uniaxial compression of 100% crystalline polyethylene and other low symmetry crystals without pyramidal slip, while Lee et al. studied numerically the behaviour of idealized poly(ethylene terephthalate) under plain strain compression. Following Asaro and Needleman's work, Schoenfeld et al. (1995) developed a constitutive model to describe both elasticity and rate dependent crystallographic slip of low symmetry crystalline materials. The total deformation is split into an elastic component which contains lattice stretching and a plastic component which describes crystallographic slippage. By including elasticity, predictive capabilities are expanded to include a broader range of phenomena occurring at small deformations. A modified Taylor-type model ensures equilibrium and compatibility and achieves the interaction law between the macroscopic and local deformations. Van Dommelen et al. (2000) formulated also a viscoplastic constitutive model for kinematically constraint crystals based on the crystallographic slip theory; however in their approach, a finite element solution strategy enforces the kinematic restrictions by an approximate weighting method. Simulations only for an idealized material with three physically distinct slip systems are analyzed.

3.2.2 Semicrystalline models

The microstructure of semicrystalline polyethylene consists of crystalline and amorphous regions locally associated with each other in sandwich-like morphological structures. The constitutive models presented herein are based on two-phase composite inclusions consisting of crystalline lamellae attached to amorphous material, as shown in *Figure* 3.1. Proposed by Ahzi et al. (1990) and Lee et al. (1993a,b), these inclusions have been used successfully to describe from a micromechanical viewpoint the development of deformation-induced texture. A material point is supposed to be the centre of a representative volume element conformed by a collection of randomly oriented inclusions. Crystalline and amorphous phases are treated separately, and each inclusion behaviour is described by using either a Sachs- or a Taylor-type homogenization technique (*e.g.*, Sanchez-

Palencia and Zaoui, 1985). Both crystalline and amorphous phases are assumed to be incompressible (Fellahi et al., 1995; Addiego et al., 2006) and insensitive to pressure deformation (Kitagawa et al., 1992; Fanggao et al., 1996). Crystalline lamellae are considered deforming by crystallographic slip and modelled by the constitutive relations used for small-molecule crystals (Asaro and Needleman, 1985). The amorphous phase is treated as an entangled molecular material lying on lamellar surfaces. Plastic deformations occur by molecular segment rotation (Argon, 1973). Amorphous polyethylene is in rubbery state at room temperature; so, the proposed models use *Rubber Elasticity Theory* (Treloar, 1975) to relate hardening and entropy changes through some measure of deformation, as proposed by Boyce et al. (1988a,b, 1989).

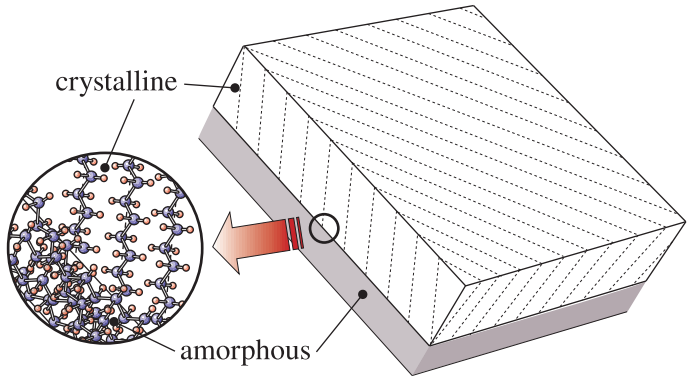

Figure 3.1: Schematic illustration of the two-phase composite inclusion, as proposed by Lee et al. (1993a,b).

Lee et al. (1993a,b) and Argon (1997) pioneered the micromechanical modelling of semicrystalline polymers. In their work, the authors proposed novel models as efficient tools for understanding in a quantitative way the interplay between the microstructure and mechanical behaviour of high density polyethylene at large deformations. These formulations neglect elasticity. The kinematics and morphological details of the deformation processes are investigated in different modes of loading conditions: uniaxial tension and compression, simple shear, and plane strain compression. To obtain the composite inclusion behaviour, different local-global interaction laws are presented. Lee and coworkers proposed a Sachs-type and two self-consistent-like hybrid interaction models to relate the local (inclusion) deformations and stresses to the corresponding macroscopic fields. Argon used a modified Sachs-like model that achieves local-global equilibrium, but satis-

fies compatibility only as a global volume average of the deformations of the individual inclusions. Lee et al. and Argon's model predictions are in satisfactory agreement with experimental observations, proving the relevance of the models to estimate mechanical properties of semicrystalline materials when using reasonable microstructural parameters.

In an attempt to expand modelling capabilities, van Dommelen et al. (2003b) modified Lee and coworkers' model and incorporated elasticity through an anisotropic fourth-order elastic modulus tensor for the crystalline phase and a generalized neo-Hookean relationship (*e.g.*, Salençon, 2001) for the amorphous one. This model has the ability to capture the stress-strain behaviour during monotonic and cyclic loading, anisotropy evolution, and crystallinity effects on the initial modulus, yield stress, and post-yield behaviour. Van Dommelen et al. investigated four interaction models: Taylor, Sachs, and two Taylor-Sachs hybrids, to relate the local and global fields. Only uniaxial compression of initially isotropic high density polyethylene is considered as deformation mode.

A multiscale modelling scheme developed by van Dommelen et al. (2003a) incorporates the influence of the mechanics and geometry of spherulites into the constitutive equations to provide further insight into the deformation mechanisms of semicrystalline polymers. The proposed approach expands the simulation steps into three different scales: *micro*, *meso*, and *macro*, as a way of bridging the morphological and continuum scales. At the microscale, the constitutive properties are developed based on the amorphous and crystalline microstructures, and the stress-strain state is homogenized through a hybrid iteration scheme. Each material point is represented by a spherulite, which is an assembly of preferentially oriented composite lamellae linking the lower and intermediate scales. The spherulite structures are modelled by finite elements to relate the inter- and intra-lamellar deformation mechanisms to the macroscopic (upper level) behaviour of the material.

Recently, Nikolov et al. (2006) developed a model built on the micromechanical framework proposed by Lee et al. (1993a,b). In contrast to Lee and coworkers' approach, Nikolov adopts an inclusion constitutive model in which interlammelar shear is introduced as an additional deformation mechanisms to overcome the kinematic deficiencies of the crystalline structure. The morphological texture is described by the inclusion shape change under an applied deformation gradient. The overall behaviour is obtained through a tangent self-consistent scheme. The stress-strain response and texture evolution for uniaxial tension and compression and simple shear are simulated, and the results

are compared with experimental data and some of the previous numerical models. The model predictions are in satisfactory agreement with most of the aspects observed experimentally.

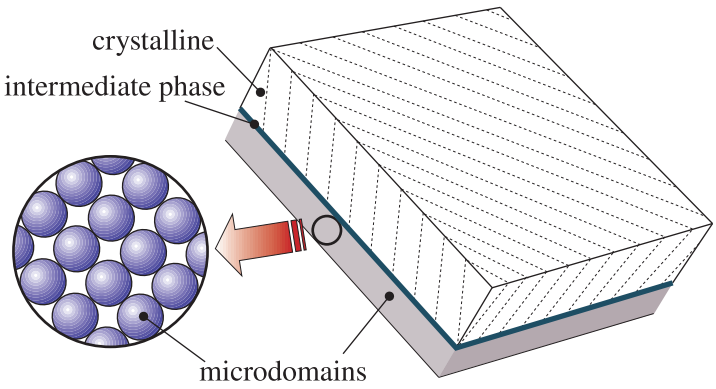

Figure 3.2: Schematic illustration of the two-phase composite inclusion, as proposed by Nikolov and Doghri (2000).

3.3 Small deformation models

Nikolov and Doghri (2000) and Nikolov et al. (2002) proposed constitutive models in which the influences of the microstructure on the initial elastic properties and yield strengths are of particular interest. Nikolov and Doghri proposed a model for simulating small deformations in high density polyethylene. The formulation is valid when crystallinity is high enough; so, the hypothesis of small deformations is satisfied. As in large deformation models, a collection of randomly oriented composite inclusions is used to represent a material point. Each inclusion consists of crystalline lamellae attached to amorphous material. The crystalline phase behaviour is assumed as viscoplastic and described by the constitutive equations proposed by Asaro and Needleman (1985). For the amorphous phase, a viscoplastic model is proposed. Following Wissbrun (1985), each amorphous layer is modelled as a polydomain structure, as shown in *Figure* 3.2. Deformation of the amorphous phase is represented as shrinkage and sliding with respect to each other of the microdomains. To satisfy the hypothesis of incompressibility, the number of microdomains grows when their sizes decrease. Hardening and normal pressure effects are ignored. The rubber-like stretching of tie molecules is incorporated in the

model through an intermediate phase linking the crystalline and amorphous materials. To obtain the stress-strain behaviour, a two-step homogenization scheme is used; first, the homogenization of the phases behaviour within a single inclusion, and then, of all inclusions using a Taylor model. Nikolov et al. (2002) proposed an improved version of their former model to include some minor modifications in the constitutive equations and material parameters to allow unloading. In this model, Nikolov et al. use a similar homogenization approach for the inclusions, but predict the overall behaviour by the simple Sachs assumption of uniform stress in the collection of composite inclusions.

CHAPTER
FOUR

Damage-coupled model for crystalline polyethylene [1]

4.1 Introduction

Polyethylene is never completely crystalline. Nevertheless, as a first modelling approach, the analysis presented herein is exclusively confined to the crystalline phase, and no attempt is made to include the amorphous phase contribution. The interplay between the two phases will be the subject of *Chapter* 6. Thus, polyethylene microstructure is thought of as an aggregate (collection) of discrete and randomly oriented crystals, as schematically shown in *Figure* 4.1. Each crystal is considered as a three-dimensional assembly of molecules arranged into an orthorhombic lattice structure (Bunn, 1954). In a lattice, molecules are kept together by van der Waals forces, and the leading deformation mechanism is crystallographic slip along specific crystallographic planes (Bowden and Young, 1974). Accordingly, in the model, Continuum Damage Mechanics provides a framework for describing crystal fragmentation caused by the debonding of the crystallographic planes (Séguéla, 2001). Hence, damage as well as hardening are given in terms of the slip systems and related to the macroscopic behaviour throughout material parameters. The evolution of the microstructure properties is also an aspect considered in the model. To characterize the overall behaviour, homogenization of stresses and deformations is defined as volume averaging over the crystals.

4.2 Finite deformations

Before presenting the model formulation, the following section briefly reviews the finite deformation theory applicable to the micromechanics of crystal plasticity. In gen-

[1] This chapter is based on Alvarado-Contreras et al. (2005, 2006b, 2007a)

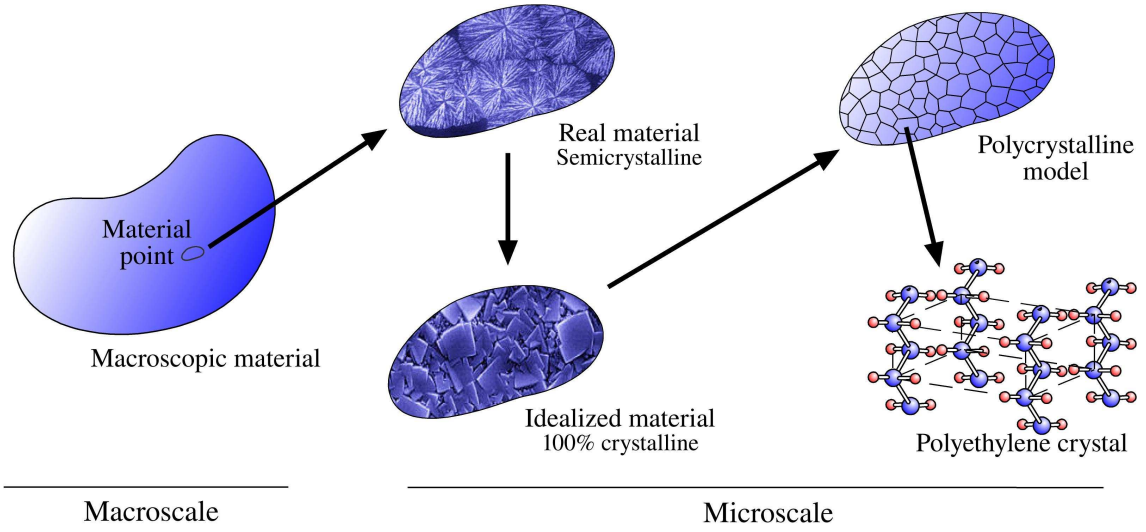

Figure 4.1: Schematic representation of the material idealization.

eral, upon loading, a body changes its shape as well as its position and orientation. In *Figure* 4.2, $\mathcal{B}^o \subset \mathbb{R}^3$ and $\mathcal{B} \subset \mathbb{R}^3$ denote respectively the reference and current (deformed) configurations for a continuous body. In the reference configuration, a representative material point P^o occupies a spatial point with a position vector X_i. In the deformed configuration at some time t, the particle originally at P^o sets at point P with a position vector x. Mathematically, assuming that deformation is smooth, the deformation function $x_i = x_i(X_j\hat{e}_j, t)$ describes the motion by mapping points $X_i \in \mathcal{B}^o$ onto points $x_i \in \mathcal{B}$. To define how material points move in relation to neighboring points, the deformation gradient tensor can be defined as

$$F_{ij} = \frac{\partial x_i}{\partial X_j} \tag{4.1}$$

where it is assumed that $det(F_{ij}\hat{e}_i\hat{e}_j) > 0$.

Supposing that the deformation gradient is a continuous one-to-one function with continuous partial derivatives to whatever order is required, the necessary and sufficient condition for the inverse to exist is that its Jacobian does not vanish. In an appropriate kinematic framework for large deformations, the deformation gradient is decomposed into elastic and plastic components (Lee, 1969)

$$F_{ij} = \frac{\partial x_i}{\partial x_k^p}\frac{\partial x_k^p}{\partial X_j} = F_{ik}^* F_{kj}^p \tag{4.2}$$

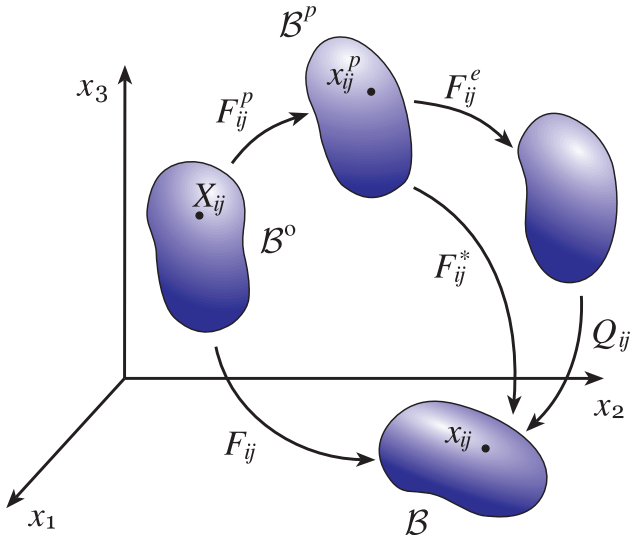

Figure 4.2: Kinematics of finite deformation (Lee, 1969; Zbib and Aifantis, 1988).

As shown in *Figure* 4.2, F_{ij}^p introduces the so-called intermediate configuration $\mathcal{B}^p$. Thus, upon unloading the body from the current configuration $\mathcal{B}$, the elastic deformation can be completely recovered while no additional plastic deformation takes place. Therefore, $x_i^p = x_i^p(X_j\hat{e}_j, t)$ is a continuous one-to-one function mapping material points $x_i \in \mathcal{B}$ onto points $x_i^p \in \mathcal{B}^p$. In *Equation* 4.2, the elastic deformation gradient F_{ij}^* can be further decomposed into strain and rotation such that

$$F_{ij}^* = Q_{ik}\, F_{kj}^e \tag{4.3}$$

where F_{ij}^e causes purely elastic deformations and Q_{ij} is an orthogonal tensor corresponding to the orientation of certain material characteristics (Zbib and Aifantis, 1988).

After calculating the material time derivative of the deformation gradient $\partial \dot{x}_i / \partial X_j$, the velocity gradient L_{ij} can be written as

$$L_{ij} = \frac{\partial \dot{x}_i}{\partial X_k}\frac{\partial X_k}{\partial x_j} = \dot{F}_{ik}\, {F_{kj}}^{-1} \tag{4.4}$$

In view of the fact that Q_{ij} may exist even in the absence of elastic deformations; *i.e.*, $F_{ij}^e \sim I_{ij}$, the total deformation rate is given by the symmetric part of L_{ij}

$$D_{ij} = \mathrm{sym}(L_{ij}) \tag{4.5a}$$

therefore,

$$D_{ij} = Q_{ik}\ \mathrm{sym}(\dot{F}^e_{kl}{F^e_{lm}}^{-1})\ Q_{jm} + Q_{ik}\ \mathrm{sym}(F^e_{kl}\dot{F}^p_{lm}{F^p_{mn}}^{-1}\,{F^e_{nq}}^{-1})\ Q_{jq} \tag{4.5b}$$

where $D^e_{ij} = Q_{ik}\ \mathrm{sym}(\dot{F}^e_{kl}{F^e_{lm}}^{-1})\ Q_{jm}$ and $D^p_{ij} = Q_{ik}\ \mathrm{sym}(F^e_{kl}\dot{F}^p_{lm}{F^p_{mn}}^{-1}\,{F^e_{nq}}^{-1})\ Q_{jq}$ denote the elastic and plastic deformation rates, respectively (Zbib and Aifantis, 1988). Therefore,

$$D_{ij} = D^e_{ij} + D^p_{ij} \tag{4.6}$$

Conversely, the total spin is defined as the skew-symmetric part of L_{ij}

$$W_{ij} = \mathrm{skw}(L_{ij}) \tag{4.7a}$$

therefore,

$$W_{ij} = \dot{Q}_{ik}Q_{jk} + Q_{ik}\ \mathrm{skw}(\dot{F}^e_{kl}{F^e_{lm}}^{-1})\ Q_{jm} + Q_{ik}\ \mathrm{skw}(F^e_{kl}\dot{F}^p_{lm}{F^p_{mn}}^{-1}{F^e_{nq}}^{-1})\ Q_{jq} \tag{4.7b}$$

where $W^m_{ij} = \dot{Q}_{ik}Q_{jk}$ is the rigid-body spin tensor, and $W^e_{ij} = Q_{ik}\ \mathrm{skw}(\dot{F}^e_{kl}{F^e_{lm}}^{-1})\ Q_{jm}$ and $W^p_{ij} = Q_{ik}\ \mathrm{skw}(F^e_{kl}\dot{F}^p_{lm}{F^p_{mn}}^{-1}{F^e_{nq}}^{-1})\ Q_{jq}$ are the elastic and plastic spins, respectively. Consequently,

$$W_{ij} = W^m_{ij} + W^e_{ij} + W^p_{ij} \tag{4.8}$$

4.3 Proposed damage model

Continuum Damage Mechanics, originated by Kachanov (1958), describes the influence of microstructural changes in the mechanical response of solids. These changes consist mainly of the nucleation and growth of small defects distributed throughout a solid prior to its final failure (Krajcinovic, 1996). To explain decreases in stiffness and strength, damage mechanics uses the so-called damage variables. These variables represent an averaged, statistical, or homogenized measurement of thousands of atomic imperfections caused by billions of atomic debonds (Krajcinovic, 1995; Bolotin, 1999). Several damage definitions are possible for consideration (*e.g.*, Zyczkowski, 2000; Zheng and Betten, 1996). Depending on the nature of the problem, damage variables are characterized in terms of stresses, strains, and/or some other associated internal state variables (Lemaitre, 1984), and are written as scalars, or second-, or fourth-order tensorial functions.

In this paper, the deformation mechanisms in polyethylene crystals are described by the theory of crystallographic slip (Bassani, 1994). The crystal structure found in polyethylene materials has a unit cell of orthorhombic geometry characterized by crystallographic slip systems along planes parallel to the chain axis. Each crystal possesses only four possible slip planes, each one with a chain and a transverse slip direction, as shown in *Figure* 4.3. Thus, eight slip systems are available to accommodate any given deformation. The three indices enclosed in parentheses (*hkl*) and the three indices enclosed in square brackets [*uvw*] represent the slip direction and the plane Miller indices, respectively.

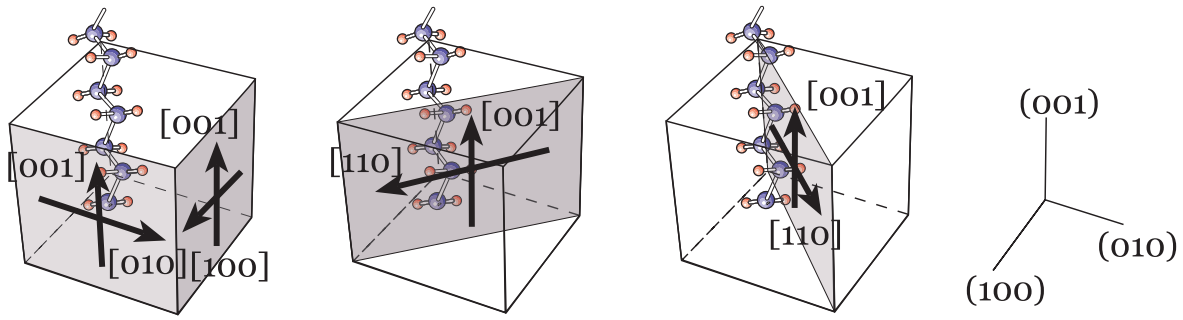

Figure 4.3: Slip systems in a polyethylene crystal.

4.3.1 Formulation

The aspects and mechanisms of damage processes in polyethylene materials are quite complex and are still only partially understood. Throughout the present work, the damage variable attempts to describe the mechanisms that render the displacement field causing discontinuous shear flow. These discontinuities are attributed to the intracrystalline debonding and subsequent crystal fragmentation (Bowden and Young, 1974; Hiss et al., 1999; Peterlin, 1971; Lustiger and Markham, 1983; G'Sell and Dahoun, 1994; Kazmierczak et al., 2005). Based on the slip theory, a damage variable is introduced and coupled with the constitutive model. Within this study framework, this variable describes the loss of load-carrying capacity attributed to the failure of van der Waals bonds along the slip systems during loading. Covalent bonds are assumed stable; therefore, molecule fracture is not included in the model. To describe the damage process in a crystallographic plane, a schematic representation of the concepts involved is given in *Figure* 4.4. Consider a crystal deforming by shear, as sketched in *Figure* 4.4a. Once the critical resolved

shear stress in the slip direction is exceeded, slip becomes translation along the plane (*Figure* 4.4b). Since an irreversible rearrangement of the microstructure occurs and the number of van der Waals bonds decreases (*Figure* 4.4c), the associated degradation process is described mathematically by a scalar variable Ω^α related to the fraction of atomic debonds; therefore,

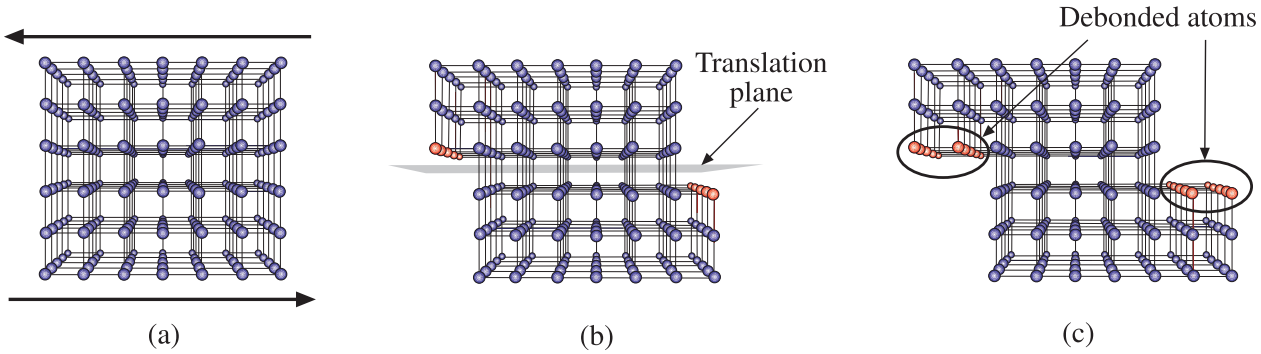

Figure 4.4: Idealized damage mechanisms for crystal slip systems.

$$\Omega^\alpha \equiv \frac{\text{Current number of atomic debonds}}{\text{Initial number of atomic bonds}} \tag{4.9}$$

where $\alpha = \{1, 2, \ldots, 8\}$ is the slip system index. Let ΔA^α be a small surface area on the α-slip system. Assuming that the number of atomic bonds is proportional to the corresponding atomic plane area, a mechanical damage measurement may be expressed as

$$\Omega^\alpha \equiv \frac{\text{Total area of defects}}{\text{Initial area}} = \frac{\Delta A^\alpha_\Omega}{\Delta A^\alpha} \tag{4.10}$$

Let $\Delta \tilde{A}^\alpha = \Delta A^\alpha - \Delta A^\alpha_\Omega$ be the effective area of resistance once slippage has occurred. The damage variable can be likewise written as

$$\Omega^\alpha = 1 - \frac{\Delta \tilde{A}^\alpha}{\Delta A^\alpha} \tag{4.11}$$

From *Equation* 4.11, it can be seen that damage takes theoretical values of $0 \leq \Omega^\alpha \leq 1$, where the limits represent an original and a fractured slip system, respectively.

The application of the damage variable to crystal slip systems is straightforward. For a given slip system, the effective shear stress $\tilde{\tau}^\alpha$ can be approximated as the ratio between the shear force ΔV^α on the plane and the effective shear area $\Delta \tilde{A}^\alpha$; therefore,

$$\tilde{\tau}^\alpha \equiv \lim_{\Delta \tilde{A}^\alpha \to 0} \frac{\Delta V^\alpha}{\Delta \tilde{A}^\alpha} = \frac{dV^\alpha}{d\tilde{A}^\alpha} \tag{4.12}$$

The effect of slip system degradation is established by introducing the damage variables into the constitutive equation with the concept of effective state variables. As pointed out by Lemaitre and Dufailly (1987),

> *The principle of strain equivalence states that any strain constitutive equation of a damaged material is written exactly as for a virgin material except that the stress is replaced by the effective stress.*

Therefore, by assuming the existence of a fictitious undamaged material, the effective shear stress can be written as a function of the nominal shear stress τ^α

$$\tilde{\tau}^\alpha \equiv \frac{\Delta V^\alpha}{(1-\Omega^\alpha)\Delta A^\alpha} = \frac{\tau^\alpha}{1-\Omega^\alpha} \tag{4.13}$$

where ΔA^α is the initial shear area of the slip system.

In crystal plasticity, it is assumed that shear strain rates are independent of the resolved shear stresses acting on other systems (Hutchinson, 1976). Thus, as used in numerous crystal mechanics models, the constitutive equation connecting the slip rate and resolved shear stress on a slip system is chosen to be a power-law relationship, as follows

$$\dot{\gamma}^\alpha = \dot{\gamma}_0 \left(\frac{\tilde{\tau}^\alpha}{g^\alpha} \right)^n \tag{4.14}$$

where $\dot{\gamma}_0$ and g^α are the reference shear strain rate and current reference shear strength, respectively, and n is a positive parameter representing the inverse of the microscopic rate sensitivity.

Figure 4.5 illustrates the stress-strain relationship given by *Equation* 4.14 for assorted values of n. This graph suggests that inelastic deformations are always present on the slip systems as long as shear stresses are not identically equal to zero, but if $\tau^\alpha < g^\alpha$, the relationship gives a negligibly small value of shear rate (Ahzi et al., 1994).

Accordingly, substituting *Equation* 4.13 into 4.14, the effective stress-strain relationship is written as a function of the nominal shear stress

$$\dot{\gamma}^\alpha = \dot{\gamma}_0 \left[\frac{\tau^\alpha}{(1-\Omega^\alpha) g^\alpha} \right]^n \tag{4.15}$$

Supposing that the stress state applied to the aggregate of crystals is given by the Cauchy stress tensor σ_{ij}, the shear stress on the crystallographic planes can be determined by resolving σ_{ij} onto the slip systems using Continuum Mechanics

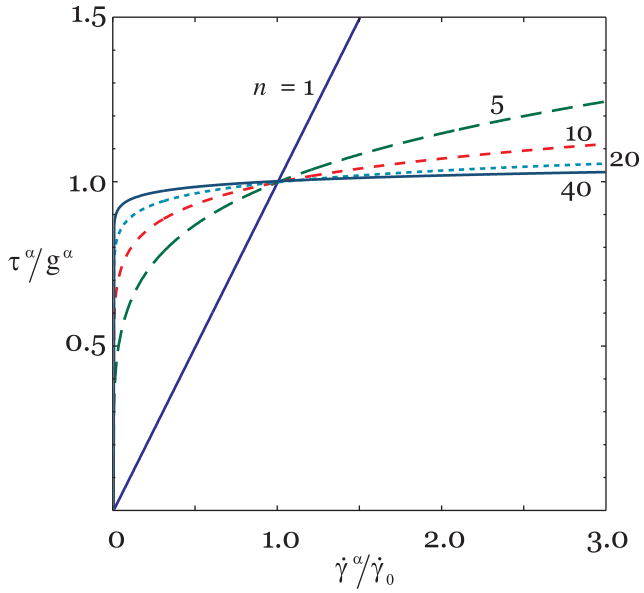

Figure 4.5: Schematic representation of the power law stress-strain rate relation for five different values of n (Ahzi et al., 1994).

$$\tau^{\alpha} = s_i^{\alpha} \sigma_{ij} n_j^{\alpha} = \sigma_{ij} T_{ji}^{\alpha} \tag{4.16}$$

where n_i^{α} and s_i^{α} are a pair of orthogonal unit vectors defining the slip plane normal and the slip direction, respectively. The product $T_{ij}^{\alpha} = n_i^{\alpha} s_j^{\alpha}$ is the so-called Schmid tensor, which can be interpreted as a slip system orientation tensor. Then, decomposing the Schmid tensor into symmetric and skew-symmetric components

$$R_{ij}^{\alpha} = \text{sym}(T_{ij}^{\alpha}) = \tfrac{1}{2}(s_i^{\alpha} n_j^{\alpha} + n_i^{\alpha} s_j^{\alpha}) \tag{4.17a}$$

and

$$A_{ij}^{\alpha} = \text{skw}(T_{ij}^{\alpha}) = \tfrac{1}{2}(s_i^{\alpha} n_j^{\alpha} - n_i^{\alpha} s_j^{\alpha}) \tag{4.17b}$$

and decomposing the Cauchy stress tensor into deviatoric and spherical components

$$\sigma_{ij} = S_{ij} + \sigma_{kk} I_{ij} \tag{4.18}$$

the resolved shear stress is reduced to the expression

$$\tau^{\alpha} = S_{ij} R_{ji}^{\alpha} \tag{4.19}$$

Equation 4.19 implies that the spherical stresses have no influence on the resolved shear stresses.

Molecule inextensibility plays an important role in determining the behaviour of crystalline polyethylene samples. In polymer crystals, plastic deformation D_{ij}^{p} vanishes along molecule direction c_i. This means that $c_i D_{ij}^{p} c_j = D_{ij}^{p} C_{ji} = 0$, where $C_{ij} = c_i c_j$ (Schoenfeld et al., 1995). When crystals experience large plastic deformations, the contribution of the elastic component of the velocity gradient to the total one can be ignored. Hence, the total deformation rate D_{ij} in *Equation* 4.6 is interpreted solely as the plastic deformation rate; *i.e.*, $D_{ij} \cong D_{ij}^{p}$, and the total spin W_{ij} in *Equation* 4.8 as the sum of the rigid-body spin and plastic spin tensor; *i.e.*, $W_{ij} \cong W_{ij}^{m} + W_{ij}^{p}$. As pointed out by Asaro (1983), the plastic component of the velocity gradient L_{ij} is given by the contributions of the shear strain rates $\dot{\gamma}^{\alpha}$ on all slip systems. Therefore, by using the additive decomposition of the Schmid tensor, slip-based kinematic equations for the plastic deformation and spin are given as

$$D_{ij}^{p} = \sum\nolimits_{\alpha} \dot{\gamma}^{\alpha} R_{ij}^{\alpha} \tag{4.20a}$$

and

$$W_{ij}^{p} = \sum\nolimits_{\alpha} \dot{\gamma}^{\alpha} A_{ij}^{\alpha} \tag{4.20b}$$

where the summation is over all slip systems.

For constrained crystals, Parks and Ahzi (1990) assumed that deviatoric stresses S_{ij} have the unique additive decomposition given as

$$S_{ij} = S_{ij}^{c} + S_{ij}^{*} \tag{4.21}$$

in which S_{ij}^{c} is a stress component aligned with the inextensible direction; therefore, $S_{ij}^{c} \propto C_{ij}$, and S_{ij}^{*} is an orthogonal sub-transformation, where $S_{ij}^{c} S_{ij}^{*} = 0$. Using the above decomposition and given that $R_{ij}^{\alpha} C_{ij} = 0$, the resolved shear stress reduces to

$$\tau^{\alpha} = S_{ij}^{*} R_{ji}^{\alpha} \tag{4.22}$$

From *Equations* 4.13 and 4.22 and ignoring elastic deformations, a pseudo-linear relationship between the microscopic deviatoric stress and deformation rate can be further expressed as

$$D_{ij} = M_{ijkl} S_{lk}^{*} \tag{4.23}$$

where M_{ijkl} is the fourth-order compliance tensor given by

$$M_{ijkl} = \dot{\gamma}_0 \sum_\alpha \frac{1}{(1-\Omega^\alpha)g^\alpha} \left| \frac{S^*_{mn} R^\alpha_{nm}}{(1-\Omega^\alpha)g^\alpha} \right|^{n-1} R^\alpha_{ij} R^\alpha_{kl} \tag{4.24}$$

4.3.2 Damage evolution law

The state equation (*Equation* 4.23) makes the model more realistic but also more difficult to handle numerically, as it requires the choice of a damage evolution law. In general, a damage evolution law is a non-negative function of the stress, strain, and/or other appropriate internal state variables, *i.e.*,

$$\dot{\Omega} = \dot{\Omega}(\sigma_{ij},\ \varepsilon_{ij},\ \text{internal state variables}) \tag{4.25}$$

where $\dot{\Omega} = d\Omega/d\lambda$, and $\lambda > 0$ is a monotonically increasing time-type parameter (Kachanov, 1986).

Damage should be associated with phenomena causing it; however, some simplifications are required for computational convenience. In the proposed model, it is postulated that damage occurs when resolved forces acting on crystal planes are high enough to overcome the intermolecular (secondary) bonds (bond strengths), which hold molecules together into a coherent structure. No rupture of the covalent (primary) bonds between hydrogen and carbon atoms is considered. As a result, in a crystal, damage is a quantity that varies from one slip system to another and depends only on the local stress states. Strain and temperature influence is ignored, and monotonous loading is assumed. Subsequently, *Equation* 4.25 is a function such that $\dot{\Omega} = \dot{\Omega}(\sigma_{ij}, \Omega)$. Using a power-law relationship, the following damage evolution law is introduced into the model,

$$\frac{d\Omega^\alpha}{d\tau^\alpha} = \begin{cases} \dot{\Omega}_0 \left| \dfrac{\tau^\alpha}{(1-\Omega^\alpha)g^\alpha} \right|^m & \text{if } d\tau^\alpha > 0 \text{ (damage loading)} \\ 0 & \text{otherwise (damage neutral loading)} \end{cases} \tag{4.26}$$

where $\dot{\Omega}_0$ and m denote the reference damage rate and damage rate sensitivity, respectively.

4.3.3 Slip system hardening

When slip systems deform plastically, the density of structural imperfections increases impeding molecules to move and, consequently, leading to an increase of the stress re-

quired to sustain shear slip. As described by Lemaitre and Chaboche (1994), damage and hardening processes can be considered independent of each other. Since the model regards the material as idealized 100% crystalline, it is assumed that the reference shear strength g^{α} increases with strain. In this work, hardening rate of slip systems is assumed to evolve with deformation according to the following relation

$$\dot{g}^{\alpha} = \sum_{\beta} h_{\alpha\beta} \dot{\gamma}^{\beta} \tag{4.27}$$

where $h_{\alpha\beta}$ is a hardening matrix. This matrix describes the hardening interaction of the slip systems. Thus, the diagonal terms represent self-hardening, and the off-diagonal terms represent latent hardening (Hutchinson, 1976; Asaro, 1983). Due to the lack of experimental information, it is assumed that the critical resolved shear stresses increase proportionally to the total shear strain. Therefore, $h_{\alpha\beta} = h$, and the evolution of hardening in *Equation* 4.27 is rewritten as (Hutchinson, 1976)

$$\dot{g}^{\alpha} = h \sum_{\beta} \dot{\gamma}^{\beta} \tag{4.28}$$

The hardening modulus h used in this model has the following form

$$h = h_0 \operatorname{sech}^2(h_0 \hat{\gamma}/c) \tag{4.29}$$

where h_0 and c are slip system parameters representing the hardening rate and saturation shear strength, respectively, and $\hat{\gamma}$ is the equivalent plastic strain, related to the second invariant $\bar{D}_{ij}\bar{D}_{ij}$ of the deformation rate as

$$\hat{\gamma} = \int_0^t \sqrt{2\bar{D}_{ij}\bar{D}_{ij}}\, dt \tag{4.30}$$

4.4 Crystal average

In crystal plasticity, the overall mechanical response is usually obtained by averaging the respective microscopic values of deformation, stress, and any other internal variable over the number of crystals in an aggregate. Constitutive evolution equations are related to macroscopic quantities through assumptions regarding both equilibrium and compatibility. The average scheme assumes that crystals can accommodate any deformation state. However, for materials deforming by crystallographic slip, the minimum number of distinct slip systems to permit an arbitrary deformation is five. Orthorhombic polyethylene crystals have fewer slip systems available than required and also show differences in slip

Table 4.1: Designation of slip systems in polyethylene crystals.

Slip system α	**Slip plane** $\{hkl\}$	**Slip direction** $\langle uvw \rangle$
1	(100)	[010]
2		[001]
3	(100)	[100]
4		[001]
5	(110)	$[1\bar{1}0]$
6		[001]
7	$(1\bar{1}0)$	[110]
8		[001]

system shear strengths. Due to these features, Parks and Ahzi (1990) and Schoenfeld et al. (1995) proposed a modified Taylor model to define interaction laws taking into account crystal constraints.

4.4.1 Macroscopic deformation rate

As shown in *Table* 4.1, eight slip systems along the ($hk0$)-type planes are available to accommodate any given deformation. However, a constant volume process is only possible when five independent slip systems are active. In polyethylene crystals, although eight distinct slip systems are available to accommodate deformation, yet only four of those systems are independent (*e.g.*, Wecker, 1975; Cotton and Kaufman, 1991). Therefore, extra kinematic constraints, beyond incompressibility, must be imposed to predict deformation evolution. These constraints are easy to define once the directions along which plastic deformation vanishes are identified (Lee et al., 1995; Schoenfeld et al., 1995).

In constrained crystals, it is natural to assume that the macroscopic deformation rate is partitioned unequally among crystals. Let $\bar{D}_{ij}$ and D_{ij} be respectively the macroscopic and crystal deformation rates, where $D_{ij}C_{ji} = 0$. Thus, the proportionality relation between $\bar{D}_{ij}$ and D_{ij} can be written as follows

$$D_{ij} = K^D_{ijkl}\bar{D}_{lk} \tag{4.31}$$

where K^D_{ijkl} is a fourth-order proportionality tensor depending on crystal orientations.

Parks and Ahzi (1990) postulated the existence of an intermediate deformation rate $\tilde{D}_{ij}$ given by the following additive decomposition

$$\tilde{D}_{ij} = D_{ij} + D^c_{ij} \tag{4.32}$$

in which D^c_{ij} represents the deformation rate along the inextensible direction accommodated among other crystals in the aggregate, where $D_{ij}D^c_{ji} = 0$. By using an enforcing multiplier β, D^c_{ij} can be approximated as

$$D^c_{ij} = \beta C_{ij} \tag{4.33}$$

Crystal and intermediate deformation rates relate through the inextensibility constraint, such as in the model proposed by Parks and Ahzi (1990),

$$D_{ij} = P_{ijkl}\tilde{D}_{lk} \tag{4.34}$$

For each crystal, P_{ijkl} is a function of the chain direction vector c_i, expressed as

$$P_{ijkl} = I_{ijkl} - \tfrac{1}{3}C'_{ij}C'_{kl} \tag{4.35}$$

Here, I_{ijkl} is the fourth-order identity tensor given as

$$I_{ijkl} = \tfrac{1}{2}(\delta_{ik}\delta_{jl} + \delta_{il}\delta_{jk}), \tag{4.36}$$

and C'_{ij} is the deviatoric part of C_{ij} defined as

$$C'_{ij} = c_i c_j - \tfrac{1}{3}c_k c_k \delta_{ij} \tag{4.37}$$

To satisfy global compatibility, the macroscopic deformation rate must equal the average deformation rate over the aggregate; thus,

$$\bar{D}_{ij} = \langle D_{ij} \rangle \tag{4.38}$$

As a result, if D_{ij} is given as in *Equation* 4.34,

$$\bar{D}_{ij} = \langle P_{ijkl} \rangle \tilde{D}_{lk} \tag{4.39}$$

and, once again, on the crystal level

$$D_{ij} = P_{ijkl}\langle P_{lknm} \rangle^{-1} \bar{D}_{mn} \tag{4.40}$$

This shows that the proportionality tensor K^D_{ijkl} is

$$K^D_{ijkl} = P_{ijmn}\langle P_{nmkl}\rangle^{-1} \tag{4.41}$$

and that the macroscopic deformation rate $\bar{D}_{ij}$ partitions unequally among the crystals, partially fulfilling global compatibility.

4.4.2 Macroscopic spin

The plastic spin influences the overall behaviour of crystal aggregates as it governs the development of crystallographic textures. In the proposed model, it is also assumed that damage plays a role in controlling the rate of change of crystallographic axes. Let $\bar{W}_{ij}$ and W_{ij} be the macroscopic and crystal spin, respectively. Since crystal spin requires only three independent components, a full Taylor mean field hypothesis is adopted to relate $\bar{W}_{ij}$ and W_{ij}. Consequently, the macroscopic spin simply equals the average one, as follows (Parks and Ahzi, 1990; Schoenfeld et al., 1995)

$$\bar{W}_{ij} = \langle W_{ij}\rangle \tag{4.42}$$

It is postulated that plastic spin W^p_{ij} depends linearly on an empirical fourth-order release tensorial function, which governs crystal rotation via the current crystal damage state, $R = R(\Omega^\alpha)$. Therefore, after ignoring elastic spin, the total spin in *Equation* 4.8 can be modified as

$$W_{ij} = W^m_{ij} + R_{ijkl}W^p_{lk} \tag{4.43}$$

with W^p_{ij} defined as in *Equation* 4.20b. In the current version of the model, a simplified scalar release function is proposed governing crystal rotation based exclusively on the crystal damage state, as follows

$$R = \tanh(\zeta\bar{\Omega}) \tag{4.44}$$

where $\bar{\Omega} = \frac{1}{8}\sum_\alpha \Omega^\alpha$ is the crystal average damage, and ζ is a non-dimensional material parameter adjusted to match experimentally measured texture development. Figure 4.6 illustrates the $\bar{\Omega} - R$ relationship given by *Equation* 4.44 for different values of ζ. This graph suggests that $\zeta \to \infty$ for damage has only a slight influence on spin.

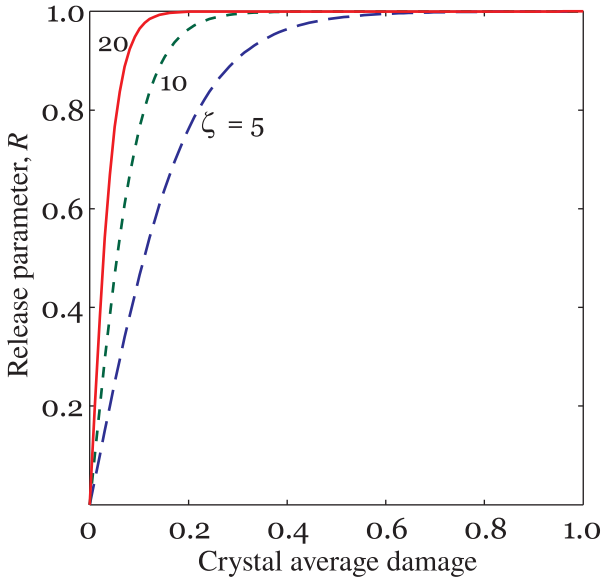

Figure 4.6: Schematic representation of the release parameter for three different values of ζ.

4.4.3 Macroscopic stress

Assuring global equilibrium, it is assumed that each crystal undergoes the same stress state as the aggregate. Thus, by analogy with *Equation* 4.31, it is postulated the existence of a proportionality relationship between the global and local stresses; therefore

$$\bar{S}_{ij} = K^S_{ijkl} \langle S^*_{lk} \rangle \tag{4.45}$$

where K^S_{ijkl} is a fourth-order transformation tensor, $\langle S^*_{ij} \rangle$ is the average reduced stress, and $\bar{S}_{ij}$ is the deviatoric macroscopic stress. From global equilibrium, the stress $\bar{S}_{ij}$ is determined by averaging the crystal deviatoric Cauchy stress responses in the aggregate; therefore,

$$\bar{S}_{ij} = \langle S_{ij} \rangle \tag{4.46}$$

If the deviatoric stress for each crystal S_{ij} is expressed as the additive decomposition given in *Equation* 4.21, and the stress component S^c_{ij} associated with the kinematic constraint is approximated as the projection of S_{ij} onto the c-direction, $S^c_{ij} = \frac{3}{2} C'_{ik} C'_{jl} S_{lk}$ (Parks and Ahzi, 1990), the reduced stress can be written as

$$S^*_{ij} = P_{ijkl} S_{lk} \tag{4.47}$$

where P_{ijkl} is the projection tensor, as defined in *Equation* 4.35. Substituting *Equation* 4.47 into 4.46, the relationship between the average reduced stress and the macroscopic stress can be expressed as

$$\bar{S}_{ij} = \langle P_{ijkl} \rangle^{-1} \langle S^*_{lk} \rangle \tag{4.48}$$

As a result, the proportionality tensor in *Equation* 4.45 can be approximated to the inverse average projection tensor, as follows

$$K^S_{ijkl} = \langle P_{ijkl} \rangle^{-1} \tag{4.49}$$

4.4.4 Macroscopic constitutive equation

Crystal aggregate response can be expressed in terms of an overall compliance tensor relating the macroscopic deformation rate and deviatoric stress (Hutchinson, 1970),

$$\bar{D}_{ij} = \bar{M}_{ijkl} \bar{S}_{lk} \tag{4.50}$$

where $\bar{M}_{ijkl}$ is obtained by averaging the respective crystal compliance tensors (*Equation* 4.24)

$$\bar{M}_{ijkl} = \langle M_{ijkl} \rangle \tag{4.51}$$

When $\bar{D}_{ij}$ is imposed, crystal stress must satisfy the following local constitutive equation

$$\bar{D}_{ij} = \langle P_{ijkl} \rangle^{-1} P_{lknm} M_{mnpq} S^*_{qp} \tag{4.52}$$

Then, if the average stress assures global boundary conditions, the solution satisfies the global constitutive equation,

$$\bar{D}_{ij} = \langle M_{ijkl} \rangle \langle P_{klmn} \rangle^{-1} \langle S^*_{mn} \rangle \tag{4.53}$$

4.5 Numerical results and discussion

This section examines the capability of the model to represent the mechanical behaviour of polyethylene based only on its crystalline microstructure. The theoretical responses are obtained by numerical integration of the constitutive equations introduced above.

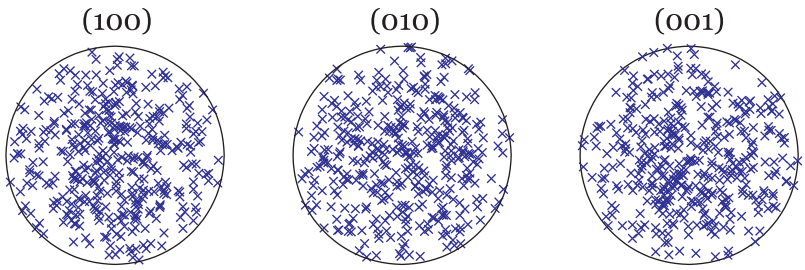

Figure 4.7: Initial pole figures of the (100), (010), and (001) lattice directions.

Two simulations are carried out to validate the proposed model capturing the stress-strain behaviour and texture evolution under uniaxial tension and simple shear loading conditions. The results are compared with experimental data and numerical simulations from other references (Parks and Ahzi, 1990; Hillmansen et al., 2000; Yang and Chen, 2001). A comparison between Parks and Ahzi's (1990) and the proposed damage-coupled models is shown in *Appendix* A. It is assumed that the number of crystals in the aggregate is fixed as the material deforms. Calculations are carried out for an aggregate of 100 randomly oriented orthorhombic crystals. According to that, the distributions of the (100), (010), and (001) poles are uniform, and the material can be considered as isotropic. In the simulations, texture is fully determined by the poles of two non-parallel planes, and crystal orientations are graphically described by the stereographic projections of the poles onto a plane tangent to the projection sphere (*e.g.*, see Chapter 2 of Kelly et al., 2000). Figure 4.7 shows the initial pole figures in terms of the (100) and (001) poles. Likewise, the velocity gradient $\bar{L}_{ij} = \bar{D}_{ij} + \bar{W}_{ij}$ is prescribed, and crystal stresses and orientation changes are determined. Then, the macroscopic stress state is calculated.

4.5.1 Uniaxial tension case

The aggregate behaviour is examined by deforming it under uniaxial tension. A constant velocity gradient with axisymmetric boundary conditions is given as

$$\bar{L}_{ij} = \dot{\gamma} \begin{bmatrix} -0.5 & 0.0 & 0.0 \\ 0.0 & 1.0 & 0.0 \\ 0.0 & 0.0 & -0.5 \end{bmatrix}$$

where $\dot{\gamma}$ is a constant macroscopic strain rate equal to 0.001 s^{-1}. The macroscopic spin is null. For all crystals, the eight slip systems are active and their initial shear strengths are adopted from the work of Parks and Ahzi (1990), as reproduced in *Table* 4.2. The model

Table 4.2: Resolved shear strengths.

Slip system	$\mathbf{g^{\alpha}}$**[MPa]**
(100)[001]	7.2
(010)[001]	7.2
$\{110\}\langle 001\rangle$	7.2
(100)[010]	7.92
(010)[100]	12.96
$\{110\}\langle 1\bar{1}0\rangle$	12.96

Table 4.3: Material parameters for the simulations.

Parameter	**Uniaxial tension**	**Simple shear**
Strain rate sensitivity, n	5.0	5.0
Reference strain rate, $\dot{\gamma}_0$ [s^{-1}]	0.001	0.001
Damage rate sensitivity, m	2.0	2.0
Reference damage rate, $\dot{\Omega}_0$ [MPa^{-1}]	0.05	0.05
Hardening modulus, h_0 [MPa/s]	6.0	3.0
Saturation shear strength, c [MPa]	23.0	7.8
Spin release, ζ	30.0	17.5

parameters are set up from a tensile test reported in Hillmansen et al. (2000) and shown in *Table* 4.3.

Figure 4.8 shows the predicted stress-strain curve for the given loading condition. The aggregate behaviour under uniaxial tension is compared with the experimental response from Hillmansen et al. (2000) as well as with the results of the viscoplastic model in Parks and Ahzi (1990). As shown in *Figure* 4.8, the proposed model has the capability to handle larger strains than the previous model in Parks and Ahzi (1990). Also, the stress-strain curve is in good agreement with the experimental behaviour. In this curve, three stages can be identified. First, the stress value is seen to increase moderately with straining. Then, the stress rises sharply with limited deformation due to molecule reorientation towards the pulling direction. Finally, the idealized material becomes stiffer than

the real one. This last aspect suggests the importance of the amorphous phase, a feature ignored in the current formulation, in providing additional intracrystalline deformation in real polyethylene. In addition, as seen in *Figure* 4.8, the stress-strain curve does not capture the stress increase at the early states of deformation since the formulation does not include the elastic contribution of the velocity gradient ($D^e_{ij} = 0$ and $W^e_{ij} = 0$ in *Equations* 4.6 and 4.8, respectively). *Figure* 4.9 gives the predicted average damage on the eight slip systems. The solid and broken lines represent the solutions for the chain and transverse slip systems, respectively. The figure shows that damage gradually evolves with straining and exhibits a nonlinear behaviour while developing anisotropy in the material. It is easy to see from the damage evolution plot that damage values on the $(1\bar{1}0)[110]$ and $(110)[1\bar{1}0]$ systems are initially larger than those exhibited on the other systems; however, as straining progresses, damage on the $(100)[00\bar{1}]$ system prevails. This is due to the relatively rapid damage evolution corresponding to one of the weakest slip systems. *Figure* 4.10 gives the predicted pole figures of the (001) and (100) lattice directions at equivalent strains of 0.5, 1.0, and 1.4. These results match qualitatively those reported in Parks and Ahzi (1990) and Schoenfeld et al. (1995), as shown in *Figure* 4.11. The predicted textures confirm that with an increasing deformation, the (100) poles migrate towards the radial direction while the (001) poles align along the straining direction.

4.5.2 Simple shear

The second simulation corresponds to the simple shear case. The constant velocity gradient is given as

$$\bar{L}_{ij} = \dot{\gamma} \begin{bmatrix} 0.0 & 1.0 & 0.0 \\ 0.0 & 0.0 & 0.0 \\ 0.0 & 0.0 & 0.0 \end{bmatrix}$$

where $\dot{\gamma}$ is equal to 0.003 s^{-1}. Unlike in the tension case, the macroscopic spin is not null. The critical resolved shear stresses and material parameters are shown in *Tables* 4.2 and 4.3. The representative stress-strain curve for single shear is plotted in *Figure* 4.12 and compared with the experimental and numerical responses from G'Sell et al. (1983) and Yang and Chen (2001), respectively. From the figure, it can be seen that the predicted stress-strain behaviour tends to overestimate stresses. For instance, the model overpredicts the initial stress by about 50%. Nevertheless, when compared with Yang and Chen (2001)'s model, our damage-coupled model has the capability of describing much larger

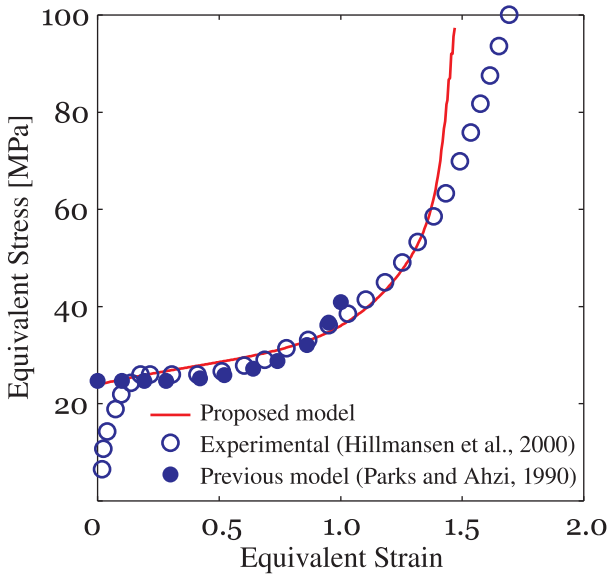

Figure 4.8: Equivalent stress versus equivalent strain behaviour of crystalline polyethylene under uniaxial tension.

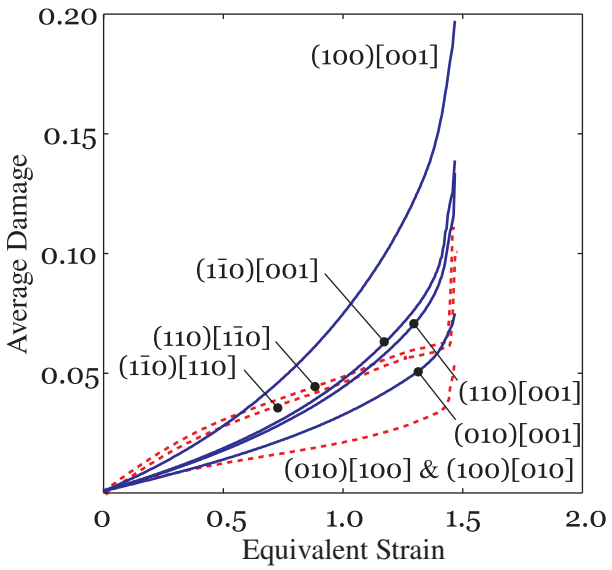

Figure 4.9: Average damage versus equivalent strain for the eight slip systems. Uniaxial tension case.

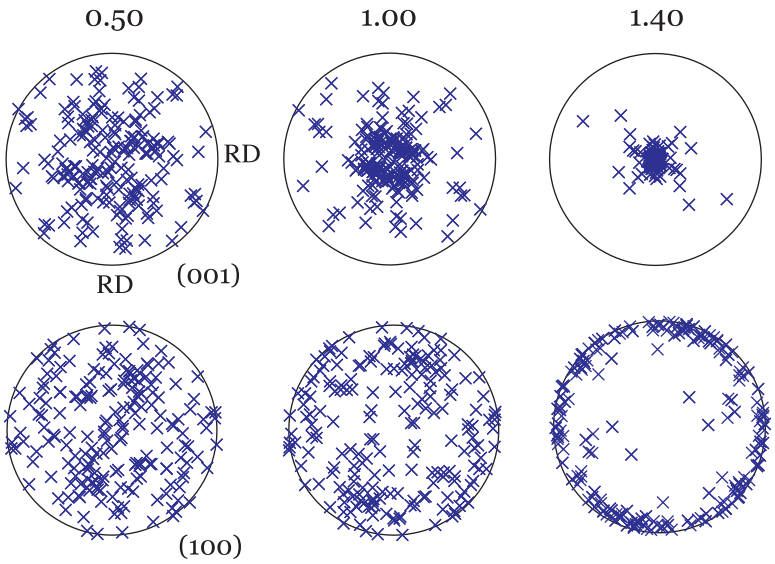

Figure 4.10: Pole figures of the (001) and (100) lattice directions at equivalent strains of 0.5, 1.0, and 1.4. The loading direction is perpendicular to the paper plane.

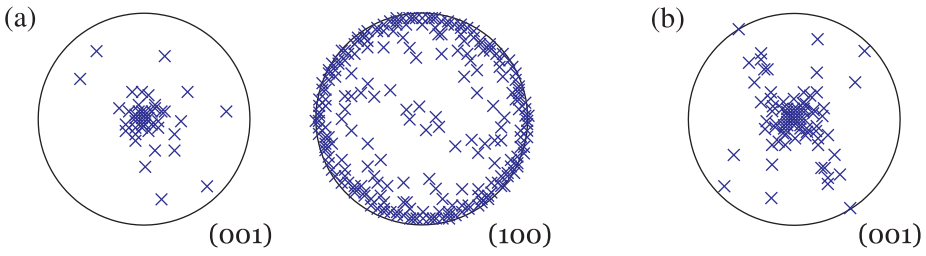

Figure 4.11: Predicted crystallographic textures obtained by (a) Parks and Ahzi (1990) and (b) Schoenfeld et al. (1995) after equivalent strains of 1.0 and 0.9, respectively.

deformations. In addition to significant straining, the curve also reveals that stresses increase moderately between the equivalent strains of 0.0 and 4.5. Afterwards, stresses drop reaching deformations larger than 8.0. As in the uniaxial tension case, the model does not describe the initial elastic behaviour of the material. *Figure* 4.13 illustrates the damage evolution obtained for each available slip system. Damage on the $(1\bar{1}0)[110]$ and $(110)[1\bar{1}0]$ slip systems increases more rapidly than it does on the other systems. Again, the trend of developing anisotropic damage is clearly observed. *Figure* 4.14 gives the predicted pole figures of the (001) and (010) lattice directions at equivalent strains of 2.0, 4.0, and 8.0. In single shear, the (001) poles tend to revolve towards the shear direction while the (010) poles orient perpendicular to that direction. For comparison purposes, *Figure* 4.15 shows the crystallographic textures obtained by Parks and Ahzi (1990) at an equivalent strain of 1.5.

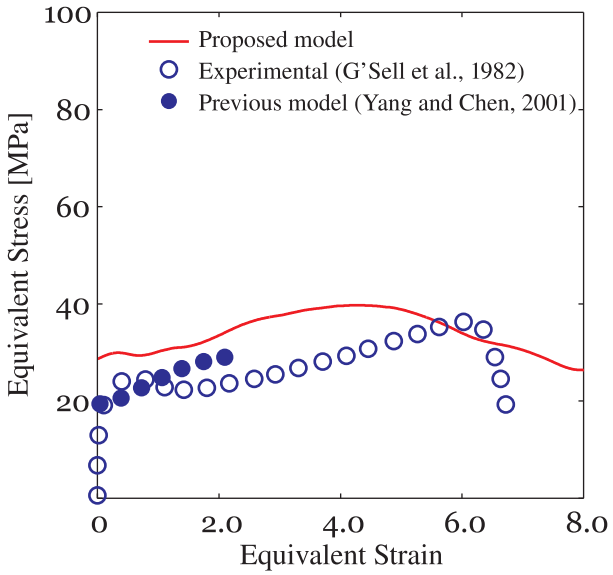

Figure 4.12: Equivalent stress versus equivalent strain behaviour of crystalline polyethylene under simple shear.

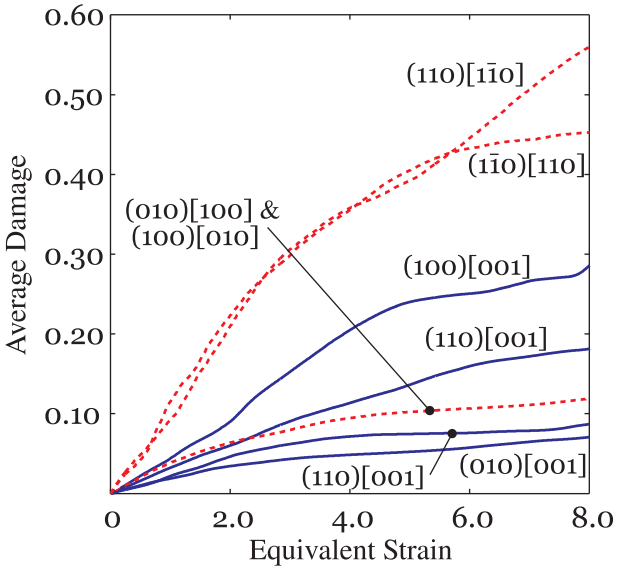

Figure 4.13: Average damage versus equivalent strain for the eight slip systems. Simple shear case.

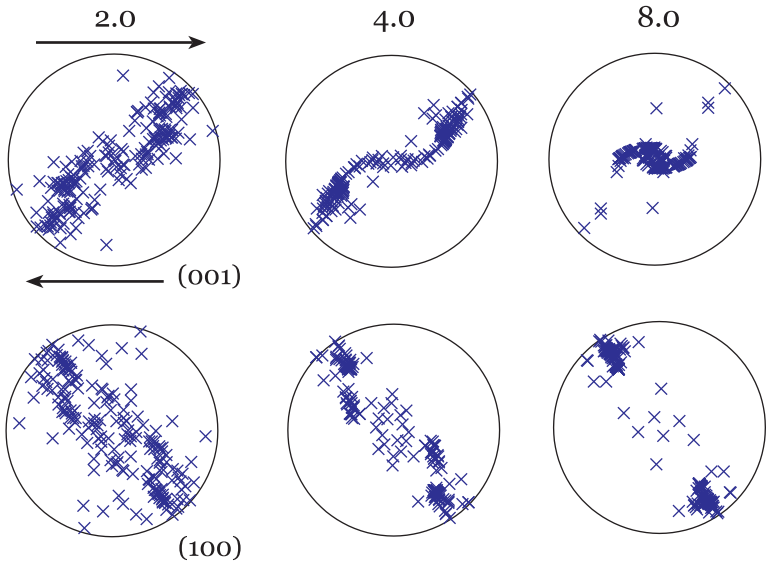

Figure 4.14: Pole figures of the (001) and (100) lattice directions at equivalent strains of 2.0, 4.0, and 8.0. The loading direction is indicated by the arrows.

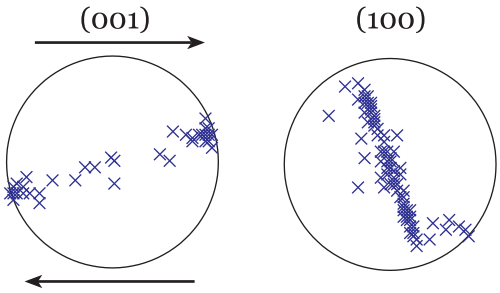

Figure 4.15: Predicted crystallographic textures obtained by Parks and Ahzi (1990) after an equivalent strain of 1.5.

CHAPTER
FIVE

Computational procedure for modelling of crystalline polyethylene[1]

5.1 Introduction

This chapter is concerned with the numerical implementation of the damage-coupled model for crystalline polyethylene proposed in the previous chapter. Consequently, a detailed explanation of the algorithms is given to provide a more general description of material modelling in terms of microstructure evolution. The present chapter is divided into two sections. The first part highlights the most relevant equations of the proposed constitutive law and deals with the main aspects of the numerical integration, whereas the second one gives an overview on the influence of the aggregate description and material parameters on the solutions.

5.2 Solution strategy

An outline of the numerical procedure for solving the constitutive model described in the previous section is presented in this chapter. The aim of the integration algorithm is to find material responses by an incremental procedure associated with discrete time steps. Let $\Delta t \equiv t_{n+1} - t_n$ be a time increment, where t_n and t_{n+1} are two successive times. For each time increment, the two problems to be solved correspond to (*i*) the integration of the constitutive equations to determine local stress states and (*ii*) the integration of the global problem to satisfy compatibility and equilibrium conditions. Since the material

[1]This chapter is based on Alvarado-Contreras et al. (2006a, 2007e)

law involves nonlinear equations, iterative schemes are applied for solving the two problems. Crystal configurations and all internal variables from a previous time increment are given. Crystal and global stresses at time t_{n+1} are obtained by solving the following equation set

$$
\begin{aligned}
D_{ij} &= P_{ijkl}\langle P_{lkmn}\rangle^{-1}\bar{D}_{nm} && (5.1)\\
D_{ij} &= M_{ijkl}S^{*}_{lk} && (5.2)\\
\bar{S}_{ij} &= \langle P_{ijkl}\rangle^{-1}\langle S^{*}_{lk}\rangle && (5.3)\\
\bar{D}_{ij} &= \langle M_{ijkl}\rangle\bar{S}_{lk} && (5.4)
\end{aligned}
$$

Thereafter, the stress-strain state satisfying the global equilibrium conditions for the current time increment is used to integrate the associated internal variables

$$
\begin{aligned}
\frac{dg^{\alpha}}{d\gamma^{\alpha}} &= h_0 \mathrm{sech}^2\left(\frac{h_0}{c}\hat{\gamma}\right) && (5.5)\\
\frac{d\Omega^{\alpha}}{d\tau^{\alpha}} &= \dot{\Omega}_0\left|\frac{\tau^{\alpha}}{(1-\Omega^{\alpha})g^{\alpha}}\right|^{m} && (5.6)
\end{aligned}
$$

and to update the lattice orientations in an implicit way. The algorithm for solving the constitutive model was implemented in computer code. To simplify the following equations and to show how data are stored and processed in the program, we adopt curly $\{\bullet\}$ and square $[\bullet]$ brackets to represent column vectors and matrices, respectively.

5.2.1 Global deformation rate and spin tensors

For the discrete time implementation, a velocity gradient $[\bar{L}]$ is prescribed. As done in crystal plasticity (Asaro and Rice, 1977), global deformation rate and spin are given as the respective symmetric and skew-symmetric components of $[\bar{L}]$. Therefore,

$$[\bar{D}] = \tfrac{1}{2}([\bar{L}] + [\bar{L}]^{\mathrm{T}}) \tag{5.7}$$

and

$$[\bar{W}] = \tfrac{1}{2}([\bar{L}] - [\bar{L}]^{\mathrm{T}}) \tag{5.8}$$

where the superscript T indicates the transpose.

In a polyethylene crystal, slip occurs in four crystallographic planes and in two directions per plane, as shown in *Table* 4.1. It is assumed that the vectors $\{n^\alpha\}$ and $\{s^\alpha\}$ representing the slip systems are perpendicular to one another and remain so with deformation. Therefore, when defined with respect to crystal axes, Schmid tensors are constants with symmetric and skew-symmetric parts, given as

$$[R^\alpha] = \tfrac{1}{2}(\{s^\alpha\}^{\mathrm{T}}\{n^\alpha\} + \{n^\alpha\}^{\mathrm{T}}\{s^\alpha\}) \tag{5.9}$$

and

$$[A^\alpha] = \tfrac{1}{2}(\{s^\alpha\}^{\mathrm{T}}\{n^\alpha\} - \{n^\alpha\}^{\mathrm{T}}\{s^\alpha\}) \tag{5.10}$$

Let a, b, and c be the lattice parameters of the polyethylene unit cell, and let h, k, and l be the Miller indices of a set of normal planes $\{hkl\}$. The expression for describing the normal directions $\{n^\alpha\}$ used in *Equations* 5.9 and 5.10 is given as

$$\{n^\alpha\} = \frac{h/a\{\hat{e}_1\} + k/b\{\hat{e}_2\} + l/c\{\hat{e}_3\}}{\sqrt{(h/a)^2 + (k/b)^2 + (l/c)^2}} \tag{5.11}$$

where $\{\hat{e}_1\}$, $\{\hat{e}_2\}$, and $\{\hat{e}_3\}$ are the three basis vectors. Likewise, let u, v, and w be the Miller indices of the set of slip directions $\langle uvw\rangle$. The equation for identifying the direction vectors $\{s^\alpha\}$ is

$$\{s^\alpha\} = \frac{ua\{\hat{e}_1\} + vb\{\hat{e}_2\} + wc\{\hat{e}_3\}}{\sqrt{(ua)^2 + (vb)^2 + (wc)^2}} \tag{5.12}$$

For computational purposes, symmetric second-order tensors are stored in six-dimensional vectors. For instance, the deformation rate tensor can be written in vector form as

$$\begin{aligned} \{D\} &= \{D_1, D_2, D_3, D_4, D_5, D_6\}^{\mathrm{T}} \\ &= \{D_{11}, D_{22}, D_{33}, \sqrt{2}D_{32}, \sqrt{2}D_{31}, \sqrt{2}D_{21}\}^{\mathrm{T}} \end{aligned} \tag{5.13}$$

Then, by using the following transformation matrix (Lequeu et al., 1987)

$$[T] = \begin{bmatrix} 1/\sqrt{2} & -1/\sqrt{2} & 0 & 0 & 0 & 0 \\ -1/\sqrt{6} & -1/\sqrt{6} & \sqrt{2}/\sqrt{3} & 0 & 0 & 0 \\ 0 & 0 & 0 & 1 & 0 & 0 \\ 0 & 0 & 0 & 0 & 1 & 0 \\ 0 & 0 & 0 & 0 & 0 & 1 \end{bmatrix} \tag{5.14}$$

deviatoric second-order tensors are further reduced to five-dimensional vectors, *e.g.*,

$$\begin{aligned}\{D\} &= \{D_1, D_2, D_3, D_4, D_5\}^{\mathrm{T}} \\ &= \{\sqrt{\tfrac{1}{2}}(D_{11} - D_{22}), \sqrt{\tfrac{3}{2}}D_{33}, \sqrt{2}D_{32}, \sqrt{2}D_{31}, \sqrt{2}D_{21}\}^{\mathrm{T}}\end{aligned} \tag{5.15}$$

Likewise, for the description of skew-symmetric second-order tensors, such as $[\bar{W}]$, the following representation is used (Simo and Hughes, 1998)

$$\{W\} = \{W_1, W_2, W_3\}^{\mathrm{T}} = \{-W_{23}, W_{13}, -W_{12}\}^{\mathrm{T}} \tag{5.16}$$

5.2.2 Crystal orientations

Let $X_1X_2X_3$ and $x_1x_2x_3$ be two orthogonal reference systems with a common origin. The $X_1X_2X_3$ coordinate system provides the sample reference frame with respect to which the global deformation rate and stress are defined. Conversely, the $x_1x_2x_3$ coordinate system is associated with the crystal reference frame and attached to the respective principal lattice axes, as shown in *Figure* 5.1. The relationship between the two systems is expressed in terms of a second-order transformation tensor $[Q]$, whose entries are formed by the scalar components of the lattice vectors $\{a\}$, $\{b\}$, and $\{c\}$. Thus, any crystal orientation can then be expressed in either reference basis by using the following square matrix

$$[Q] = \begin{bmatrix} \{a\}^{\mathrm{T}} \\ \{b\}^{\mathrm{T}} \\ \{c\}^{\mathrm{T}} \end{bmatrix} = \begin{bmatrix} a_1 & a_2 & a_3 \\ b_1 & b_2 & b_3 \\ c_1 & c_2 & c_3 \end{bmatrix} = \begin{bmatrix} Q_{11} & Q_{12} & Q_{13} \\ Q_{21} & Q_{22} & Q_{23} \\ Q_{31} & Q_{32} & Q_{33} \end{bmatrix} \tag{5.17}$$

Given the orthogonality condition of the lattice vectors, there are six dependencies among the nine components of $[Q]$. Thus, only three independent parameters are required for relating the reference and crystal orientations. An alternative scheme for expressing the transformation tensor components is the so-called Euler angles. In this approach, the Euler space $E = \{\varphi, \theta, \psi\}$ is spanned by three rotation angles taken in succession about the reference coordinate system. Here, φ represents a rotation about the X_3 axis, θ is the rotation about the transformed X_2 axis, and ψ is the rotation about the transformed X_3 axis. Thus, the orientation of a certain crystal is fully described by using only trigonometric functions, as follows (Craig, 1989)

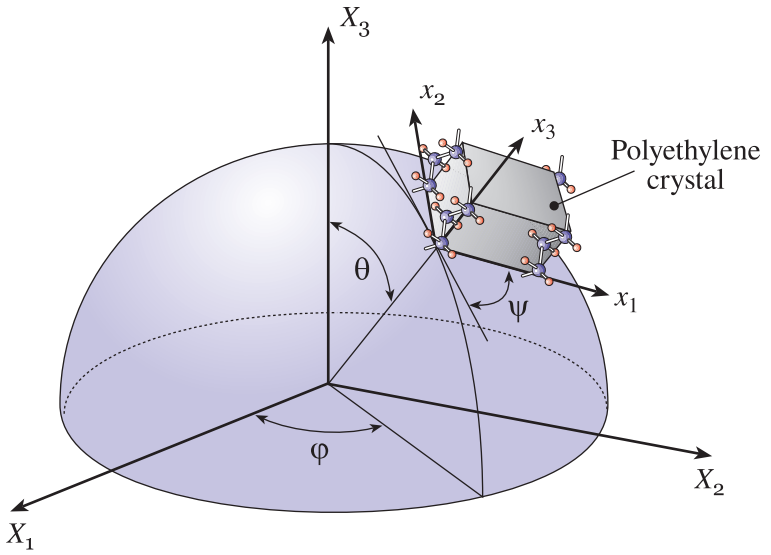

Figure 5.1: Relation between the sample and crystal coordinate systems using Euler angles.

$$[Q] = \begin{bmatrix} \cos\varphi\cos\psi - \sin\varphi\cos\theta\sin\psi & \sin\varphi\cos\psi + \cos\varphi\cos\theta\sin\psi & \sin\theta\sin\psi \\ -\cos\varphi\sin\psi - \sin\varphi\cos\theta\cos\psi & -\sin\varphi\sin\psi + \cos\varphi\cos\theta\cos\psi & \sin\theta\cos\psi \\ \sin\varphi\sin\theta & -\cos\varphi\sin\theta & \cos\theta \end{bmatrix} \tag{5.18}$$

where the three independent rotation ranges are (Morawiec, 2004)

$$0 \leq \varphi < 2\pi, \quad 0 \leq \theta \leq \pi, \quad \text{and} \quad 0 \leq \psi < 2\pi \tag{5.19}$$

For computational purposes, crystal aggregates are assumed to have initially isotropic properties at the macroscopic level. According to this hypothesis, simulations are based on a simple random sampling (Pang, 2006) of crystal orientations, generated by assigning random numbers to the Euler angles. The crystal orientation generator is implemented as follows

1. Generate a set of three numbers $r_i\,(i = 1, 2, 3)$ of random uniform distribution on $[0, 1]$
2. Compute the three Euler angles

$$\varphi = 2\pi r_1, \quad \theta = \cos^{-1}(2r_2 - 1), \quad \text{and} \quad \psi = 2\pi r_3 \tag{5.20}$$

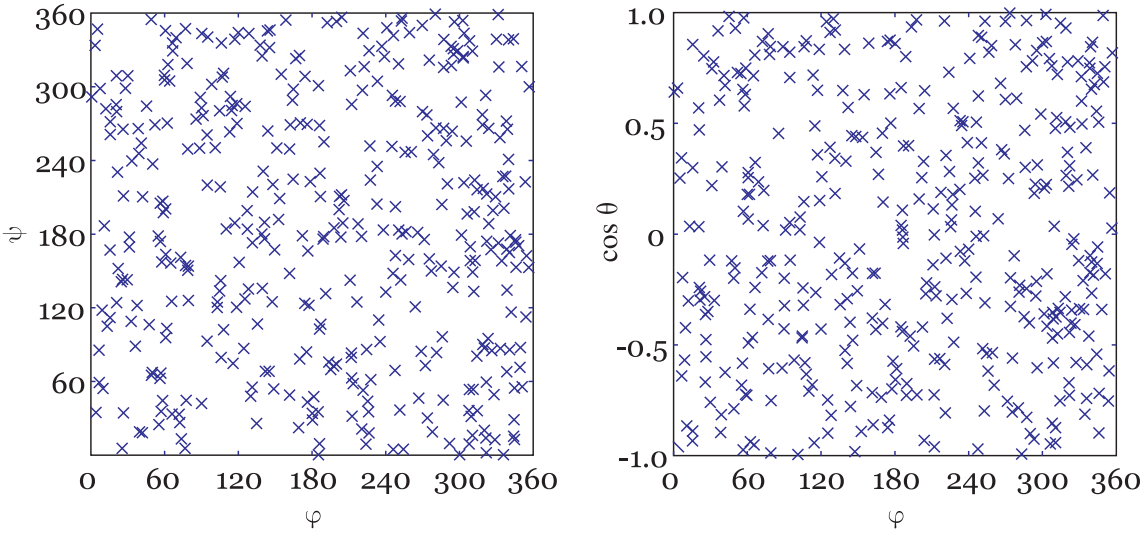

Figure 5.2: Two-dimensional views of the Euler space with the location of 400 randomly oriented crystals.

3. Calculate the corresponding rotation matrix $[Q]$ as given in *Equation* 5.18
4. Repeat steps 1 to 3 to generate the rest of the crystal orientations

The outcome is a series of rotation matrices $[Q]$, which are thought of as representing the crystals in the microstructure of a material point. An example of two-dimensional views of the Euler angles of 400 randomly oriented crystals is given in *Figure* 5.2.

The spatial orientation of some crystallographic planes can be plotted by using a stereographic projection (*e.g.*, Schwarzenbach, 1996). First, it is assumed that crystals lie centred inside a common unit sphere, as the one shown in *Figure* 5.3. Each one of the intersection points of the particular normal vectors with the sphere is identified. Then, the alternative representation is a projection of points from the sphere surface onto a tangential plane to the sphere. If any point on the sphere surface is joined to the reference point N, the line PN cuts the tangential plane at P'. This projection point is the stereographic projection of P. The arrangement of projected points is referred to as a "pole figure". Let X_1, X_2, and X_3 be the coordinates of a point on the sphere, and let X_1' and X_2' be the coordinates of the same point on the projection plane. Then, let $x_1^2 + x_2^2 + x_3^2 = 1$ and $x_3 = -1$ be the equations of the unit sphere and projection plane, respectively. The equation of the line joining the intersection and the projection points can then be written as

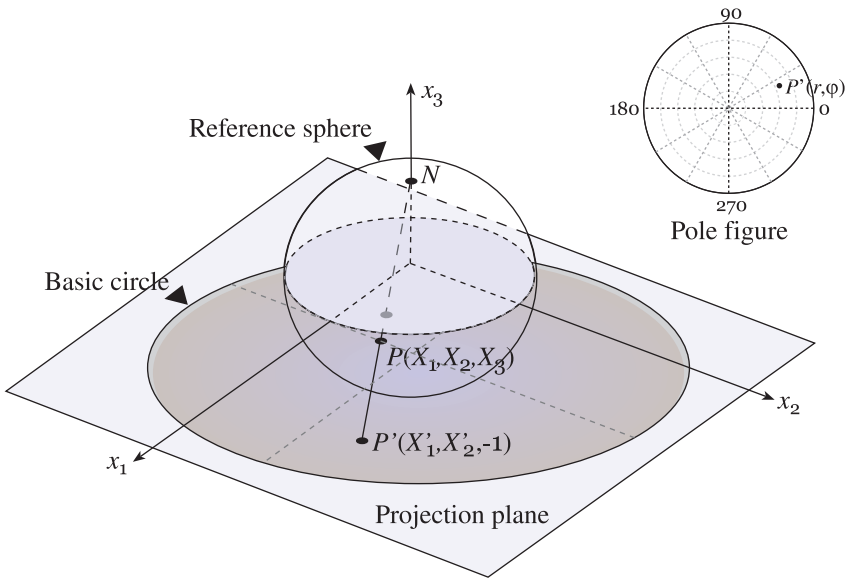

Figure 5.3: Projection of a three-dimensional onto a two-dimension representation (Stereographic projection).

$$\frac{x_1}{X_1} = \frac{x_2}{X_2} = \frac{x_3 - 1}{X_3 - 1} \tag{5.21}$$

Therefore, the intersection point of this line with the projection plane is given as

$$X_1' = -\frac{2x_1}{x_3 - 1}, \qquad \text{and} \qquad X_2' = -\frac{2x_2}{x_3 - 1} \quad (x_3 \neq 1) \tag{5.22}$$

Using a polar coordinate system, the projection points can be defined by a radial coordinate r and a polar angle φ, given in terms of x_1, x_2, and x_3 as

$$r = \frac{2}{x_3 - 1}\sqrt{x_1^2 + x_2^2}, \qquad \text{and} \qquad \tan\varphi = \frac{x_2}{x_1} \quad (x_1 \neq 0) \tag{5.23}$$

From *Figure* 5.3, it is evident that (*i*) the basic circle diameter is twice that of the projected sphere, and (*ii*) a point above the equatorial plane (on the superior hemisphere) projects outside the basic circle, and when the point approaches the reference point N (*i.e.*, $x_3 \to 1$), the projection draws out to infinity. Thus, first, the radial coordinate can be normalized by dividing it by two, and then, points above the equatorial plane can be projected towards the projection plane onto the inferior hemisphere. After that, the radial coordinate is rewritten as

$$r = \frac{1}{|x_3| + 1}\sqrt{x_1^2 + x_2^2} \tag{5.24}$$

5.2.3 Constraint and projection tensors

An aggregate contains a fixed number of crystals denoted by N_c. For each one of the crystals, the inextensible direction $\{c\}$ and the constraint tensor $\{C\}$ can be expressed as

$$\{c\} = \{c_1, c_2, c_3\}^{\mathrm{T}} = \{Q_{31}, Q_{32}, Q_{33}\}^{\mathrm{T}} \tag{5.25}$$

and

$$\begin{aligned} \{C\} &= \{C_1, C_2, C_3, C_4, C_5, C_6\}^{\mathrm{T}} \\ &= \{Q_{31}^2, Q_{32}^2, Q_{33}^2, \sqrt{2}Q_{32}Q_{33}, \sqrt{2}Q_{31}Q_{33}, \sqrt{2}Q_{31}Q_{32}\}^{\mathrm{T}} \end{aligned} \tag{5.26}$$

respectively, where Q_{3i} are the components of the corresponding rotation matrix $[Q]$, as given in *Equations* 5.17 and 5.18.

To calculate the local and global projection tensors, the following steps are applied to each one of the crystals at each time increment:

1. Compute the corresponding deviatoric constraint tensor,

$$\{C'\} = \{C\} - \tfrac{1}{3}\mathrm{tr}\{C\}\{\,I\,\} \tag{5.27}$$

   where $\mathrm{tr}\{C\} = C_1 + C_2 + C_3$, and $\{\,I\,\} = \{1, 1, 1, 0, 0, 0\}^{\mathrm{T}}$

2. Compute the crystal projection tensors,

$$[P_c] = [\,I\,] - \tfrac{3}{2}\{C'\}\{C'\}^{\mathrm{T}} \tag{5.28}$$

   where $[\,I\,]$ is the 6×6 identity matrix

3. Repeat steps 1 and 2 to define the rest of the projection tensors

4. Compute the global average projection tensor,

$$[\bar{P}] = 1/N_c \sum_c [P_c] \tag{5.29}$$

   where the summation is carried out over the total number of crystals in the aggregate, $c = 1, \ldots, N_c$

5. Compute the inverse global projection tensor $[\bar{P}]^{-1}$

5.2.4 Crystal deformation rate and spin tensors

From the global deformation rate, an appropriate partition among the crystals can be derived. If the aggregate is strained at its boundaries at a rate $\{\bar{D}\}$, the local deformation rate $\{D\}$is calculated according to

$$\{D\} = [P_c][\bar{P}]^{-1}\{\bar{D}\} \tag{5.30}$$

where $[P_c]$ and $[\bar{P}]^{-1}$ are the crystal and inverse global projection tensors, respectively. Then, the deformation rate tensor is rotated into the crystal axes by using the transformation

$$\{D_c\} = [\widehat{Q}]\{D\} \tag{5.31}$$

Here, $\{D_c\}$ designates the deformation rate tensor in crystal c, and $[\widehat{Q}]$ is a 5×6 reduced transformation matrix, defined as

$$[\widehat{Q}] = [T][\widetilde{Q}] \tag{5.32}$$

where $[T]$ is the matrix defined in *Equation* 5.14, and $[\widetilde{Q}]$ is a matrix describing the coordinate transformation from the global to the crystal basis, given as

$$[\widetilde{Q}] = \begin{bmatrix} Q_{11}^2 & Q_{12}^2 & Q_{13}^2 & \sqrt{2}Q_{12}Q_{13} & \sqrt{2}Q_{13}Q_{11} & \sqrt{2}Q_{11}Q_{12} \\ Q_{21}^2 & Q_{22}^2 & Q_{23}^2 & \sqrt{2}Q_{22}Q_{23} & \sqrt{2}Q_{23}Q_{21} & \sqrt{2}Q_{21}Q_{22} \\ Q_{31}^2 & Q_{32}^2 & Q_{33}^2 & \sqrt{2}Q_{32}Q_{33} & \sqrt{2}Q_{33}Q_{31} & \sqrt{2}Q_{31}Q_{32} \\ \sqrt{2}Q_{21}Q_{31} & \sqrt{2}Q_{22}Q_{32} & \sqrt{2}Q_{23}Q_{33} & Q_{22}Q_{33}+Q_{23}Q_{32} & Q_{23}Q_{31}+Q_{21}Q_{33} & Q_{21}Q_{32}+Q_{22}Q_{31} \\ \sqrt{2}Q_{11}Q_{31} & \sqrt{2}Q_{12}Q_{32} & \sqrt{2}Q_{13}Q_{33} & Q_{12}Q_{33}+Q_{13}Q_{32} & Q_{13}Q_{31}+Q_{11}Q_{33} & Q_{11}Q_{32}+Q_{12}Q_{31} \\ \sqrt{2}Q_{11}Q_{21} & \sqrt{2}Q_{12}Q_{22} & \sqrt{2}Q_{13}Q_{23} & Q_{12}Q_{23}+Q_{13}Q_{22} & Q_{13}Q_{21}+Q_{11}Q_{23} & Q_{11}Q_{22}+Q_{12}Q_{21} \end{bmatrix}. \tag{5.33}$$

Here, Q_{ij} are the components of the rotation matrix.

5.2.5 Local iterative procedure

At the local level, the procedure is strain-driven. That is, the constitutive equation is used to obtain an estimate of the crystal stress state for a given $\{D_c\}$. After resolving individually all the crystals, the average stress state gives the macroscopic material response. Consider a single crystal subjected to a local deformation rate $\{D_c\}$. Following a Newton-Raphson iterative scheme, the reduced stress $\{S_c^*\}$, the primary unknown, can be determined by solving the following relationship

$$\{D_c\} = [M(S_c^*)]\{S_c^*\} \tag{5.34}$$

During the iterations, updates are carried out on reduced stresses while the internal variables are kept constant and chosen to be the values at time t_n. Therefore, given the most recently updated reduced stress $\{S_c^*\}_k$, the numerical procedure to update the crystal stress state consists of the following steps:

1. Compute the 5×5 crystal compliance tensor

$$[M_c]_k = \dot{\gamma}_0 \sum\nolimits_\alpha \frac{|\{S_c^*\}_k\{R^\alpha\}|^{n-1}}{[(1-\Omega^\alpha)g^\alpha]^n}\{R^\alpha\}\{R^\alpha\}^{\mathrm{T}} \tag{5.35}$$

   where the subscript k identifies the k^{th} iterative approximation. For the first iterative step, $[M_c]_k$ is computed by using an initial guess for the reduced stress.

2. Evaluate the equation system residual,

$$\{H\}_k = \{D_c\} - [M_c]_k\{S_c^*\}_k \tag{5.36}$$

3. Compute the Jacobian matrix,

$$[J]_k = \partial\{H\}_k/\partial\{S_c^*\}_k \tag{5.37}$$

4. Solve the equation system,

$$[J]_k\{\Delta S_c^*\} = -\{H\}_k \tag{5.38}$$

   where $\{\Delta S_c^*\}$ indicates the stress increment between iterations k and $k+1$

5. Compute the new residual $\{H\}_{k+1}$ based on the Newton-Raphson approach,

$$\{H\}_{k+1} = \{H\}_k + [J]_k\{\Delta S_c^*\} \tag{5.39}$$

6. Update the reduced stress,

$$\{S_c^*\}_{k+1} = \{S_c^*\}_k + \{\Delta S_c^*\} \tag{5.40}$$

7. Repeat steps 1 to 6 until the norm of the residual $\|\{H\}_{k+1}\|$ becomes smaller than some adequate tolerance
8. Calculate the reduced stress state in the rest of the crystals using the same approach

5.2.6 Global reduced stress and compliance

The overall response is assumed to be described by a constitutive law similar to that given in *Equation* 5.34. Reduced stress and compliance tensors are determined in the local coordinate systems, and then, rotated onto the reference coordinate system. Assuming that the aggregate is statistically homogeneous, the global stress and compliance are calculated as the respective volume averages of $\{S_c^*\}$ and $[M_c]$ over all the crystals. The volume fraction is given as $v_c = V_c/V$, where V_c and V represent the crystal and aggregate volumes, respectively.

The following steps show how to achieve the global variables.

1. Compute the global compliance tensor,

$$[\bar{M}] = \sum_c v_c [\widehat{Q}_c]^{\mathrm{T}} [M_c] [\widehat{Q}_c] \tag{5.41}$$

2. Compute the global stress,

$$\{\bar{S}^*\} = \sum_c v_c [\widehat{Q}_c]^{\mathrm{T}} \{S^*\} \tag{5.42}$$

3. Compute the global deviatoric Cauchy stress,

$$\{\bar{S}\} = [\bar{P}]^{-1} \{\bar{S}^*\} \tag{5.43}$$

5.2.7 Global iterative procedure

If the global deviatoric Cauchy stress $\{\bar{S}\}$ obtained from *Equation* 5.43 satisfies equilibrium, the solution is accepted, and the next time increment is evaluated. In case of no convergence, corrections based on the successive substitution under-relaxation scheme are performed, and the local iterative procedure is repeated using $\{\bar{S}\}$ as an updated estimate of the stress state for the following step. Once a suitable $\{\bar{S}\}$ is found, it is related

to the global deformation rate $\{\bar{D}\}$ through the relationship $\{\bar{D}\} = [\bar{M}]\{\bar{S}\}$, which can be written in partitioned form as

$$\left\{ \begin{array}{c} \{\bar{D}_g\} \\ \{\bar{D}_u\} \end{array} \right\} = \left[\begin{array}{cc} [\bar{M}]_{11} & [\bar{M}]_{12} \\ [\bar{M}]_{21} & [\bar{M}]_{22} \end{array} \right] \left\{ \begin{array}{c} \{\bar{S}_g\} \\ \{\bar{S}_u\} \end{array} \right\} \tag{5.44}$$

where $\{\bar{D}_g\}$ and $\{\bar{S}_g\}$ are the prescribed components of global deformation rate and deviatoric Cauchy stress, while $\{\bar{D}_u\}$ and $\{\bar{S}_u\}$ are the corresponding deformation and stress components to be calculated in the iterative process. $[\bar{M}]_{11}$, $[\bar{M}]_{12}$, $[\bar{M}]_{21}$, and $[\bar{M}]_{22}$ are compliance tensor partitions obtained from the partition scheme of $\{\bar{D}\}$ and $\{\bar{S}\}$. The following iterative algorithm contains the key steps for integrating the global problem.

1. Obtain the corrected stress corresponding to the prescribed components of $\{\bar{D}_g\}$, along with the condition $\{\bar{S}_g\} = \{0\}$

$$\{\bar{S}_u\}_{k+1} = \omega\,[\bar{M}]_{12}^{-1}\{\bar{D}_g\} + (1-\omega)\{\bar{S}_u\}_k \tag{5.45}$$

   where $\omega \in [0,1]$ is an under-relaxation parameter. The explicit and implicit integrations correspond to $\omega = 0$ and $0 < \omega \leq 1$, respectively (Simo and Hughes, 1998)

2. Compute the global equivalent stress,

$$\hat{\sigma}_{k+1} = \sqrt{\tfrac{3}{2}\{\bar{S}\}_{k+1}^{\mathrm{T}} \cdot \{\bar{S}\}_{k+1}} \tag{5.46}$$

3. Repeat the local and global procedures until the convergence condition $|\hat{\sigma}_{k+1} - \hat{\sigma}_k|$ satisfies the required tolerance. The deformation rate residual is ignored for the solution convergence.

5.2.8 Hardening and damage updating

After achieving global convergence, slip strength and damage values are updated before attempting the next deformation step. The scalar nature of hardening and damage leads to a straightforward integration procedure. In this approach, the integration algorithm consists in:

1. Evaluate the total shear strain,

$$\hat{\gamma}_{n+1} = \sqrt{2\{\bar{D}\}^{\mathrm{T}}\{\bar{D}\}}\,\Delta t + \hat{\gamma}_n \tag{5.47}$$

2. Evaluate the critical resolved shear stresses at t_{n+1},

$$g^{\alpha}_{n+1} = g^{\alpha}_{n} + h_0 \operatorname{sech}^2(h_0 \hat{\gamma}_{n+1}/c)\Delta\gamma^{\alpha} \tag{5.48}$$

3. Obtain the critical resolved shear stresses at $t_{n+\omega}$,

$$g^{\alpha}_{n+\omega} = (1-\omega)g^{\alpha}_{n} + \omega g^{\alpha}_{n+1} \tag{5.49}$$

4. Obtain the resolved shear stress at $t_{n+\omega}$,

$$\tau^{\alpha}_{n+\omega} = (1-\omega)\tau^{\alpha}_{n} + \omega \tau^{\alpha}_{n+1} \tag{5.50}$$

5. Obtain the damage for each slip system at $t_{n+\omega}$,

$$\Omega^{\alpha}_{n+\omega} = (1-\omega)\Omega^{\alpha}_{n} + \omega \Omega^{\alpha}_{n+1}, \tag{5.51}$$

   setting $\Omega^{\alpha}_{n+1} = \Omega^{\alpha}_{n}$ in the first iterative step

6. Compute the damage rate at $t_{n+\omega}$ according to the following damage evolution law:

$$\dot{\Omega}^{\alpha}_{n+\omega} = \begin{cases} \dot{\Omega}_0 \left| \dfrac{\tau^{\alpha}_{n+\omega}}{(1-\Omega^{\alpha}_{n+\omega})g^{\alpha}_{n+\omega}} \right|^{m} & \text{if } \Delta\tau^{\alpha} > 0 \\ 0 & \text{otherwise} \end{cases} \tag{5.52}$$

   where $\Delta\tau^{\alpha} = \left|\tau^{\alpha}_{n+1}\right| - \left|\tau^{\alpha}_{n}\right|$

7. Compute a new approximation for Ω^{α}_{n+1},

$$\Omega^{\alpha}_{n+1}\big|_{k+1} = \Omega^{\alpha}_{n} + \dot{\Omega}^{\alpha}_{n+\omega}\big|_{k} \Delta\tau^{\alpha} \tag{5.53}$$

8. Repeat steps 5 to 7 until $\left|\Omega^{\alpha}_{n+1}\big|_{k+1} - \Omega^{\alpha}_{n+1}\big|_{k}\right|$ becomes smaller than the required tolerance

5.2.9 Crystal orientation updating

Plastic deformation causes a gradual and preferential crystal reorientation (texture), changing significantly the material properties. Assuming that the lattice vectors $\{a\}$, $\{b\}$, and $\{c\}$ rotate at the same lattice spin $[W^*]$, the evolution of the crystallographic axes can be written as (Asaro and Rice, 1977)

$$\{\dot{a}\} = [W^*]\{a\}, \quad \{\dot{b}\} = [W^*]\{b\}, \quad \text{and} \quad \{\dot{c}\} = [W^*]\{c\} \tag{5.54}$$

These are linear homogenous differential equations whose backward-Euler exponential solution over the time increment from t to $t + \Delta t$ can be expressed through, *e.g.*,

$$\{a\}_{n+1} = \exp\left(\Delta t\,[W^*]\right) \cdot \{a\}_n = \exp\left[\mathcal{W}\right] \cdot \{a\}_n \tag{5.55}$$

where the exponential of $[\mathcal{W}]$ is defined and computed numerically by the tensorial power series

$$\exp[\mathcal{W}] = \sum_{k=0}^{\infty} \frac{1}{k!}[\mathcal{W}]^k \tag{5.56}$$

The simplest algorithm for updating the crystal orientations at time t_{n+1} from the corresponding orientations at time t_n is described by the following steps:

1. Evaluate the crystal release function

$$R = \tanh\left(\zeta\hat{\Omega}\right) \tag{5.57}$$

where $\hat{\Omega}$ is the average damage, given as $\hat{\Omega} = \frac{1}{8}\sum_\alpha \Omega^\alpha$

2. Compute the spin tensor at t_{n+1},

$$\{W^*\}_{n+1} = \{W\} - R\{W^p\} \tag{5.58}$$

where $\{W^p\} = \sum_\alpha \dot{\gamma}^\alpha \{A^\alpha\}$, with $\{A^\alpha\}$ vectorized as in *Equation* 5.16

3. Compute the spin tensor at $t_{n+\omega}$,

$$\{W^*\}_{n+\omega} = \omega\,\{W^*\}_n + (1-\omega)\{W^*\}_{n+1} \tag{5.59}$$

4. Compute the incremental spin tensor,

$$\{\mathcal{W}\} = \Delta t\{W^*\}_{n+\omega} \tag{5.60}$$

5. Approximate the exponential function as (*e.g.*, see Chapter 2 of Angeles, 1988)

$$\exp[\mathcal{W}] = [I] + \frac{2}{1+|\{\tilde{w}\}|^2}([\widetilde{W}] + [\widetilde{W}]^2) \tag{5.61}$$

where $\{\tilde{w}\}$ is a unit rotation vector defined as

$$\{\tilde{w}\} = \frac{\{\mathcal{W}\}}{|\{\mathcal{W}\}|}\tan\tfrac{1}{2}\,|\{\mathcal{W}\}| \tag{5.62}$$

and $[\widetilde{W}]$ is a skew-symmetric matrix associated with the $\{\tilde{w}\}$

$$[\widetilde{W}] = \begin{bmatrix} 0 & -\tilde{w}_3 & \tilde{w}_2 \\ \tilde{w}_3 & 0 & -\tilde{w}_1 \\ -\tilde{w}_2 & \tilde{w}_1 & 0 \end{bmatrix} \tag{5.63}$$

6. Update the local rotation tensor

$$[Q]_{n+1} = [Q]_n \cdot \exp^{\mathrm{T}}[\mathcal{W}] \tag{5.64}$$

7. Repeat steps 1 to 6 to update the rest of the rotation tensors

5.3 Numerical examples

A number of simulations illustrate the performance of the algorithm described in the previous section. For the tension loading case, it is assumed that deformation is imposed along the sample X_2-direction. Global spin is null, and global deformation rate and deviatoric stress are of the following reduced forms

$$\{\bar{D}\} = \{?, \bar{D}_2, ?, ?, ?, ?\}^{\mathrm{T}}, \text{ and } \{\bar{S}\} = \{?, ?, ?, 0, 0, 0\}^{\mathrm{T}} \tag{5.65}$$

where $\bar{D}_2$ is the enforced deformation rate. The shear stress components $\bar{S}_4$, $\bar{S}_5$, and $\bar{S}_6$ are assumed to be null. The rest of the non-prescribed components, written as question marks, are the associated unknowns. However, due to the loading conditions and the deviatoric nature of the deformation rate, the components along the transverse direction can be written as

$$\bar{D}_1 = \bar{D}_3 = -\tfrac{1}{2}\bar{D}_2 \tag{5.66}$$

Note that the condition $\bar{D}_4 = \bar{D}_5 = \bar{D}_6 = 0$ is not satisfied; consequently, the compatibility conditions are partially fulfilled. In the stress tensor, normal components are unknown; however, as in $\{\bar{D}\}$, it can be assumed that

$$\bar{S}_1 = \bar{S}_3 = -\tfrac{1}{2}\bar{S}_2 \tag{5.67}$$

All the simulations were carried out for aggregates of 250 randomly oriented orthorhombic crystals of the same volume. Unless indicated otherwise, the model and material parameters used in the simulations are those listed in *Table* 5.1. The critical shear strengths are taken as proposed in Parks and Ahzi (1990).

Table 5.1: Material parameters for the simulations.

Parameter	Uniaxial tension
Strain rate sensitivity, n	5.0
Reference strain rate, $\dot{\gamma}_0$ [s^{-1}]	0.001
Damage rate sensitivity, m	2.0
Reference damage rate, $\dot{\Omega}_0$ [MPa^{-1}]	0.05
Hardening modulus, h_0 [MPa/s]	6.0
Saturation shear strength, c [MPa]	23.0
Spin release, ζ	30.0
Under-relaxation parameter, ω	0.5
Time increment, Δt [s]	5.0
Error tolerance	1.0×10^{-6}

5.3.1 Influence of the number of crystals

In order to investigate the solution dependence on the number of crystals, 180 samples were simulated. These samples were grouped into nine sets of 20 different aggregates characterizing initially isotropic material points. The sets represent successive enlargement of the number of crystals. Each aggregate was generated by changing the crystal orientations, as described in *Section* 5.2.2. Simulations were performed on the samples by using identical model parameters and incremental displacements. The simulations were carried out at a deformation rate $\bar{D}_2$ of 1×10^{-3}/s. The effect of the number of crystals on compliances was analyzed. *Figure* 5.4 shows the compliance ratio $\bar{M}_{33}/\bar{M}_{11}$ versus the number of crystals at equivalent (inelastic) strains of 0.0 and 1.0. Likewise, *Figure* 5.5 illustrates similar plots, but in this case for the compliance ratio $\bar{M}_{11}/\bar{M}_{22}$. From the results, it can be seen that the band of the simulated ratios diminishes rapidly reaching a steady width as the number of crystals increases. As can be seen, at least 100 crystals are required to homogenize the material compliance (orientation dependence disappears on the average) and to attain a reasonable representation of the aggregate. For example, for the set of aggregates with 250 crystals, the mean values of the ratio $\bar{M}_{33}/\bar{M}_{11}$ at the equivalent strains of 0.0 and 1.0 are 0.991 and 0.989, respectively. In both cases, the mean

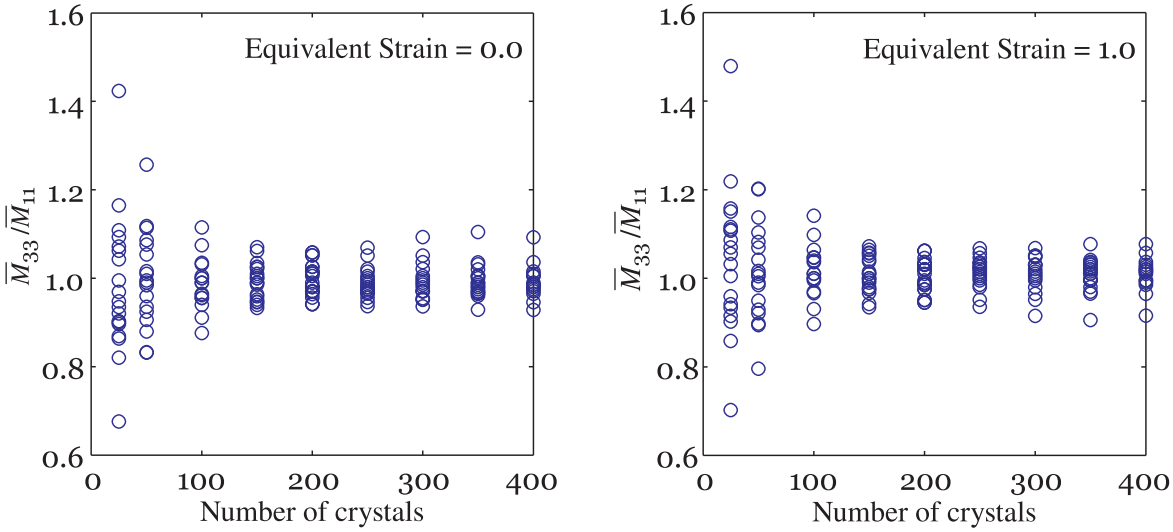

Figure 5.4: Global compliance ratio $\bar{M}_{33}/\bar{M}_{11}$ versus number of crystals at the equivalent strains of 0.0 and 1.0.

values lie fairly close to the theoretical value of 1.0. On the other hand, the mean values of the ratio $\bar{M}_{11}/\bar{M}_{22}$ at the same strains are 0.523 and 0.630. As expected, the mean values illustrate how the ratio increases as material anisotropy evolves.

5.3.2 Influence of the crystal orientation

Probability plots and statistical distributions for a selection of normal and shear stresses at an equivalent deformation of 1.0 are presented. *Figure* 5.6 shows the probability plots used for assessing graphically whether the local stresses follow a theoretical distribution. The stresses were plotted against a normal distribution. Based on the point patterns, it appears that the stresses reasonably fit the presupposed distribution. Therefore, although a few points show departures from the fitted lines, the assumption of normality seems be reasonable for comparing the effects of initial crystal orientations on the overall macro-response of the aggregate. *Figure* 5.7 shows the normal distributions fitted to the S^*_{11}, S^*_{22}, and S^*_{12} components for 20 aggregate samples. All examples were performed under the same loading conditions and material constants given in *Table* 5.1. Each aggregate contains a total of 250 crystals differently oriented from sample to sample. As expected, the distributions show that the mean axial stress $\bar{S}^*_{22}$ is positive ranging from 12.92 to 14.67 MPa. The mean transverse stress $\bar{S}^*_{11}$ is negative and ranges from -7.47 to -6.31 MPa. Similarly, the mean shear stress $\bar{S}^*_{12}$ is approximately zero, varying from -0.33 to 0.38 MPa.

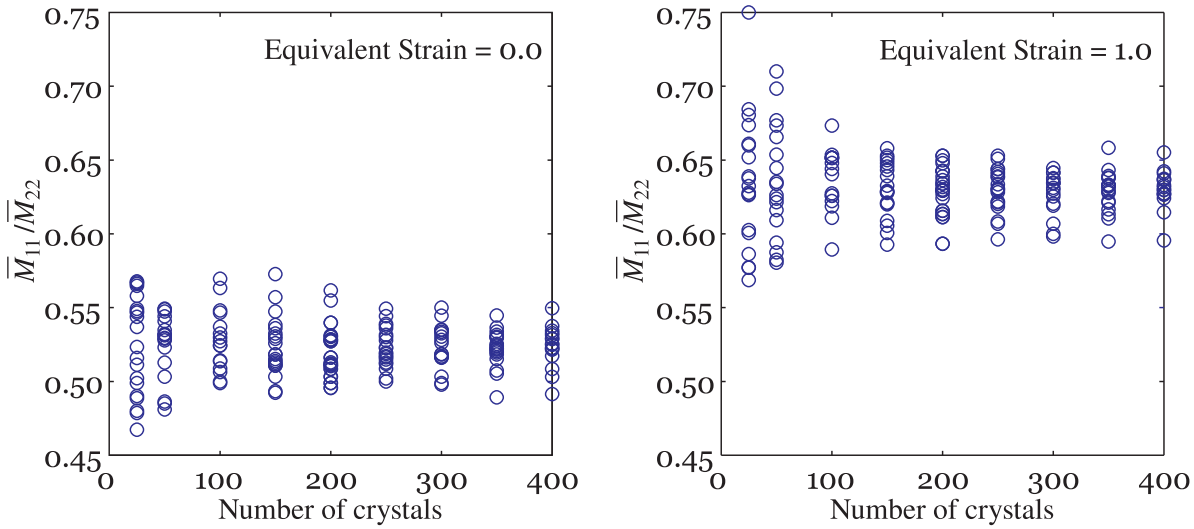

Figure 5.5: Global compliance ratio $\bar{M}_{11}/\bar{M}_{22}$ versus number of crystals at the equivalent strains of 0.0 and 1.0.

Respectively, for the three components, the standard deviations range from 5.19 to 6.13 MPa, from 4.76 to 5.71 MPa, and from 6.61 to 7.82 MPa. The results obtained show that crystal orientations in an isotropic and representative large aggregate do not have a considerable influence on the prediction of the reduced stress components. Similarly, *Figure* 5.8 illustrates the normal distributions of three simulations performed on a 250 crystal aggregate. In these simulations, loading was applied alternately along one of the three principal sample directions, while keeping crystal orientations invariant for each case. It is apparent from the distributions shown that the resulting stress states are not affected significantly by the loading direction in an initially isotropic aggregate.

5.3.3 Influence of the material parameters

Further insight into the model can be gained by considering the influence of the different material parameters on the simulated mechanical behaviour of crystalline polyethylene. Here, the simulations do not attempt to capture quantitatively all experimental details, but instead, to predict the influence of four new adjustable material parameters in stress and damage evolution. Other parameter combinations might lead to better agreement with experimental results, yet parameter estimation by using appropriate statistical and optimization algorithms is beyond the scope of this chapter. As measures of stress and strain, the equivalent forms were calculated in the simulations; therefore,

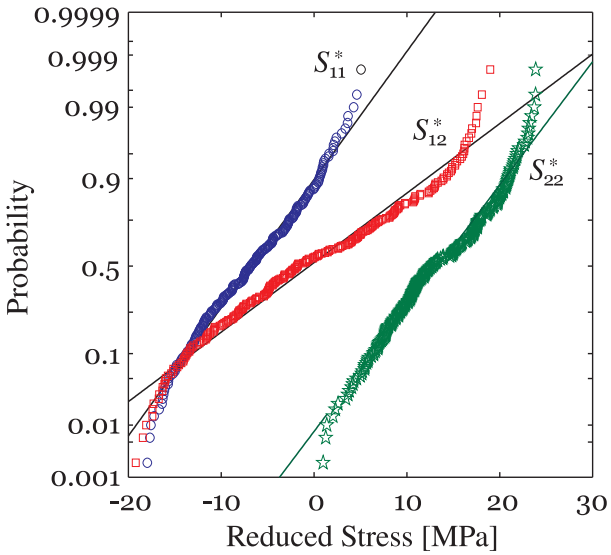

Figure 5.6: Probability distribution of the S_{11}^*, S_{22}^*, and S_{12}^* stress components on a 250-crystal aggregate.

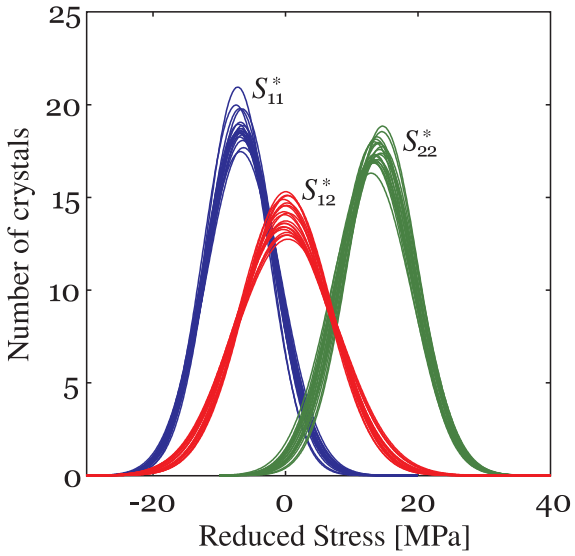

Figure 5.7: Normal distributions showing the aggregate effects on a selection of reduced stress components.

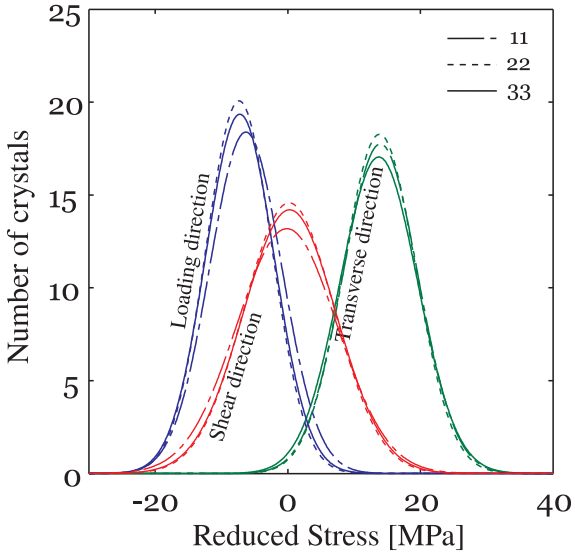

Figure 5.8: Normal distributions showing the loading direction effects on a selection of reduced stress components.

$$\hat{\sigma} = \sqrt{\tfrac{3}{2}\bar{S}_{ij}\bar{S}_{ij}} \tag{5.68}$$

and

$$\hat{\varepsilon} = \int_0^t \sqrt{\tfrac{2}{3}\bar{D}_{ij}\bar{D}_{ij}}\, dt \tag{5.69}$$

The material parameters considered for the analysis are the damage rate $\dot{\Omega}_0$, hardening modulus h_0, saturation shear strength c, and release ζ. All subsequent plots are obtained at the same deformation rate of 1×10^{-3}/s. First, we focus on the damage rate. The effects of five trial values of $\dot{\Omega}_0$ on material hardening are illustrated in *Figure* 5.9. The figure shows the predicted stress-strain curves and damage evolution for the (100)[001] slip system for the given rates. The curves reveal a significant influence of damage rate on material response. The most noteworthy feature is the straining level where the curves exhibit the sharp stress upturn. It is easy to see that the higher the $\dot{\Omega}_0$, the more limited the deformation, and for strains below 1.0, the lower the stress. Minor changes in the initial tangent modulus $\partial\sigma/\partial\varepsilon$ were observed. *Figure* 5.10 compares four simulated textures corresponding to the (001) and (100) lattice directions at an equivalent strain of 1.5. It can be seen that damage rate has also an important influence on the development of texture. For instance, it is observed in *Figure* 5.10 that as $\dot{\Omega}_0$ increases, the (001) and (100)

poles rotate more rapidly towards the respective loading and transverse directions. The strongest texture was presented for $\dot{\Omega}_0 = 0.1$. *Figure* 5.11 shows the same lattice directions at an equivalent stress of 40 MPa, revealing that damage rate variations have negligible effects on textures when compared at an identical equivalent stress. Stress-strain and damage plots illustrating the effects of hardening modulus h_0 are given in *Figure* 5.12. The results show that material behaviour depends on h_0 quite significantly. It should be noted that, as h_0 increases, the tangent modulus $\partial\sigma/\partial\varepsilon$ at zero inelastic strain increases, and the material becomes more highly stressed. Furthermore, for this particular example, it is indicated that the stress-strain and damage plots come near a maximum as h_0 approaches 40 MPa/s. In *Figure* 5.13, the corresponding pole figures for the different hardening rates are plotted. The comparison of the predicted poles clearly shows the influence on the migration rate of the (001) and (100) poles, for an equivalent strain of 1.5. *Figure* 5.14 shows how the predicted poles are not far from each other when compared at the same stress level of 40 MPa. Additionally, note the nearly coinciding textures of *Figures* 5.11 and 5.14. In a manner analogous to the analyses for the damage rate and hardening modulus, the overall behaviour for different values of saturation shear strength c were assessed, as shown in *Figure* 5.15. The results illustrate that as c increases from 1.5 to 30, the overall stress levels rise rapidly and damage values climb sharply. Additionally, the stress plateau disappears gradually when c is beyond 3.0. Nevertheless, the initial tangent modulus $\partial\sigma/\partial\varepsilon$ does not vary by a significant amount among the curves. Comparisons of the pole figures are outlined in *Figures* 5.16 and 5.17. As in previous cases, the choice of c also has a marked effect on the texture development. Moreover, *Figure* 5.17 shows that saturation shear strength has also an important influence on texture even when poles are compared at the same stress level. This peculiarity can be attributed to the fact that the model considers equal saturation shear strength for all slip systems. Finally, *Figures* 5.18 to 5.20 show how an increasing release parameter ζ influences stress and damage evolution as well as texture. Similar conclusions to the ones discussed for the previous cases can be drawn.

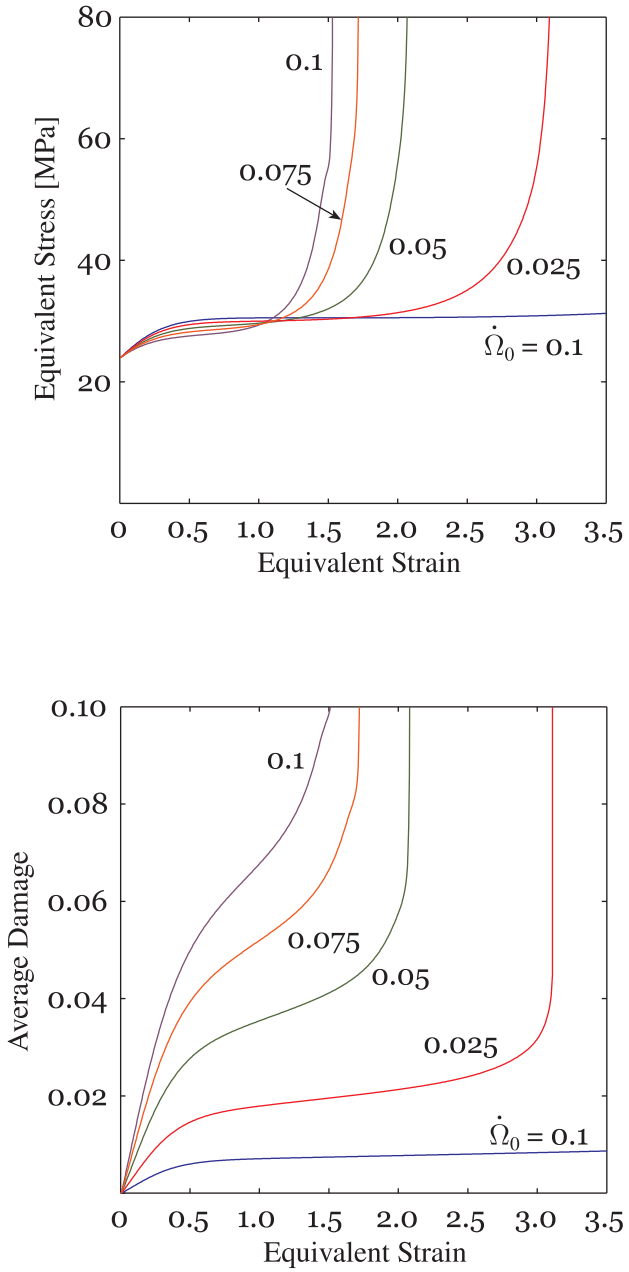

Figure 5.9: Curves revealing effects of increasing damage rate values $\dot{\Omega}_0$ on (*top*) the stress-strain behaviour and (*bottom*) the average damage for the (100)[001] slip system. (Material parameters used: h_0=10, c=6, and ζ = 20).

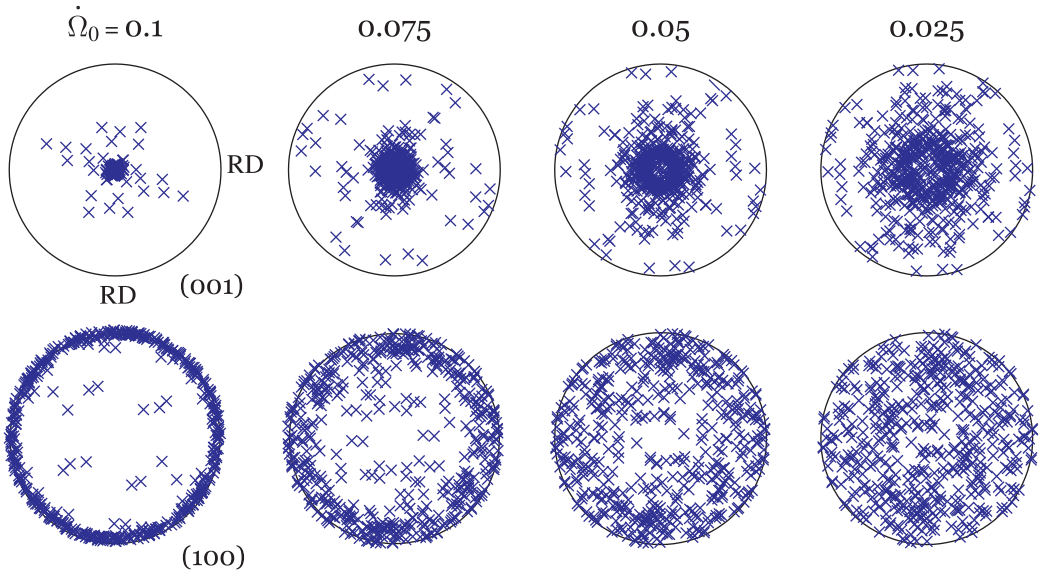

Figure 5.10: Pole figures of the (001) and (100) lattice directions at an equivalent strain of 1.5 for four different values of damage rate $\dot{\Omega}_0$. The loading direction is perpendicular to the paper plane.

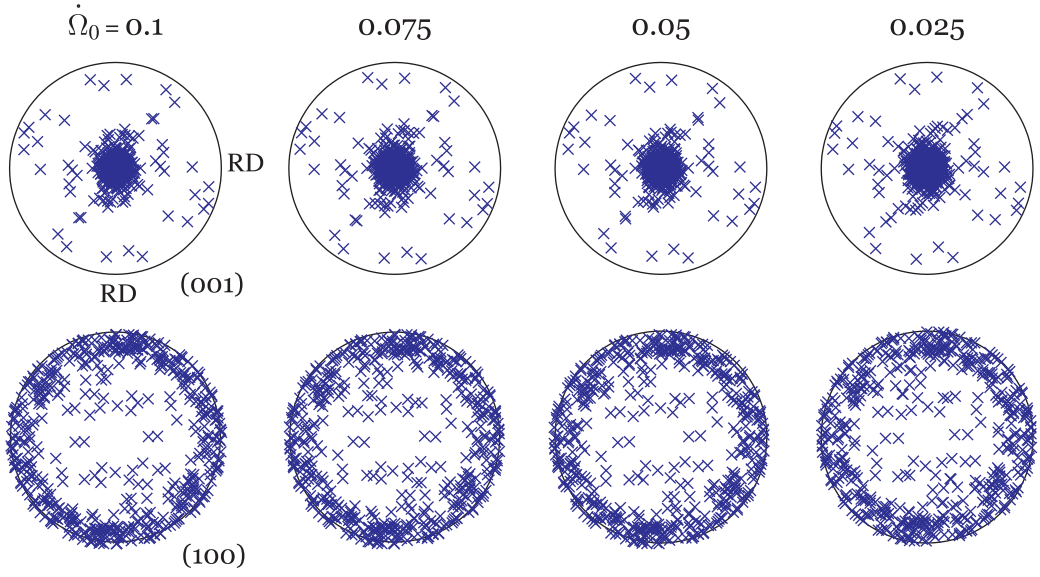

Figure 5.11: Pole figures of the (001) and (100) lattice directions at an equivalent stress of 40 MPa for four different values of damage rate $\dot{\Omega}_0$.

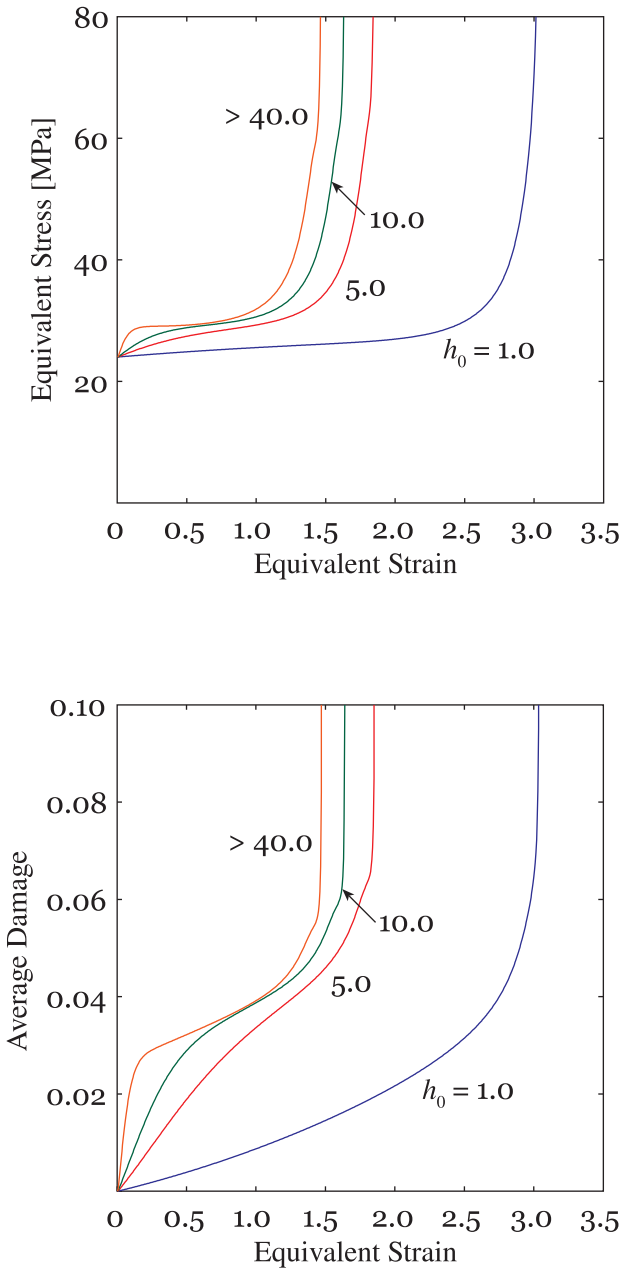

Figure 5.12: Curves revealing effects of increasing hardening rate values h_0 on (*top*) the stress-strain behaviour and (*bottom*) the average damage for the (100)[001] slip system. (Material parameters used: $\dot{\Omega}_0$=0.05, c=6, and ζ = 30).

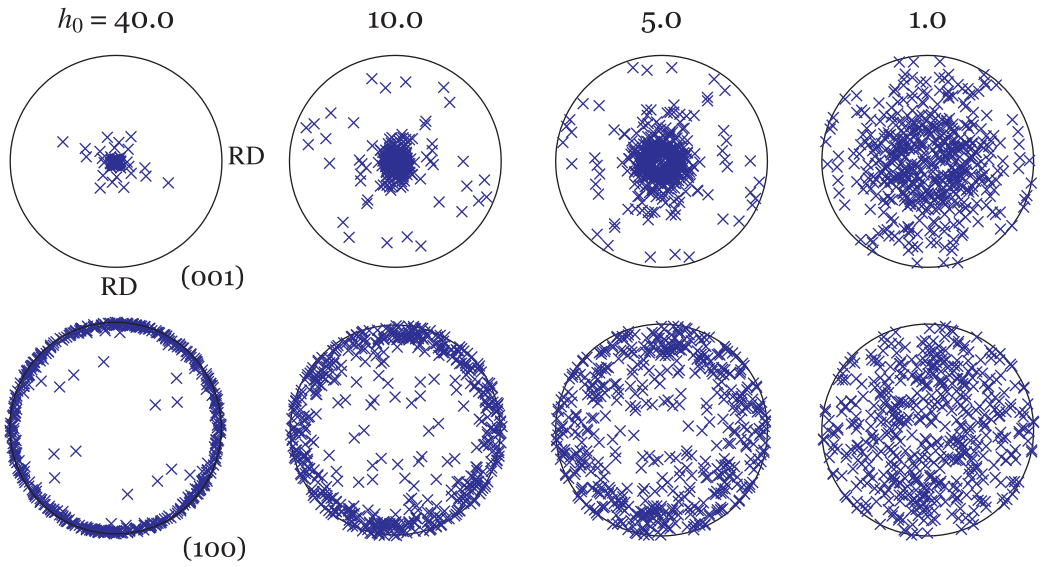

Figure 5.13: Pole figures of the (001) and (100) lattice directions at an equivalent strain of 1.5 for four different values of hardening rate h_0.

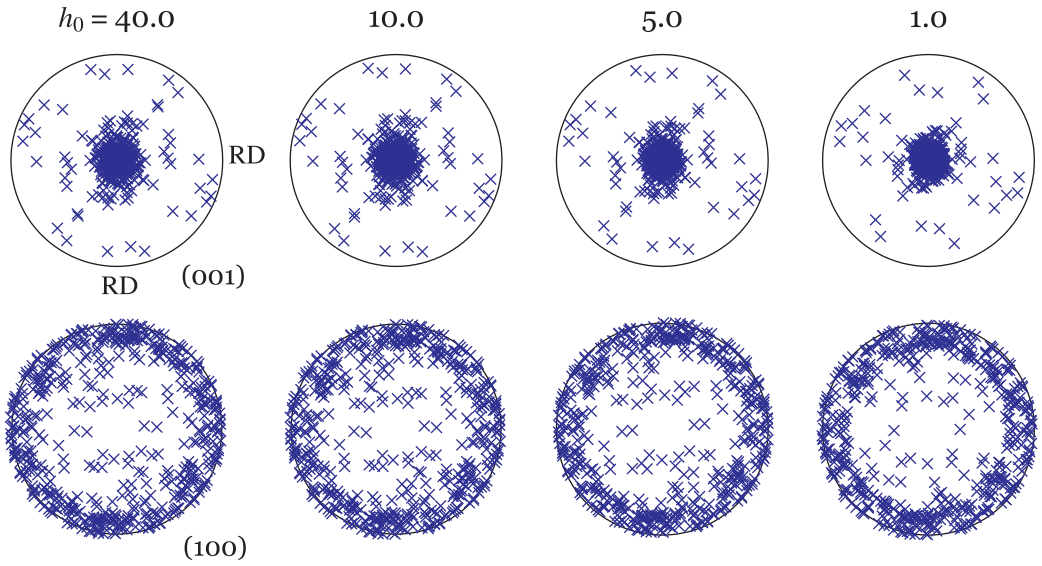

Figure 5.14: Pole figures of the (001) and (100) lattice directions at an equivalent stress of 40 MPa for four different values of hardening rate h_0.

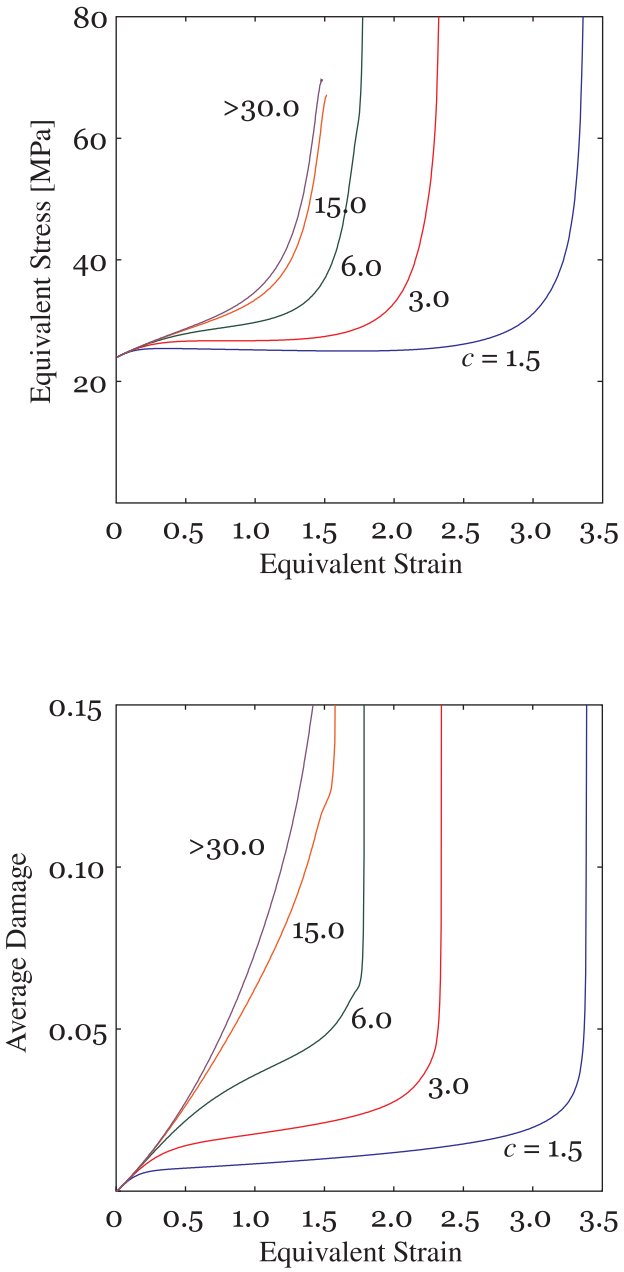

Figure 5.15: Curves revealing effects of increasing hardening rate values c on (*top*) the stress-strain behaviour and (*bottom*) the average damage for the (100)[001] slip system. (Material parameters used: $\dot{\Omega}_0$=0.05, h_0=6, and ζ = 30).

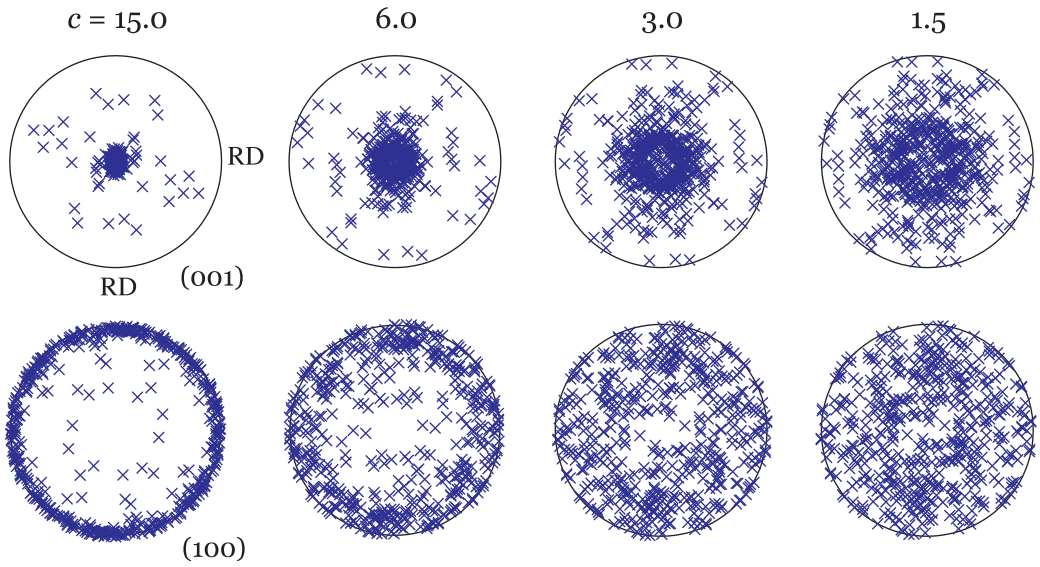

Figure 5.16: Pole figures of the (001) and (100) lattice directions at an equivalent strain of 1.5 for four different values of saturation shear strength c.

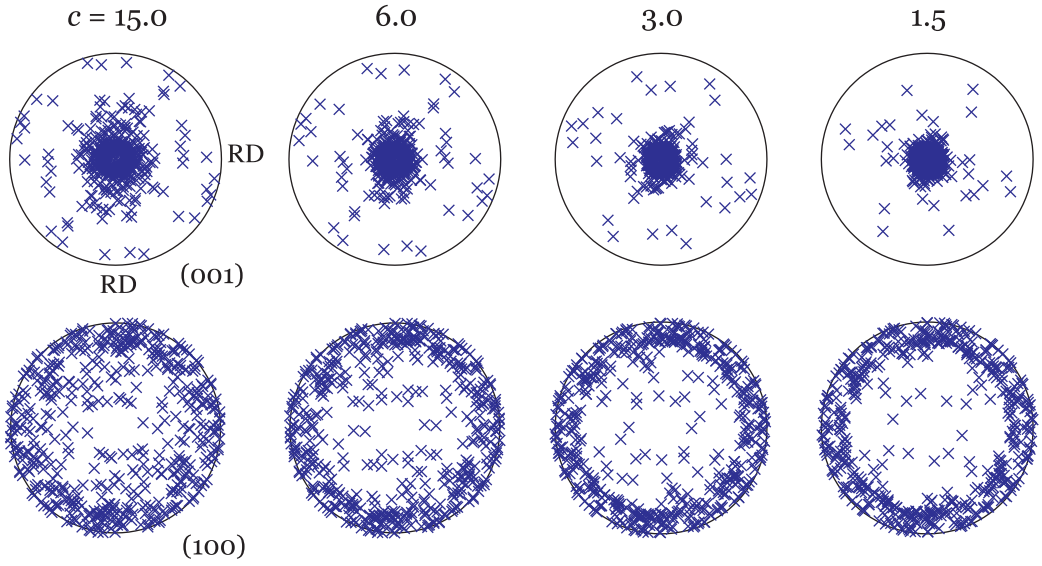

Figure 5.17: Pole figures of the (001) and (100) lattice directions at an equivalent stress of 40 MPa for four different values of saturation shear strength c.

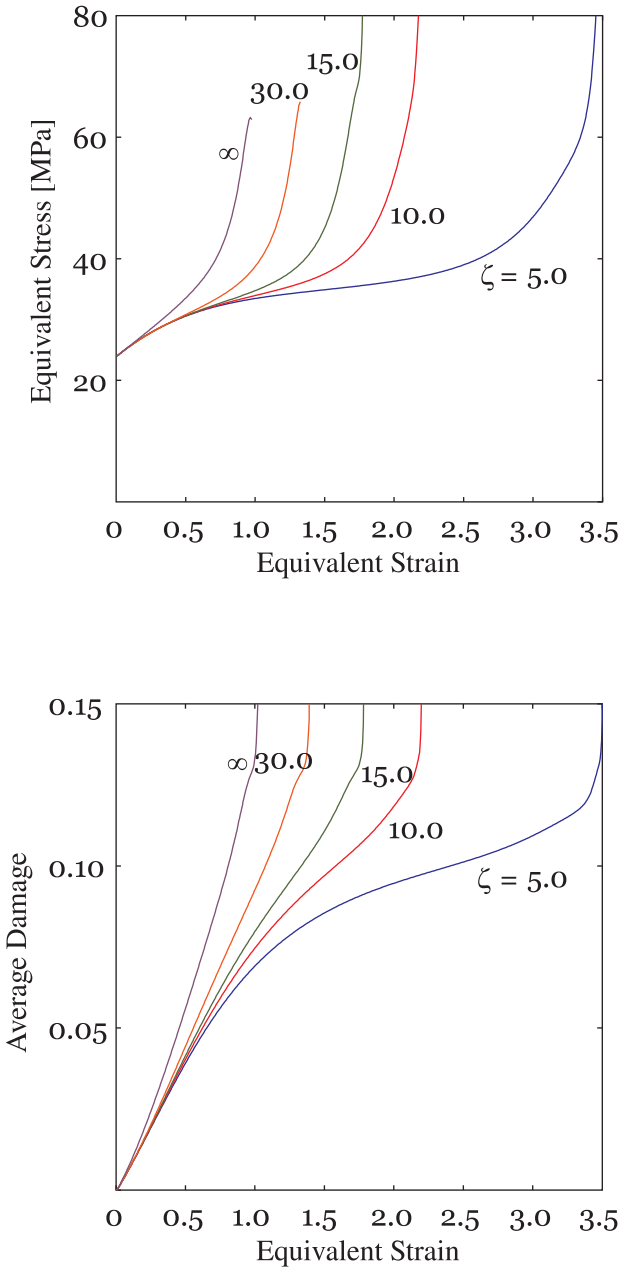

Figure 5.18: Curves revealing effects of rotation release values ζ on (*top*) the stress-strain behaviour and (*bottom*) the average damage for the (100)[001] slip system. (Material parameters used: $\dot{\Omega}_0$=0.05, h_0=10, and c = 15).

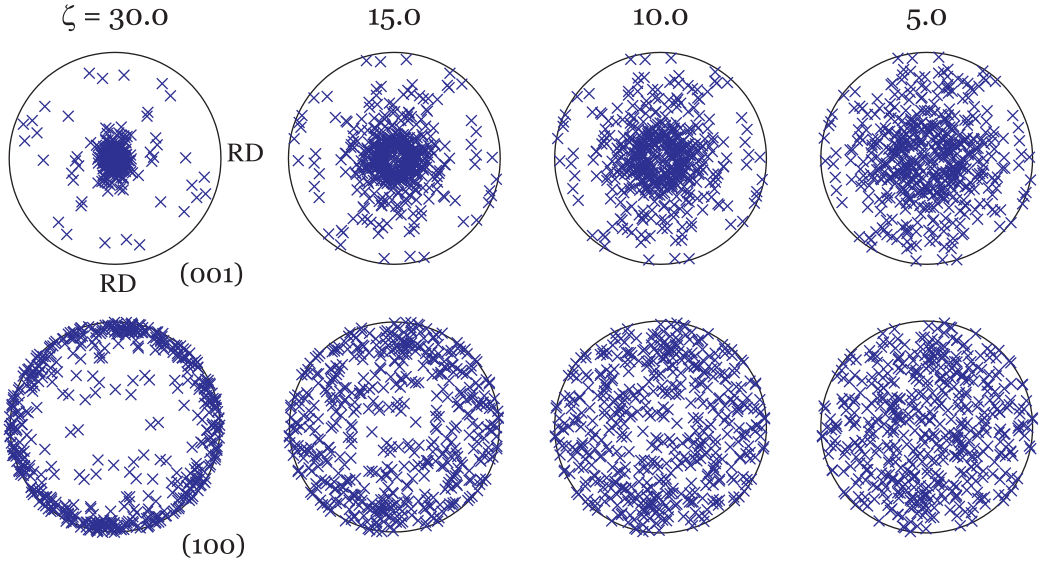

Figure 5.19: Pole figures of the (001) and (100) lattice directions at an equivalent strain of 1.5 for four different values of rotation release ζ.

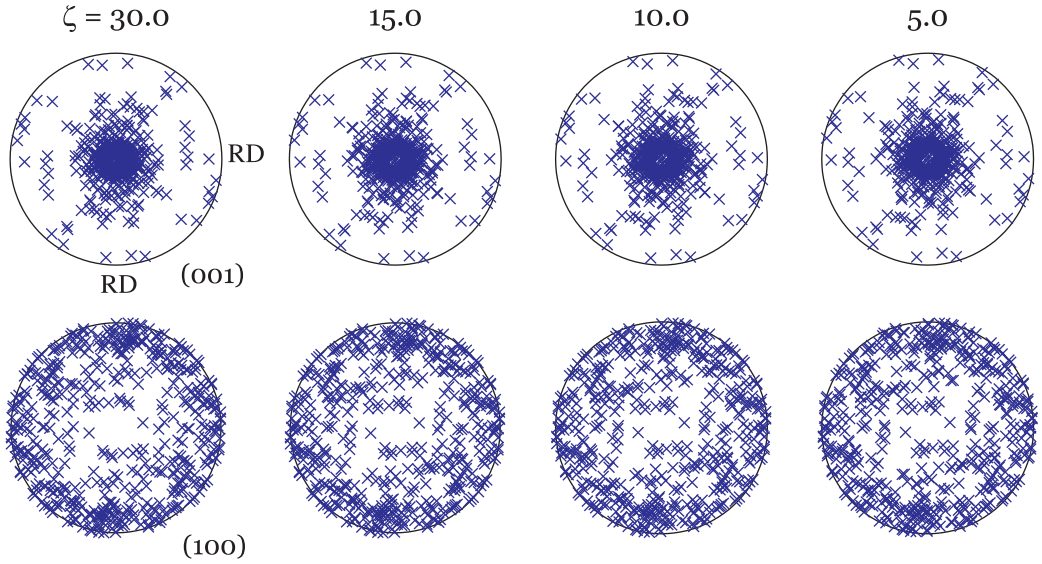

Figure 5.20: Pole figures of the (001) and (100) lattice directions at an equivalent stress of 40 MPa for four different values of rotation release ζ .

CHAPTER
SIX

Damage-coupled model for semicrystalline polyethylene

6.1 Introduction

In this chapter, a detailed description of the proposed constitutive formulation for the mechanical behaviour of semicrystalline polyethylene is presented. The model attempts to describe the deformation and degradation processes in polyethylene following a Continuum Damage Mechanics approach and considering the interplay between the crystalline and amorphous phases. For the crystalline phase, the proposed model is similar to the one introduced in *Chapter* 4. For the amorphous phase, the constitutive model is developed within a thermodynamic framework able to describe the features of the material behaviour. Hardening of the amorphous phase is considered into the model and associated to different molecular configurations arising during the deformation process, as suggested by Arruda and Boyce (1993). The equation governing the evolution of damage in the amorphous phase is obtained by choosing a particular form based on the internal energy and entropy. The model generated within this damage-coupled framework is used to simulate uniaxial tension and simple shear of a high density polyethylene. The model predictions are compared with the experimental results reported by G'Sell and Jonas (1981) and G'Sell et al. (1983) and with the numerical simulations obtained by Lee et al. (1993b) and Nikolov et al. (2006).

6.2 Thermodynamic framework

The structure morphology of amorphous polyethylene can be regarded as a sort of randomly oriented molecular chains connected by physical entanglements. When deformed

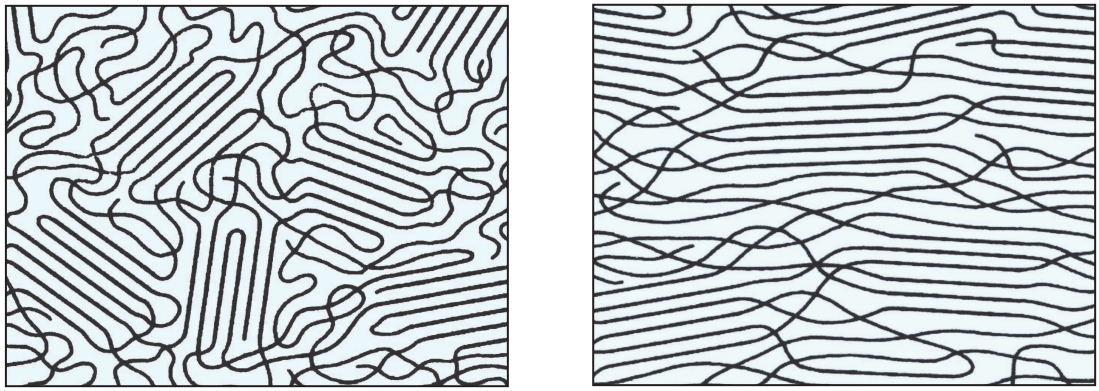

Figure 6.1: Representation of a semicrystalline polymeric material showing the amorphous phase structure in the (left) unstrained and (right) strained states (Treloar, 1975).

below its glass transition temperature ($T_g \approx -70°\text{C}$), amorphous polyethylene is considered relatively rigid, stiff, and brittle. In contrast, above T_g, it becomes softer elastically and tougher plastically. During stretching and once intermolecular resistances are overcome, molecular chains have the freedom to rearrange and reorient themselves towards the direction of maximum stretch, as illustrated in *Figure* 6.1. For a nonlinear analysis of the mechanical behaviour, amorphous polyethylene has been classically considered isotropic, incompressible, and rubber-like.

The equations required to describe the mechanical response as well as the processes and changes occurring at the microstructural level are obtained in terms of classical thermodynamics and statistical mechanics (Treloar, 1975). For describing the stress-strain response of amorphous polyethylene, the energies controlling the variety of processes and changes at the microstructural level are of particular interest. Let us consider as *a system* the amorphous material to be analyzed. The first law of thermodynamics, a consequence of conservation of energy, states the interconvertibility of mechanical and thermal energies through the following postulate:

> *The change in the internal energy of a thermodynamic system is equal to the sum of the heat energy exchanged with the surroundings and the work done on the system.*

A mathematical approach to this conservation law can be written as

$$du = dq + dw, \tag{6.1}$$

where u, q, and w are the internal energy, the heat absorbed or released by the system, and the work done on it by external forces, respectively.

At a molecular level, the second law of thermodynamics states that a system always tends to change to a more disordered state. Therefore, energy tends to be transformed into lower levels of availability before reaching a state of unavailability for further work. The irreversibility condition given by the second law of thermodynamics states that:

> *In all energy exchanges, if no energy enters or leaves the system, the energy of the state will always be less than that of the initial state.*

The central property of the second law is entropy, which is thought of as a measure or index of the randomness of a system. Entropy is defined as

> *a function of the thermodynamic state of a system whose change in any reversible process is equal to the energy dissipated at a temperature T.*

On the basis of the second law of thermodynamics, the expression for the entropy change of a system is given as the energy transferred as heat divided by the absolute temperature (on the Kelvin scale) at which the transfer takes place; thus,

$$ds = \frac{dq}{T} \tag{6.2}$$

Since T is always positive, ds has the same sign as that of dq. Entropy change can be additively decomposed into two components; one related to the flux due to energy flow s_e, and the other related to the internal entropy production due to irreversible processes s_i (Nicolis and Prigogine, 1977); that is,

$$ds = ds_e + ds_i \tag{6.3}$$

The second law of thermodynamics establishes that any internal process occurring spontaneously always increases the entropy of the system; *i.e.*,

$$ds_i \geq 0 \tag{6.4}$$

where ds_i vanishes at equilibrium. Therefore, the total entropy change can only be negative when,

$$ds_e < 0 \qquad \text{and} \qquad \mid ds_e \mid > ds_i \tag{6.5}$$

Thus, it can be seen that giving a sufficient amount of negative entropy flow the system is able to maintain an ordered configuration.

The thermodynamic potential that measures work availability is given by the Helmholtz free energy ψ, which is defined as

$$d\psi = du - Tds - sdT \tag{6.6}$$

In the context of amorphous molecules, the energy associated with intermolecular interactions remains practically constant compared to the change in the configurational entropy. Likewise, it can be assumed that temperature remains unchanged during the entire deformation process. Accordingly, $du = 0$ and $dT = 0$. Then, *Equations* 6.1 and 6.6 adopt the following forms proportional to the entropy change (Rosen, 1993)

$$d\psi = -Tds \tag{6.7a}$$

$$dw = -Tds \tag{6.7b}$$

Therefore, after combining *Equations* 6.7a and 6.7b,

$$d\psi = dw \tag{6.8}$$

Entropy has a statistical definition given by the usual form of Boltzmann's principle, which says that entropy is proportional to the logarithm of the number of microstates[1] available to the molecules from an observed initial macrostate $\mathcal{B}_0$ to a final macrostate $\mathcal{B}_f$. Each microstate is equally likely; therefore,

$$s = k \ln \frac{\Theta_f}{\Theta_0} = k \ln \Theta \tag{6.9}$$

Here k is Boltzmann's constant ($k = 1.380662 \times 10^{-23} \mathrm{JK}^{-1}$). The thermodynamic probability Θ is closely connected to the corresponding function of distribution of molecular configurations. Thus, from *Equation* 6.9, it can be seen that any change leading to a larger number of molecular conformations corresponds to a larger increase of entropy, and consequently, of the number of choices for the arrangement of the total energy (Lambert, 2002). Boltzmann's constant k is introduced to make them mathematically identical.

6.2.1 Configurational entropy

The number of possible configurations Θ of a molecule is a key parameter for describing the mechanical behaviour of amorphous polymers. According to the molecular chain

[1] Microstates refers to the different arrangements of the molecular chains.

network theory, deformation is associated with a reduction of entropy in the system. A common way to describe this phenomenon is to relate entropy to disorder. A strained amorphous material has low entropy because its molecules are enforced to align along certain directions in space. As constraints are removed and molecules are released, disorder increases and entropy rises. Since entropy is an extensive property[2], the total entropy in a system is obtained by simply summing the entropy contributions of each individual chain.

An amorphous polymeric material can be considered as a three-dimensional network of long flexible chains, randomly oriented and interconnected together by chemical cross-links at the so-called junction-points. Using the affine deformation assumption[3], the junction-points are looked upon as discrete points of a continuum model. Junction point fluctuations are negligible when compared to rigid-link ones.

An idealized lineal molecule can be thought of as an assembly of N carbon-carbon backbone bonds of length ℓ connected by freely rotating pivots, as illustrated in *Figure* 6.2. Let $\ell_i^{(j)} (j = 1, \ldots, N)$ be a set of N vectors representing the individual segments of a molecule. As shown in *Figure* 6.3, the vector directions are assumed pointing from bond $C^{(j-1)}$ to bond $C^{(j)}$, and the angle between two successive vectors is given as $\theta^{(j,j-1)}$. The chain size is evaluated based on the end-to-end distance, which is simply the vector length connecting the first and last segments of the chain, as shown in *Figure* 6.2. This end-to-end distance ranges between a minimum and a maximum value. The minimum distance happens when a molecule's ends are just touching and corresponds to the atomic spacing (van der Waals radii) between the chain-end atoms. On the other hand, the maximum value occurs when a molecule is fully extended, and all bonds lie in a straight line; *i.e.*, $r_{\max} = N\ell$.

In the Euclidean space, the end-to-end vector r_i for a particular molecule is given by the vector sum over the bond segments; such as

$$r_i = \ell_i^{(1)} + \ell_i^{(2)} + \ldots + \ell_i^{(N)} \tag{6.10}$$

It is reasonable to assume that for very large molecules, the vectorial segments follow a random uniform distribution function, *i.e.*, all vectors are of equal probability; therefore,

[2] An extensive property varies directly with the amount of matter present.
[3] These models are referred to as affine because the entangled points are assumed to be fixed during deformation and the average number of segments between entanglement points remains constant.

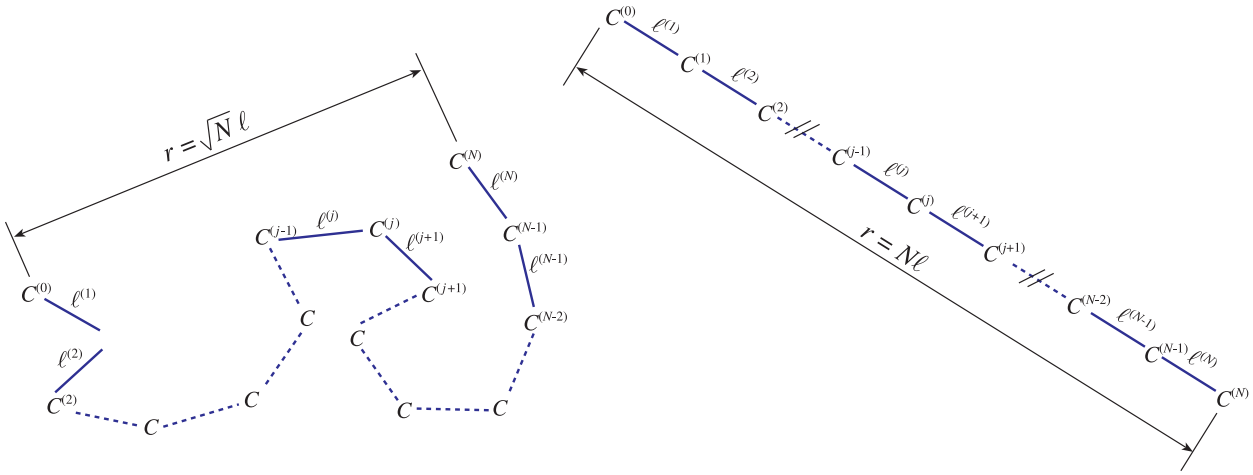

Figure 6.2: (left) Schematic representation of a polymer chain, and (right) end-to-end distance of a fully extended molecule.

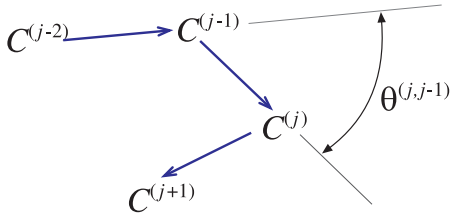

Figure 6.3: Vector directions and angles in a polymer chain.

$$\ell_i^{(1)} + \ell_i^{(2)} + \ldots + \ell_i^{(N)} = \langle \ell_i \rangle \cong 0_i \tag{6.11}$$

Nevertheless, the chain length can be estimated from the magnitude squared of the vector r_i (*e.g.*, Eyring, 1932; Shaw and MacKnight, 2005); that is,

$$r^2 = r_i r_i = \sum_j \ell_i^{(j)} \ell_i^{(j)} + 2 \sum_k \sum_{k<p} \ell_i^{(k)} \ell_i^{(p)} \tag{6.12}$$

It follows immediately that $\ell_i^{(j)} \ell_i^{(j)}$ is the square of segment $\ell_i^{(j)}$ length since both vectors point towards the same direction, and consequently, the cosine of the angle is equal to unity; therefore,

$$\sum_j \ell_i^{(j)} \ell_i^{(j)} = \ell^2 \sum_j \theta^{(j,j)} = N\ell^2 \tag{6.13}$$

On the other hand, the second term of *Equation* 6.12 can be written as

$$\ell_i^{(j)} \ell_i^{(k)} = \ell^2 \cos\theta^{(j,k)} \tag{6.14}$$

where if $\theta^{(j,k)}$ follows a random uniform distribution, it cancels out; *i.e.*,

$$\sum_k \sum_{k<p} \ell_i^{(k)} \ell_i^{(p)} = \ell^2 \sum_k \sum_{k<p} \cos\theta^{(kp)} = \ell^2 \langle \cos\theta^{(kp)} \rangle \cong 0 \tag{6.15}$$

Thus, the mean end-to-end distance obtained from an ensemble of statistical segments forming an equivalent-freely-jointed chain is given as (Treloar, 1975)

$$r = \sqrt{N}\ell \tag{6.16}$$

Gaussian and non-Gaussian models are used to determine the number of configurations of a single chain, defined by N and ℓ (Wang and Guth, 1952). The Gaussian model given in the following equation is relatively simple, but is only valid for small deformations.

$$\Theta = \Theta_0 \exp\left[-\frac{3}{2} N \left(\frac{r}{\ell}\right)^2\right] \tag{6.17}$$

A better prediction for the large strain range is achieved using non-Gaussian chain models (Flory, 1988). In 1952, Kuhn and Grün used non-Gaussian statistics theory to obtain the probability density in the logarithmic form of a molecular chain composed by N monomer segments of length ℓ (Treloar, 1975) as

$$\Theta = \Theta_0 \exp\left[-N\left(\frac{r}{N\ell}\beta - \ln\frac{\beta}{\sinh\beta}\right)\right] \tag{6.18}$$

where $\beta = \mathcal{L}^{-1}(r/N\ell)$ is the inverse Langevin function[4] with $r/N\ell$ as the fractional extension (Treloar, 1954).

Here, adopting the non-Gaussian model, the entropy of an idealized single chain can be written as

$$s = k\ln\Theta = s_0 - kN\left(\frac{r}{N\ell}\beta + \ln\frac{\beta}{\sinh\beta}\right) \tag{6.19}$$

where $s_0 = -k\ln\Theta_0$ is the entropy value in the unperturbed state.

6.3 Back-stress tensor

When an amorphous polymeric material experiences a stress state that breaks the bonds holding molecules together, its resistance to deformation increases. Initially, molecules are randomly entangled; thus, the molecular network can be statistically assumed to be isotropic. After yielding, short-range molecular motion takes place to accommodate the imposed deformation, and chains stretch and align smoothly along a preferred direction. As molecules stretch, a reduction of the configuration entropy, and consequently, an increase of the internal strength for further deformation occur (Haward and Thackray, 1968). These phenomena can be expressed as kinematic hardening and represented as a translation of the yield surface F with respect to the origin of the stress space; where a back-stress tensor H_{ij} indicates the current position of the surface, as shown in *Figure* 6.4. The yield function governing the evolution of inelastic deformations can be expressed as

$$F = J_2(\sigma_{ij} - H_{ij}) - \sigma_0 \leq 0 \tag{6.20}$$

where J_2 represents a distance in the stress space dependent on the Cauchy stress and back-stress tensors, and σ_0 is a reference strength.

To model how the amorphous material hardens, it is necessary to find a thermodynamic-based formulation valid for large inelastic deformations and a simple molecular description of the material by using some molecular chain network theory (*e.g.*, Tomita

[4] The Langevin function is defined as $\mathcal{L}(x) = \cosh(x) - 1/x$, and according to Cohen (1991), its inverse is accurately approximated as $\mathcal{L}^{-1}(z) \approx z(3 - z^2)/(1 - z^2)$.

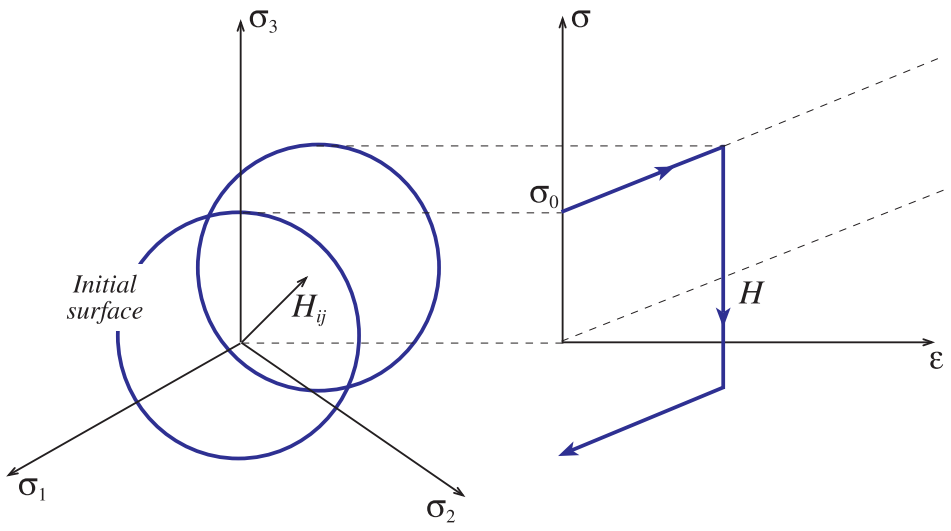

Figure 6.4: Back-stress tensor: representation in stress space and in tension-compression. The scales coincide on the principal axes (Lemaitre and Chaboche, 1994).

et al., 1997; Tomita, 2000). To represent the relation between hardening and microstructure development, the back-stress tensor can be associated to the change of free energy by the so-called Clausius-Duhem inequality, obtained from the second law of thermodynamics as follows,

$$H_{ij}L_{kj} - \dot{\psi} \geq 0 \tag{6.21}$$

where the equality and inequality hold for reversible and irreversible processes, respectively.

To calculate the back-stress tensor, it is assumed that the Helmholtz free energy ψ can be expressed in terms of the left Cauchy-Green tensor B_{ij} as a measure of deformation; thus,

$$\psi = \psi(B_{ij}) \tag{6.22}$$

where B_{ij} is given in terms of the deformation gradient tensor F_{ij} as

$$B_{ij} = F_{ik}F_{jk} \tag{6.23}$$

Taking the time derivative of *Equation* 6.22, yields

$$\dot{\psi} = \frac{\partial \psi}{\partial B_{ij}}\dot{B}_{ij} \tag{6.24}$$

The evolution equation of B_{ij} gives that

$$\dot{B}_{ij} = \dot{F}_{ik}F_{jk} + F_{ik}\dot{F}_{jk} = L_{ik}B_{kj} + B_{ik}L_{jk} \tag{6.25}$$

where L_{ij} is the velocity gradient. Thus, if $D_{ij} = \frac{1}{2}(L_{ij} + L_{ji})$

$$\dot{B}_{ij} = B_{ik}(L_{kj} + L_{jk}) = 2B_{ik}D_{kj} \tag{6.26}$$

Because the velocity gradient can be expressed in terms of its symmetric and skew-symmetric components, the first term of *Equation* 6.21 can be simplified as

$$H_{ij}L_{ij} = H_{ij}(D_{ij} + W_{ij}) = H_{ij}D_{ij} \tag{6.27}$$

Using *Equation* 6.24 and the results from *Equations* 6.26 and 6.27, the Clausius-Duhem inequality for a reversible process can be written as

$$H_{ij}D_{ij} - 2\frac{\partial\psi}{\partial B_{ij}}B_{ik}D_{kj} = \left(H_{ij} - 2\frac{\partial\psi}{\partial B_{kj}}B_{ki}\right)D_{ij} = 0 \tag{6.28}$$

from which, the equation of state of the back-stress tensor can be obtained as

$$H_{ij} = 2B_{ik}\frac{\partial\psi}{\partial B_{kj}} \tag{6.29}$$

If the Helmholtz free energy is given as in *Equation* 6.7a, the back-stress tensor can be expressed in terms of the end-to-end distance, left Cauchy-Green tensor, and entropy as

$$H_{ij} = -2T\frac{ds}{dr}B_{ik}\frac{\partial r}{\partial B_{kj}} \tag{6.30}$$

6.3.1 The eight-chain model

To capture the most important mechanical features of the amorphous material, the random chain network is modelled as an assembly of idealized unit cells. Developed by Arruda and Boyce (1993), one of the most widely used models is the eight-chain model. In this model, it is assumed that each unit cell is an isotropic cube comprising eight chains, which are linked at the cube centre and extended individually to each one of the corners. *Figure* 6.5 illustrates the problem geometry in the undeformed and deformed states, stretched in the principal strain frame.

The unstretched network includes chains of length $r_0 = \sqrt{N}\ell$ inside a cube of initial dimension a_0. From this geometry

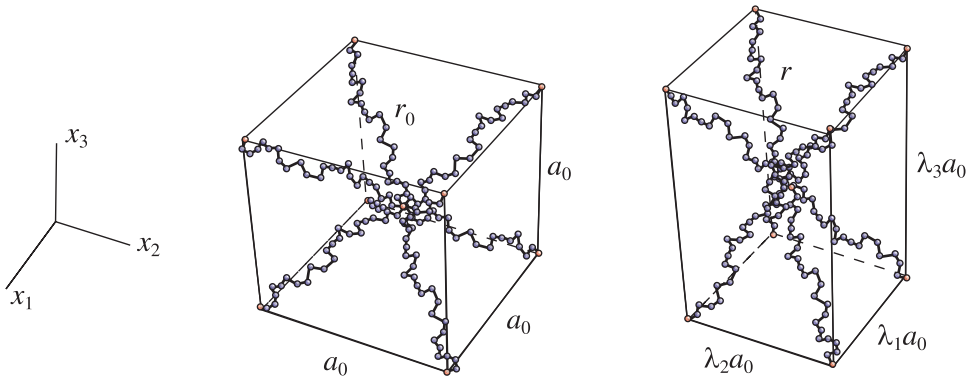

Figure 6.5: The eight chain network model in (left) the unstretched and (right) stretched configurations.

$$a_0 = \frac{2}{3}\sqrt{3}r_0 = 2\sqrt{\frac{N}{3}}\ell \tag{6.31}$$

When the cube is stretched, its edges measure $\lambda_1 a_0$, $\lambda_2 a_0$, and $\lambda_1 a_0$ in the x_1, x_2, and x_3 directions, respectively. A chain vector from the centre of the cube to a corner has a length

$$r = \frac{a_0}{2}(\lambda_1^2 + \lambda_2^2 + \lambda_3^2)^{1/2} = \frac{a_0}{2}\sqrt{I_I} \tag{6.32}$$

where $I_I = \lambda_1^2 + \lambda_2^2 + \lambda_3^2 = B_{ii}^2$ is the left Cauchy-Green stretch tensor first invariant.

Substituting the unstretched length and *Equation* 6.31 into 6.32 gives the chain length in terms of the number of links, the chain bond length, and the stretch first invariant

$$r = \sqrt{\frac{N}{3}I_I}\ell \tag{6.33}$$

The eight-chain model is symmetric with respect to the three principal axes; therefore, the chains are stretched at the same extension ratio,

$$\lambda = \frac{r}{r_0} = \sqrt{\frac{I_I}{3}} \tag{6.34}$$

The back stress tensor H_{ij} is derived from *Equation* 6.30 by calculating the first partial derivative of the end-to-end distance with respect to the left Cauchy-Green stretch tensor as

$$\frac{\partial r}{\partial B_{ij}} = \frac{\partial r}{\partial \lambda}\frac{\partial \lambda}{\partial I_I}\frac{\partial I_I}{\partial B_{ij}} \tag{6.35}$$

where

$$\begin{aligned}\frac{\partial r}{\partial \lambda} &= r_0 = \sqrt{N}\ell \\ \frac{\partial \lambda}{\partial I_I} &= \frac{1}{6\lambda} \\ \frac{\partial I_I}{\partial B_{ij}} &= I_{ij}\end{aligned}$$

Then, if

$$\frac{ds}{dr} = -k\frac{\beta}{\ell} \tag{6.36}$$

and assuming that the random system exhibits a thermodynamical entropy corresponding to a chain entropy ensemble; *i.e.*, $s_{\text{syst}} = \sum s = ns$, the back-stress tensor for the network is expressed as

$$H_{ij} = -2nT\frac{ds}{dr}B_{ik}\frac{\partial r}{\partial B_{kj}} = \frac{nkT}{3}\sqrt{\frac{3N}{I_I}}\mathcal{L}^{-1}\left(\sqrt{\frac{I_I}{3N}}\right)B_{ij} \tag{6.37}$$

where n is the number of chains per unit volume (Arruda et al., 1995).

By definition, the deviatoric back-stress tensor is

$$H'_{ij} = H_{ij} - \tfrac{1}{3}H_{kk}I_{ij} \tag{6.38}$$

Therefore,

$$H'_{ij} = \frac{C_R}{3}\sqrt{\frac{3N}{I_I}}\mathcal{L}^{-1}\left(\sqrt{\frac{I_I}{3N}}\right)(B_{ij} - \tfrac{1}{3}I_I I_{ij}) \tag{6.39}$$

Equation 6.39 provides the back-stress tensor of the network subjected to a deformation represented by B_{ij}, where $C_R = nkT$ is the rubbery shear modulus[5].

[5]The rubbery shear modulus is related to the number average molecular weight M_N through the expression $C_R = \rho RT/M_N$, where ρ and R are the density of the amorphous phase and gas constant, respectively (Treloar, 1975).

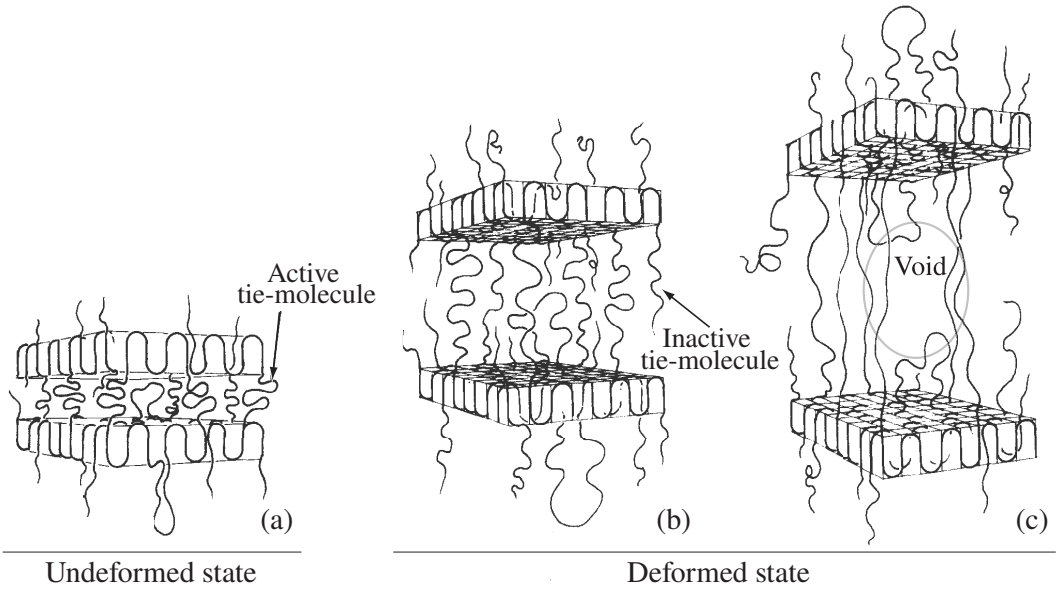

Figure 6.6: Idealized deformation mechanisms in amorphous polyethylene (adapted from Lustiger and Markham, 1983).

6.4 Proposed damage model

Using Continuum Damage Mechanics, an isotropic damage variable can provide a rational representation of the degradation progress taking place in the amorphous microstructure. Damage in amorphous polyethylene can be seen as the appearance of material discontinuities which decrease the effective areas that transmit internal forces. Tie-molecules play an important role in connecting neighbouring crystallites and in transmitting internal loads (*e.g.*, Takayanagi et al., 2003; Nitta and Takayanagi, 2003). However, large deformations can lower the cohesive forces that maintain tie-molecules attached to the crystalline material. Once a tie-molecule becomes inactive, it binds the lamellar material and does not participate directly in the stress transmittance to rise hardening (Takayanagi et al., 2003). This mechanism raises stresses in the still active tie-molecules, facilitating the further disentanglement and pull-out of the network anchors and contributing significantly to the degradation of the mechanical behaviour of the material.

6.4.1 Formulation

Based on the concept of the so-called damage variable, the number density[6] of active and inactive tie-molecules can be used to estimate the evolution of the fraction of discontinuities in the amorphous material. To illustrate the damage process in amorphous polyethylene, consider the inclusion comprising amorphous and crystalline materials shown in *Figure* 6.6a. When the inclusion deforms by interlamellar separation, the partially stretched chain segments within the amorphous phase start to align parallel to the loading direction, as given in *Figure* 6.6b. Once the chain segments reach their full extended lengths, they lead to lamella fragmentation (*not shown*), cavitation, and detachment of crystalline-amorphous interface, as illustrated in *Figure* 6.6c (*e.g.*, Kazmierczak et al., 2005; Argon et al., 2005).

In the reference configuration, the initial number density of tie-molecules is defined as Λ. In the deformed configuration at some time t, the number density of inactive tie-molecules (molecules unable to carry load) is expressed as Λ_I. Then, the isotropic damage variable representing the density of discontinuities in the material can be written as

$$\Omega = \frac{\text{Inactive tie-molecule number density}}{\text{Initial tie-molecule number density}} = \frac{\Lambda_I}{\Lambda} \tag{6.40}$$

Furthermore, if $\tilde{\Lambda}$ represents the remaining number density of tie-molecules at time t; *i.e.*, $\tilde{\Lambda} = \Lambda - \Lambda_I$, the damage variable can be rewritten as

$$\Omega = 1 - \frac{\tilde{\Lambda}}{\Lambda} \tag{6.41}$$

This damage measure takes magnitudes in the range from zero to unity; zero in the case of no damage and unity for a completely damaged material.

Using the concept of effective stress and the proposed isotropic damage parameter, a mapping between the deviatoric Cauchy stress S_{ij} and the effective stress $\tilde{S}_{ij}$ is introduced as

$$\tilde{S}_{ij} = \frac{S_{ij}}{1 - \Omega} \tag{6.42}$$

[6]The number density refers to the amount of molecules per volume

6.4.2 Damage-coupled flow rule

To describe the yield condition, a shifted stress deviator S_{ij}^H (Xuejun et al., 2001) is introduced as

$$S_{ij}^H = \tilde{S}_{ij} - H'_{ij} \tag{6.43}$$

where $\tilde{S}_{ij}$ is the effective stress tensor as defined in *Equation* 6.42, and H'_{ij} is the deviatoric back-stress tensor describing the anisotropic resistance to plastic deformation (kinematic hardening), respectively.

The plastic deformation rate is given by the normality law (Lemaitre and Chaboche, 1994)

$$D_{ij} = \dot{\alpha} \frac{\partial F}{\partial \sigma_{ij}} \tag{6.44}$$

where $\dot{\alpha}$ is an arbitrary and a positive proportionality factor called the plastic multiplier, and F is the yield function, given in terms of an equivalent stress σ_{eq} and a reference strength σ_0 as

$$F = F(\sigma_{eq}, \sigma_0) = 0 \tag{6.45}$$

If the yield surface is based on the von Mises criterion, *i.e.*,

$$F = \sigma_{eq} - \sigma_0 \tag{6.46}$$

the equivalent stress σ_{eq} can be defined as (Lemaitre, 1996)

$$\sigma_{eq} = J_2(S_{ij}^H) = \left(\tfrac{3}{2} S_{ij}^H S_{ij}^H\right)^{\frac{1}{2}} = \left[\frac{3}{2}\left(\frac{S_{ij}}{1-\Omega} - H'_{ij}\right)\left(\frac{S_{ij}}{1-\Omega} - H'_{ij}\right)\right]^{\frac{1}{2}} \tag{6.47}$$

Therefore, the evolution of the yield surface can be written as

$$\frac{\partial F}{\partial S_{ij}} = \frac{3}{2(1-\Omega)} \frac{\frac{S_{ij}}{1-\Omega} - H'_{ij}}{\sigma_{eq}} \tag{6.48}$$

Likewise, it is postulated that the accumulated plastic strain rate

$$\dot{p} = \sqrt{\tfrac{2}{3} D_{ij} D_{ij}} \tag{6.49}$$

is related to the plastic multiplier as (Lemaitre, 1996)

$$\dot{p} = \frac{\dot{\alpha}}{1-\Omega} \tag{6.50}$$

Using a power-law relationship, the accumulated plastic strain rate can be written as a function of the equivalent stress as

$$\dot{p} = \dot{\epsilon_0} \left(\frac{\sigma_{eq}}{\sigma_0} \right)^n \tag{6.51}$$

where $\dot{\epsilon_0}$ is a reference strain rate, σ_0 is the amorphous material strength, and n is the rate exponent.

Substituting *Equations* 6.48, 6.50, and 6.51 into 6.44, the constitutive equation for the inelastic deformations in the amorphous material is given as

$$D_{ij} = \tfrac{3}{2}\dot{\epsilon_0} \left(\frac{\sigma_{eq}}{\sigma_0} \right)^{n-1} \frac{\frac{S_{ij}}{1-\Omega} - H'_{ij}}{\sigma_0} \tag{6.52}$$

6.4.3 Damage evolution law

A thermodynamics-based evolution law for damage is introduced to account for the material damage accumulation. The force f required to stretch a single molecule from its characteristic end-to-end length r to a deformed length $r + dr$ is given in terms of the amount of work w done (strain energy) as

$$f = \frac{dw}{dr} \tag{6.53}$$

According to *Equation* 6.7a, the work done equals the increase in free energy of the molecule; thus, the force can be given in terms of entropy as

$$f = \frac{d\psi}{dr} = -T\frac{ds}{dr} \tag{6.54}$$

Therefore, postulating a relationship between the strain energy and the internal loads required to overcome the molecular cohesion, damage can be described in terms of an energy function, so the material is modelled as a continuum. Thus, using the eight-chain model derived by Boyce and Arruda (2000), the required function can be expressed as

$$W = wn_{chains} = C_R N \left[\beta \sqrt{\frac{I_I}{3N}} + \ln \frac{\beta}{\sinh \beta} \right] \tag{6.55}$$

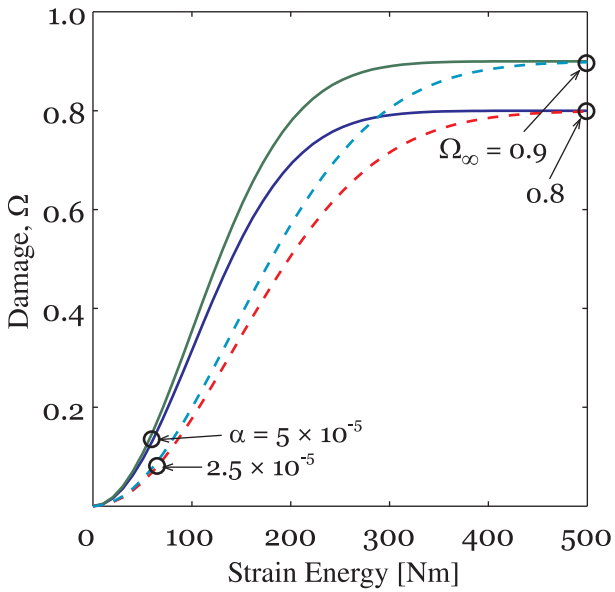

Figure 6.7: Amorphous phase damage evolution for two different values of Ω_∞ and α.

with n_{chains} being the number of chains per unit volume.

The proposed evolution law for damage follows the formulation used by Fotiu et al. (1990), which is of the form

$$\Omega = \Omega_\infty[1 - \exp(-\alpha W^2)] \tag{6.56}$$

where Ω_∞ and α are material parameters describing the asymptotic value of damage and how fast damage evolves, respectively. *Figure* 6.7 illustrates graphically the proposed relationship between Ω and W for two sets of material parameters.

6.5 Semicrystalline model

Polyethylene is a material with a complex microstructure in which neither amorphous nor crystalline phase exists in the pure state. To model the mechanical behaviour, the semicrystalline material morphology is simplified as a collection of inclusions comprising the two phases by their characteristic average volume fractions. In the spatial arrangement, each inclusion consists of crystalline material lying in a thin lamella attached to an amorphous layer, as illustrated in *Figure* 6.8. The interface region interconnecting

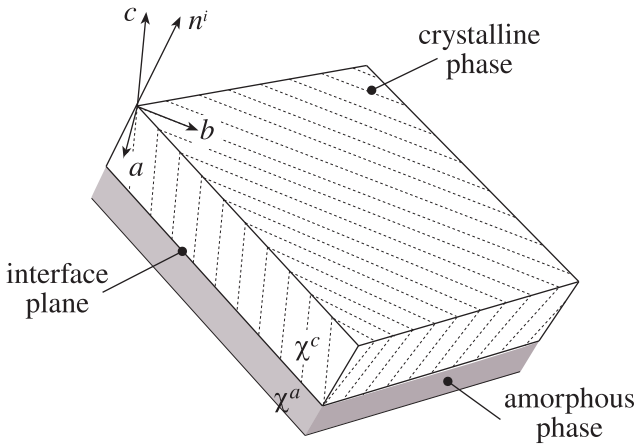

Figure 6.8: Schematic illustration of a two-phase composite inclusion

the two phases is the plane through which loads are carried and transferred by tie molecules. As shown in *Figure* 6.8, each composite inclusion is characterized by its crystalline-amorphous interface normal n_i, the crystalline lattice orientation; a_i, b_i, and c_i, and the crystalline and amorphous volume fractions; χ^c and χ^a ($\chi^a = 1 - \chi^c$). In the present formulation, it is assumed that the constitutive models containing complete information about the mechanical behaviour of each constituent are known (see *Sections* 4.3 and 6.4). After modelling the two materials independently, the inclusion behaviour is found by applying some compatibility and equilibrium restrictions along the interface plane. Then, by considering uniform stresses everywhere and suitable boundary conditions in the aggregate, the behaviour of the material on the large scale can be determined.

In summary, the constitutive equations used to describe the mechanical behaviour of the crystalline and amorphous phases of the material are:

Crystalline phase

1. Material law

$$D_{ij} = M_{ijkl} S^*_{lk} \tag{6.57}$$

where M_{ijkl} is the fourth-order compliance tensor given by

$$M_{ijkl} = \dot{\gamma}_0 \sum_\alpha \frac{1}{(1-\Omega^\alpha) g^\alpha} \left| \frac{S^*_{mn} R^\alpha_{nm}}{(1-\Omega^\alpha) g^\alpha} \right|^{n^c - 1} R^\alpha_{ij} R^\alpha_{kl} \tag{6.58}$$

2. Damage evolution law

$$\dot{\Omega}^{\alpha} = \dot{\Omega}_0 \left| \frac{\tau^{\alpha}}{(1-\Omega^{\alpha})g^{\alpha}} \right|^{m} \tag{6.59}$$

3. Spin

$$W_{ij} = W^{*}_{ij} + RW^{p}_{ij} \tag{6.60}$$

where

$$R = \tanh(\zeta\bar{\Omega}) \tag{6.61}$$

Amorphous phase

1. Material law

$$D_{ij} = \tfrac{3}{2}\dot{\epsilon}_0 \left(\frac{\sigma_{eq}}{\sigma_0}\right)^{n^a-1} \frac{\frac{S_{ij}}{1-\Omega} - H'_{ij}}{\sigma_0} \tag{6.62}$$

2. Hardening law

$$H'_{ij} = \frac{C_R}{3}\sqrt{\frac{3N}{I_I}}\mathcal{L}^{-1}\left(\sqrt{\frac{I_I}{3N}}\right)(B_{ij} - \tfrac{1}{3}I_I I_{ij}) \tag{6.63}$$

3. Damage evolution law

$$\Omega = \Omega_{\infty}[1 - \exp(-\alpha W^2)] \tag{6.64}$$

6.6 Inclusion volume-averaging

Let L^i_{ij}, L^c_{ij}, and L^a_{ij} be the velocity gradients for the inclusion and for the crystalline and amorphous phases, respectively. The velocity gradient of the inclusion can be expressed as (Lee et al., 1993b)

$$L^i_{ij} = \chi^c L^c_{ij} + (1-\chi^c)L^a_{ij} \tag{6.65}$$

If D^i_{ij} and W^i_{ij} are the symmetric and skew-symmetric components of the velocity gradient for the inclusion, the inclusion deformation rate can be written as (Lee et al., 1993a)

$$D^i_{ij} = \mathrm{sym}(L^i_{ij}) = \chi^c D^c_{ij} + (1-\chi^c)D^a_{ij} \tag{6.66}$$

and the inclusion spin as

$$W_{ij}^{i} = \text{skw}(L_{ij}^{i}) = \chi^{c} W_{ij}^{c} + (1 - \chi^{c}) W_{ij}^{a} \tag{6.67}$$

Similarly, the inclusion Cauchy stress is given as (van Dommelen et al., 2003b)

$$\sigma_{ij}^{i} = \chi^{c} \sigma_{ij}^{c} + (1 - \chi^{c}) \sigma_{ij}^{a} \tag{6.68}$$

where the deviatoric part can be defined as (Lee et al., 1993a,b)

$$S_{ij}^{i} = \chi^{c} S_{ij}^{c} + (1 - \chi^{c}) S_{ij}^{a} \tag{6.69}$$

6.6.1 Interface conditions

On the interface between the amorphous and crystalline layers, kinematical coupling is maintained by imposing compatibility on the velocity gradients. Assuming no slippage at the crystalline-amorphous interface, the first interface compatibility condition can be written as

$$L_{ij}^{i} t_i = L_{ij}^{a} t_i = L_{ij}^{c} t_i \tag{6.70}$$

where t_i is an arbitrary vector on the interface plane, such that $t_i n_i = 0$. Consequently, from *Equations* 6.65 and 6.70, the continuity conditions expressed in components relative to the local coordinate system can be written as

$$L_{\alpha\beta}^{i} = L_{\alpha\beta}^{a} = L_{\alpha\beta}^{c} \tag{6.71a}$$

$$L_{3\beta}^{i} = L_{3\beta}^{a} = L_{3\beta}^{c} \tag{6.71b}$$

where the subscripts α and β range from 1 to 2 (In-plane components). Then, from *Equation* 6.71a,

$$D_{\alpha\beta}^{i} = D_{\alpha\beta}^{a} = D_{\alpha\beta}^{c} \tag{6.72a}$$

$$W_{12}^{i} = W_{12}^{a} = W_{12}^{c} \tag{6.72b}$$

and assuming incompressibility in both phases; *i.e.*, $D_{ii}^{a} = 0$ and $D_{ii}^{c} = 0$,

$$D_{33}^{i} = D_{33}^{a} = D_{33}^{c} \tag{6.73}$$

The possible discontinuous kinematic components are related by the inclusion-averaged relations

$$L^i_{\alpha 3} = \chi^c L^c_{\alpha 3} + (1 - \chi^c) L^a_{\alpha 3} \tag{6.74}$$

where the deformation rate components are given as

$$D^i_{\alpha 3} = D^i_{3\alpha} = \chi^c D^c_{3\alpha} + (1 - \chi^c) D^a_{3\alpha} \tag{6.75}$$

and the spin rate components as

$$-W^i_{\alpha 3} = W^i_{3\alpha} = \chi^c W^c_{3\alpha} + (1 - \chi^c) W^a_{3\alpha} \tag{6.76}$$

From *Equation* 6.71b, it is obtained that

$$\Delta D_{3\alpha} = D^a_{3\alpha} - D^c_{3\alpha} = W^a_{3\alpha} - W^c_{3\alpha} \tag{6.77}$$

Thus, substituting *Equation* 6.77 into 6.76 and after some algebra, the remainder of the conditions are written as

$$W^c_{3\alpha} = W^i_{3\alpha} - (1 - \chi^c) \Delta D_{3\alpha} \tag{6.78a}$$

$$W^a_{3\alpha} = W^i_{3\alpha} + \chi^c \Delta D_{3\alpha} \tag{6.78b}$$

The second interface compatibility condition enforces traction equilibrium across the interface, which is written as

$$\sigma^i_{ij} n_i = \sigma^a_{ij} n_i = \sigma^c_{ij} n_i \tag{6.79}$$

As a result,

$$\sigma^i_{3j} = \sigma^a_{3j} = \sigma^c_{3j} \tag{6.80}$$

with j ranging from 1 to 3. From *Equation* 6.80, the requirement of shear stress across the interface can be expressed as

$$S^i_{3\alpha} = S^a_{3\alpha} = S^c_{3\alpha} \tag{6.81}$$

and the restraint of normal stress as

$$S^a_{33} + p^a = S^c_{33} + p^c \tag{6.82}$$

where p^a and p^c represent pressure in the amorphous and crystalline phases, respectively.

6.6.2 Inclusion interaction law

Following Lee and coworkers (1993b), a material point is considered an aggregate of composite inclusions subject to boundary conditions consistent with macroscopically homogeneous fields. To relate the volume-averaged behaviour of each inclusion to the imposed boundary conditions, a local-global interaction law is formulated. The macroscopic deviatoric Cauchy stress, macroscopic deformation rate, and macroscopic spin are represented as $\bar{S}_{ij}$, $\bar{D}_{ij}$, and $\bar{W}_{ij}$, respectively.

The Sachs model states that the macroscopic stress is equal to the stress in each inclusion; hence, the inclusion deviatoric stress is approximated as

$$S^i_{ij} = \bar{S}_{ij} \tag{6.83}$$

Similarly, the inclusion spin is equalled to the macroscopic spin; consequently,

$$W^i_{ij} = \bar{W}_{ij} \tag{6.84}$$

To complete the interaction law, the macroscopic deformation rate is assumed equal to the volume average deformation rate; therefore,

$$\bar{D}_{ij} = \langle D^i_{ij} \rangle = \textstyle\sum_i \chi^i D^i_{ij} \tag{6.85}$$

where $\langle \bullet \rangle$ denotes the volume average over the total number of inclusions N^i, and χ^i represents the volume fraction of the i^{th} inclusion.

The proposed model satisfies global equilibrium and compatibility trivially, because $S^i_{ij} = \bar{S}_{ij}$ and $W^i_{ij} = \bar{W}_{ij}$, but local compatibility is not addressed. However, comparisons done by Lee et al. (1993b) between the Sachs model and other hybrid models suggest that the Sachs model responses do not differ significantly from those obtained with other models.

6.7 Numerical results and discussion

The goal of this section is to describe the overall mechanical behaviour of a semicrystalline polyethylene material under uniaxial tension and simple shear. A distribution of 100 inclusions of equal volume fractions (χ^i=1.0) is considered in this analysis. The orientation of each inclusion is numerically generated in a random manner by using Euler

angles (See details in *Chapter* 7). All the inclusions are assumed to have the same material properties, which are summarized in *Table* 6.1 for uniaxial tension and in *Table* 6.3 for simple shear. For the given loading conditions, two different approaches are analyzed. The first approach, identified as *Model A*, assumes damage occurs only in the crystalline phase; *i.e.*, degradation of the amorphous phase is ignored. The second approach, *Model B*, considers the effect of damage on the mechanical behaviour of both phases. A comparison between Lee et al.'s (1993a) and *Model B* is shown in *Appendix* B. The slip systems of the crystalline phase have shear strengths whose values are taken from Lee et al. (1993a,b), for a reference resolved shear strength of 8.0 MPa, and presented in *Table* 6.2. The model parameters are identified to describe as close as possible the experimental results reported by G'Sell and Jonas (1981) for a sample of high density polyethylene tested at 21°C under uniaxial tension and by G'Sell et al. (1983) for a simple shear case tested at 23°C.

Table 6.1: Material parameters for the simulations under uniaxial tension.

Parameter	**Model A**	**Model B**	**Lee et al.'s model**
Crystalline phase			
Strain rate sensitivity, n^c	5.0	5.0	9.0
Reference strain rate, $\dot{\gamma}_0$ [s^{-1}]	0.001	0.001	0.001
Damage rate sensitivity, m	2.0	2.0	NA
Reference damage rate, $\dot{\Omega}_0$ [MPa^{-1}]	0.0003	0.00025	NA
Spin release, ζ	6.0	8.0	NA
Crystallinity, χ^c	70	70	70
Amorphous phase			
Strain rate sensitivity, n^a	5.0	5.0	9.0
Reference strain rate, $\dot{\gamma}_0$ or $\dot{\epsilon}_0$ [s^{-1}]	0.001	0.001	0.001
Strength τ_0 or σ_0, [MPa]	6.4	6.4	8.0
Number of rigid links, N	50	50	49
Rubbery shear modulus, C_R	5.0	4.0	1.6
Critical damage, Ω_∞	NA	0.8	NA
Damage rate, α	NA	0.000005	NA

Table 6.2: Resolved shear strengths.

Slip system	$\mathbf{g^{\alpha}}$**[MPa]**
(100)[001]	8.0
(010)[001]	20.0
$\{110\}\langle 001\rangle$	20.0
(100)[010]	13.3
(010)[100]	20.0
$\{110\}\langle 1\bar{1}0\rangle$	19.5

6.7.1 Uniaxial tension case

The aim of the first example is to demonstrate the capability of the model to describe the stress-strain behaviour and texture evolution of a semicrystalline polyethylene material. The numerical test is carried out under constant velocity gradient,

$$\bar{L}_{ij} = \dot{\gamma} \begin{bmatrix} -0.5 & 0.0 & 0.0 \\ 0.0 & 1.0 & 0.0 \\ 0.0 & 0.0 & -0.5 \end{bmatrix}$$

where $\dot{\gamma}$ is a macroscopic strain rate equal to 0.001 s^{-1}.

The influence of damage on the overall mechanical behaviour is analyzed. As a first approach, damage only on the crystallographic slip systems is considered in the formulation (*Model A*). Therefore, the constitutive equations for the amorphous phase are based on the original phenomenological model proposed by Lee et al. (1993a,b). The damage-coupled model for the crystalline phase is described by *Equations* 6.57 to 6.61. On the other hand, *Model B* is used to describe damage in both crystalline and amorphous phases. *Figures* 6.9 to 6.19 show the responses obtained with these two approaches.

The simulation results are compared with two viscoplastic models (Lee et al., 1993b; Nikolov et al., 2006) and experimental data (G'Sell and Jonas, 1981), as illustrated in *Figures* 6.9 and 6.10. It is seen that the predictions are in agreement with the experimental data and that the proposed models are able not only to describe larger strains than the models proposed by Lee et al. (1993a) and Nikolov et al. (2006), but also to represent the complete range of deformations. When comparing *Figures* 6.9 and 6.10, both models give similar stress-strain response; however, the second model (*Model B*) predicts slightly lower stress values at the early states of deformation (below 0.25).

Figures 6.11 and 6.12 show the predicted deformation rate ratio $\hat{D}^a/\hat{D}^c$ versus equivalent strain for *Model A* and *Model B*, respectively. The discrete points represent the results from Lee et al.'s (1993a; 1993b) models. As seen, for deformations below 0.5, both proposed models determine that the amorphous phase deforms more rapidly than the crystalline one; nevertheless, *Model B* predicts approximately a 10 times larger initial ratio than *Model A*. For deformations above 0.5, the ratios exhibit values relatively close to unity, while Lee et al.'s models estimate ratio values between 1.5 and 2.9, and 2.9 and 1.1, respectively. Likewise, *Figures* 6.13 and 6.14 show a stress comparison between the numerical results of the proposed and the previous models. It can be seen that, as in Lee et al.'s formulation, the stress ratio $\hat{\sigma}^a/\hat{\sigma}^c$ increases as deformation progresses; however, the most noteworthy feature in the proposed models is that the ratio evolves much faster. This peculiarity can be attributed to the fact that damage lowers the load-carrying capacity of the crystallographic slip systems as deformation increases.

The evolution of the maximum damage in the eight slip system is shown in *Figures* 6.15 and 6.16. It is found that damage progresses more rapidly when no damage of the amorphous phase is postulated. For both models, the larger damage values are displayed in the (010)[001], (110)[001], and (1$\bar{1}$0)[001] planes, all of them corresponding to chain slip systems. The lower damage value is observed in the (100)[001] systems. *Figure* 6.17 shows the evolution of the maximum damage in the amorphous phase, obtained from the second approach model. As can be seen, at the beginning, damage evolves moderately with deformation; then, it rises sharply once deformation of the amorphous phase is limited due to the molecule reorientation.

The pole figures of the (100) and (001) planes as well as the morphological textures corresponding to a selection of total deformations are represented in *Figures* 6.18 and 6.19. The projections (001) and (100) are shown perpendicular to the loading direction; transverse directions are referred as RD. The numerical crystallographic textures (*Figures* 6.18 and 6.19) are in good agreement with the measured pole figures from a sample subjected to a tensile strain of 2.1 and allowed to undergo natural relaxation for 24 hours to a final strain of 1.8, as reported by Li et al. (2001) in *Figure* 6.20. It is seen that as deformation progresses, a texture develops and the crystalline material becomes preferentially oriented relative to the tensile axis. In this case, morphological (interface) planes approach progressively the radial (transverse) directions. *Figures* 6.21 and 6.22 show the textures obtained numerically by Lee et al. (1993a) and Nikolov et al. (2006), respectively, for comparative purposes.

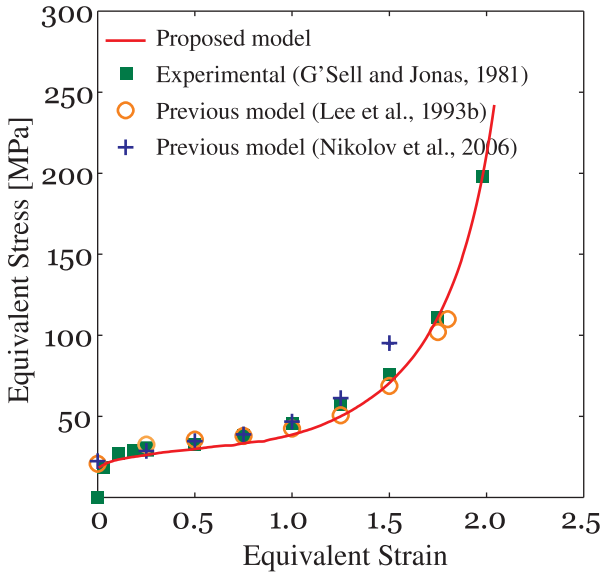

Figure 6.9: Equivalent stress versus equivalent strain behaviour of semicrystalline polyethylene under uniaxial tension for Model A (non-degradable amorphous phase model).

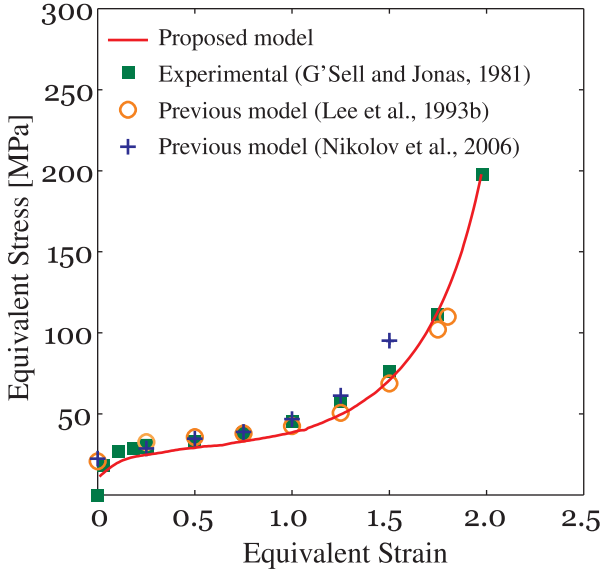

Figure 6.10: Equivalent stress versus equivalent strain behaviour of semicrystalline polyethylene under uniaxial tension for Model B (both phases degradable model).

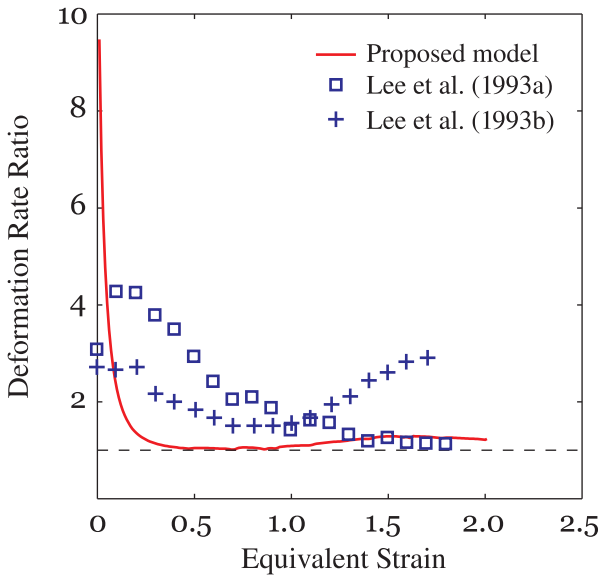

Figure 6.11: Deformation rate ratio versus equivalent strain for Model A (non-degradable amorphous phase model).

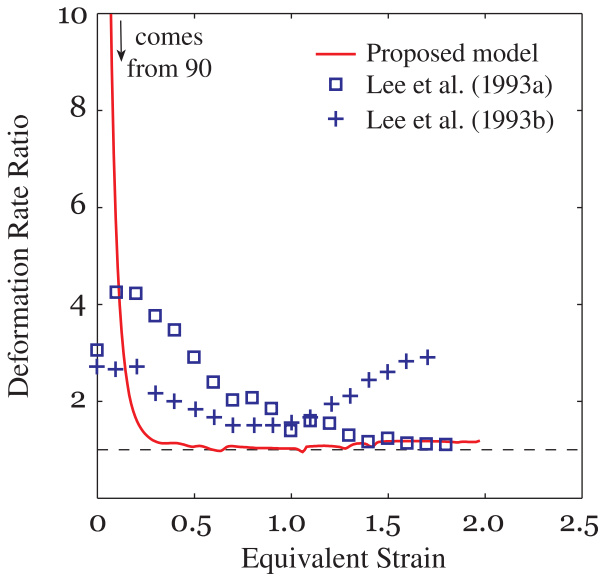

Figure 6.12: Deformation rate ratio versus equivalent strain for Model B (both phases degradable model).

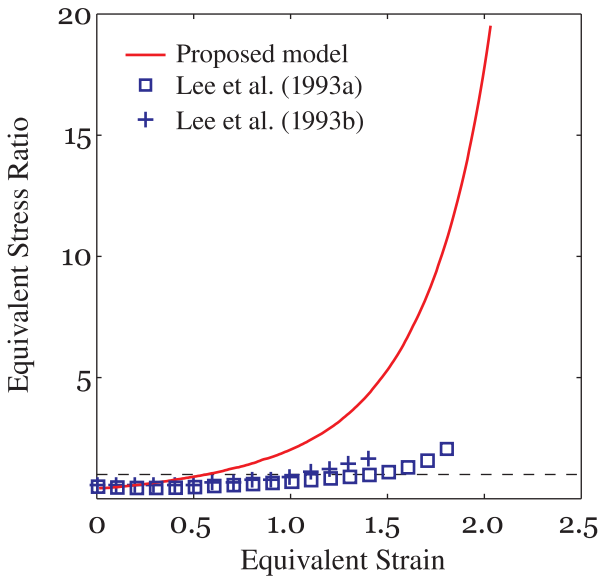

Figure 6.13: Equivalent stress ratio versus equivalent strain for Model A (non-degradable amorphous phase model).

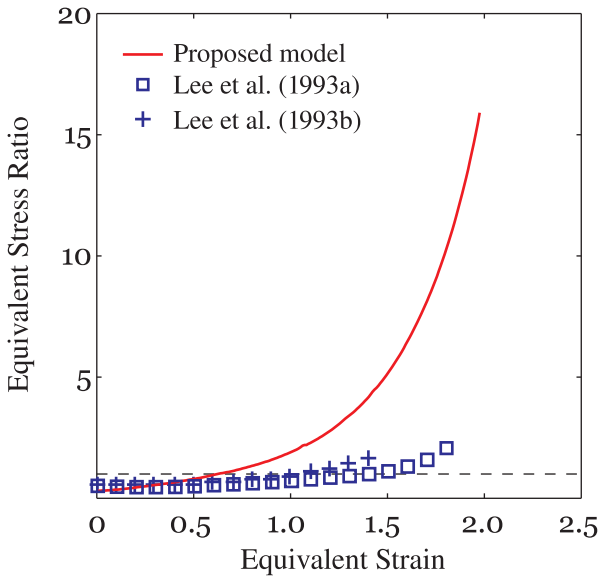

Figure 6.14: Equivalent stress ratio versus equivalent strain for Model B (both phases degradable model).

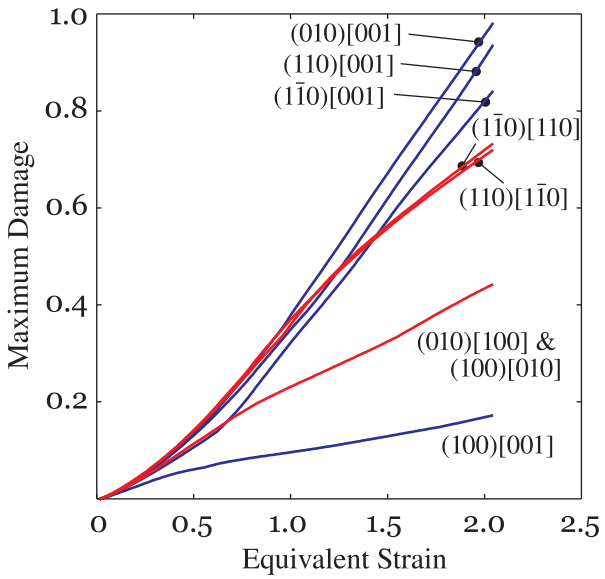

Figure 6.15: Maximum damage versus equivalent strain for the eight slip systems (Model A).

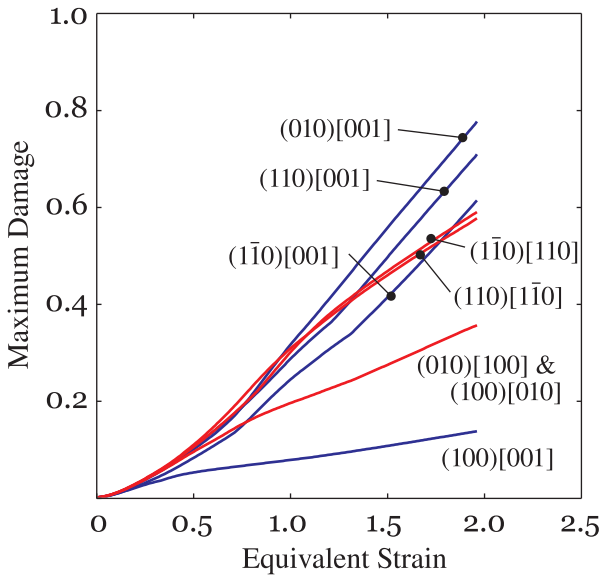

Figure 6.16: Maximum damage versus equivalent strain for the eight slip systems (Model B).

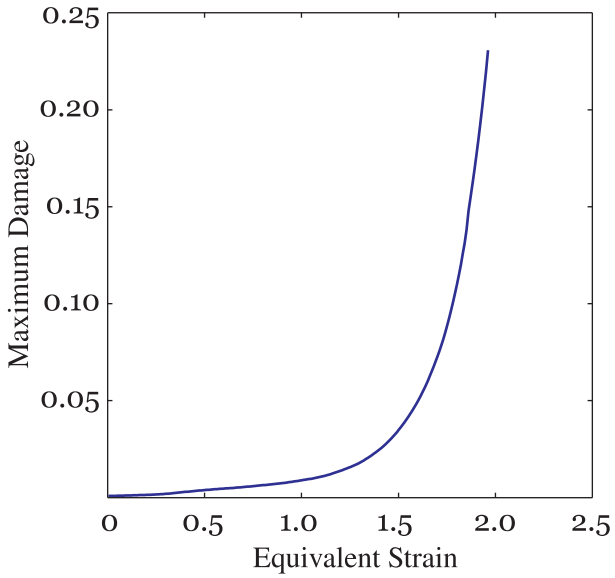

Figure 6.17: Maximum damage versus equivalent strain for the amorphous phase (Model B).

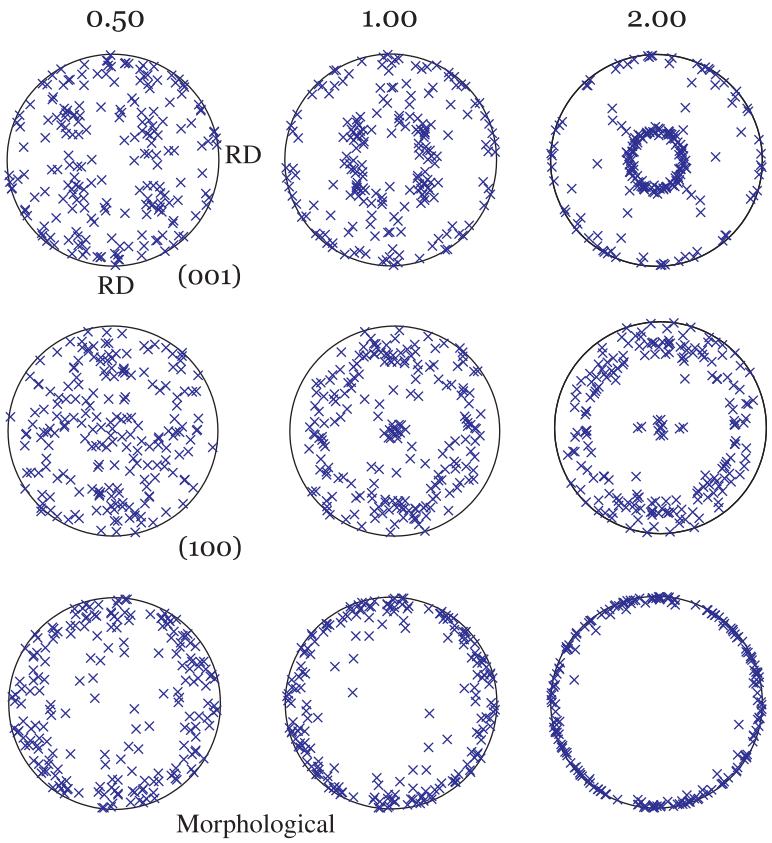

Figure 6.18: Pole figures of the (001) and (100) lattice directions and the morphological texture at equivalent strains of 0.5, 1.0, and 2.0 (Model A) The loading direction is perpendicular to the paper plane.

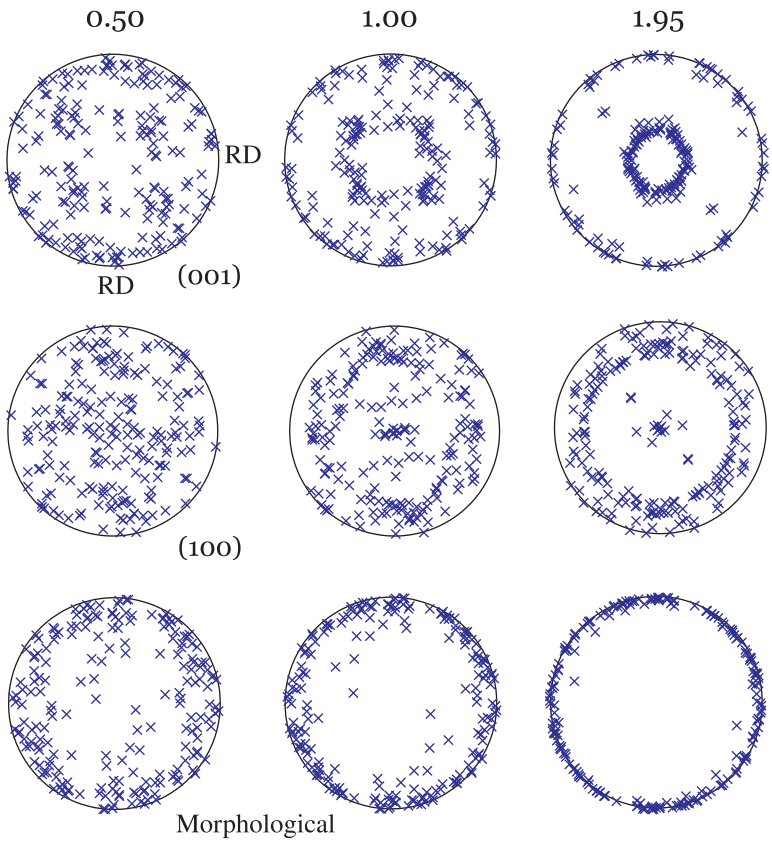

Figure 6.19: Pole figures of the (001) and (100) lattice directions and of the morphological textures at the equivalent strains of 0.5, 1.0, and 1.95 (Model B) The loading direction is perpendicular to the paper plane.

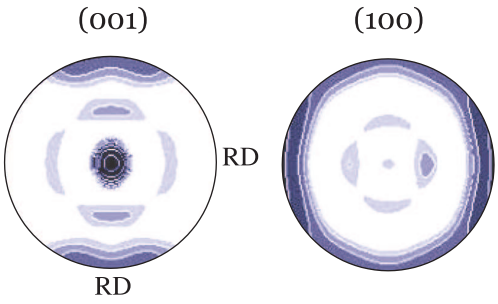

Figure 6.20: Experimental pole figures of the (001) and (100) lattice directions at an equivalent strain of 2.1, as reported by Li et al. (2001)

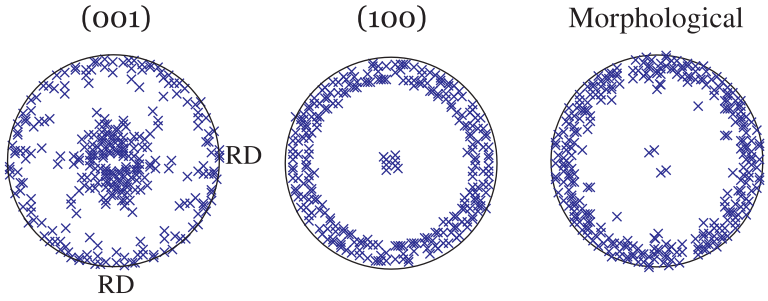

Figure 6.21: Pole figures of the (001) and (100) lattice directions and of the morphological texture at an equivalent strain of 1.0, as predicted by Lee et al.'s (1993b) model.

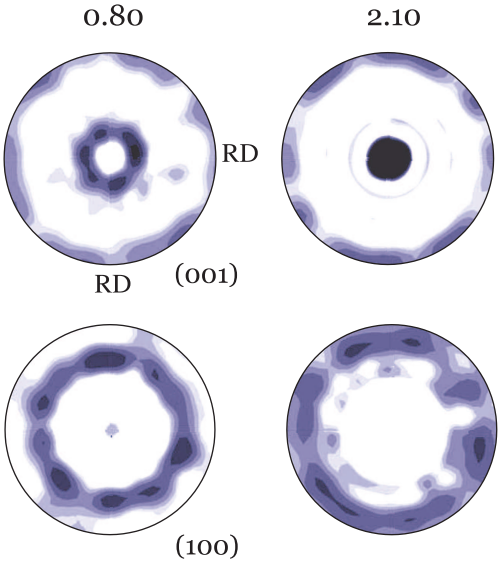

Figure 6.22: Pole figures of the (001) and (100) lattice directions at the equivalent strains of 0.8 and 2.1, as predicted by Nikolov et al.'s (2006) model.

6.7.2 Simple shear

The second case analyzed corresponds to simple shear, where the velocity gradient along the loading path is given as

$$\bar{L}_{ij} = \dot{\gamma} \begin{bmatrix} 0.0 & 1.0 & 0.0 \\ 0.0 & 0.0 & 0.0 \\ 0.0 & 0.0 & 0.0 \end{bmatrix}$$

and where $\dot{\gamma}$ is equal to 0.003 s^{-1}. *Table* 6.3 shows the material parameters used in the examples for the two modelling approaches.

The stress-strain curves obtained by using the first and second approach models are depicted in *Figures* 6.23 and 6.24. The solid line corresponds to the best fit of the models to the experimental data presented by G'Sell et al. (1983). Likewise, these figures also show the responses obtained by Lee et al. (1993b) and Nikolov et al. (2006). From the figure, it is clear that the proposed and the other two viscoplastic models overestimate the stress. For instance, the proposed models are in good agreement with the experimental curve up to a deformation of 0.75; after that straining, the stress rises and the numerical curve moves off the experimental one. Nevertheless, among the three numerical predictions, the proposed damage-coupled model shows a better consistency with the experimental observations. As suggested by Nikolov et al. (2006), the differences between the numerical and experimental behaviour can be attributed to the lack of accuracy of the data obtained from a simple shear test in which the normal stress components are not considered. It is likely that normal stress effects be more pronounced at very large displacements.

Figure 6.25 shows the evolution of the maximum damage in the slip systems. As seen in the figure, one of the most significant characteristics is the slope discontinuities along the different damage curves. According to the model, deformation induces damage with equally importance in the chain and transverse slip systems. Damage evolution is lower in the (010)[100], (100)[010], and (100)[001] systems. Same conclusions can be drawn for *Figure* 6.26, which illustrates the predictions from Model B.

The predicted pole figures are shown in *Figures* 6.28 and 6.29, and compared with the experimental textures obtained by Bartczak et al. (1994), as illustrated in *Figure* 6.30. In simple shear, the model predicts that the (001) and (100) axes align towards the shear direction and plane, respectively. However, as deformation proceeds, the texture patterns

do not become as concentrated as the ones predicted by Lee et al. and Nikolov et al. (*Figures* 6.31 and 6.32). As expected, comparison of the damage-coupled models with Lee et al.'s one shows that the morphological textures largely agree.

In simple shear, Model B predicts the maximum damage evolution for the amorphous phase, as illustrated in *Figure* 6.27. As in the uniaxial tension case, a moderate damage increment is observed at low deformations; however, damage does not evolve at large deformations as sharply as in *Figure* 6.17.

Table 6.3: Material parameters for the simulations under simple shear.

Parameter	**Model A**	**Model B**
Crystalline phase		
Strain rate sensitivity, n^c	5.0	5.0
Reference strain rate, $\dot{\gamma}_0$ [s^{-1}]	0.001	0.001
Damage rate sensitivity, m	2.0	2.0
Reference damage rate, $\dot{\Omega}_0$ [MPa^{-1}]	0.0003	0.00035
Spin release, ζ	2.0	2.0
Crystallinity, χ^c	70	70
Amorphous phase		
Strain rate sensitivity, n^a	5.0	5.0
Reference strain rate, $\dot{\alpha}_0$ or $\dot{\epsilon}_0$ [s^{-1}]	0.001	0.001
Strength τ_0 or σ_0, [MPa]	6.4	6.4
Number of rigid links, N	50	50
Rubbery shear modulus, C_R	1.5	1.5
Critical damage, Ω_∞	NA	1.0
Damage rate, α	NA	0.00005

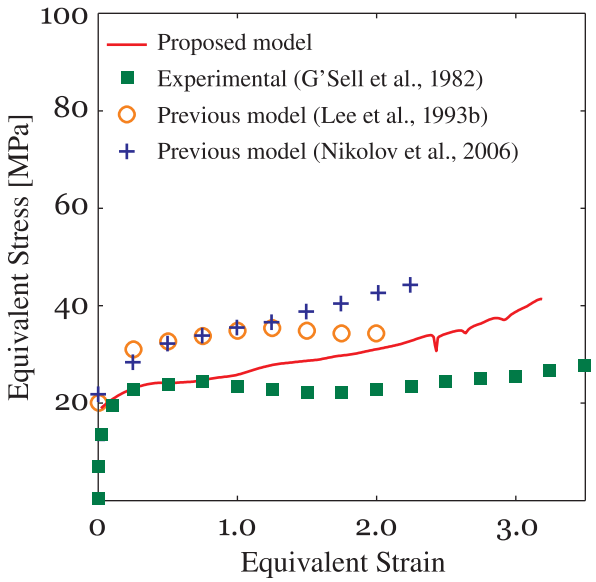

Figure 6.23: Equivalent stress versus equivalent strain behaviour of semicrystalline polyethylene under simple shear for Model A (non-degradable amorphous phase model).

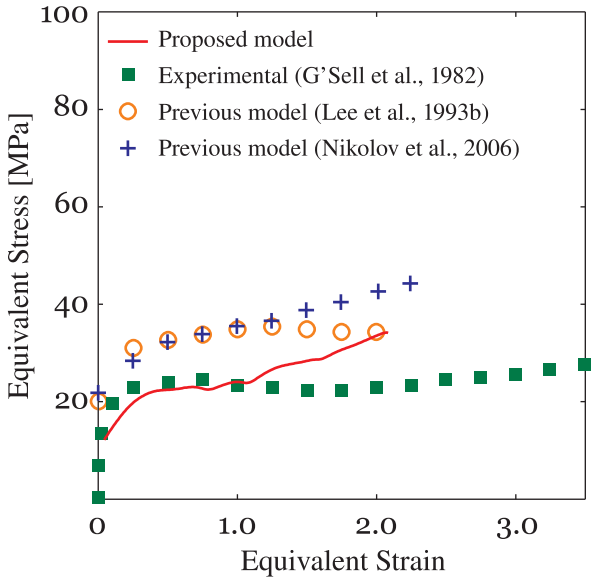

Figure 6.24: Equivalent stress versus equivalent strain behaviour of semicrystalline polyethylene under simple shear for Model B (both phases degradable model).

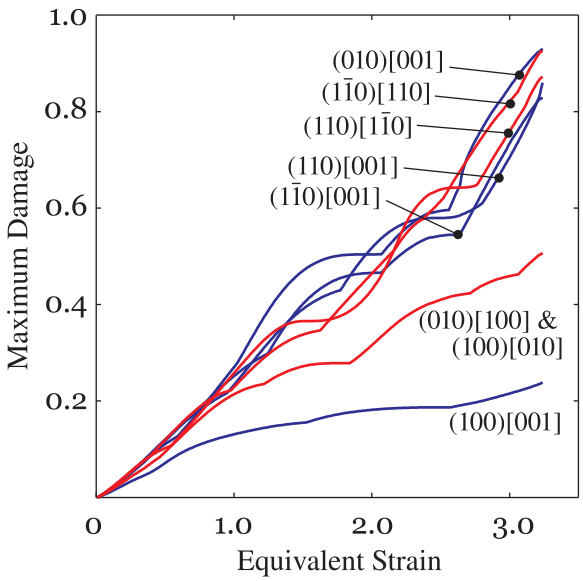

Figure 6.25: Maximum damage versus equivalent strain for the eight slip systems (Model A).

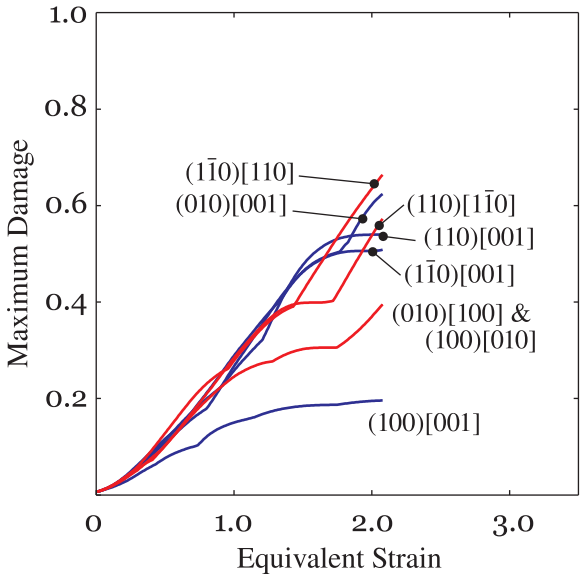

Figure 6.26: Maximum damage versus equivalent strain for the eight slip systems (Model B).

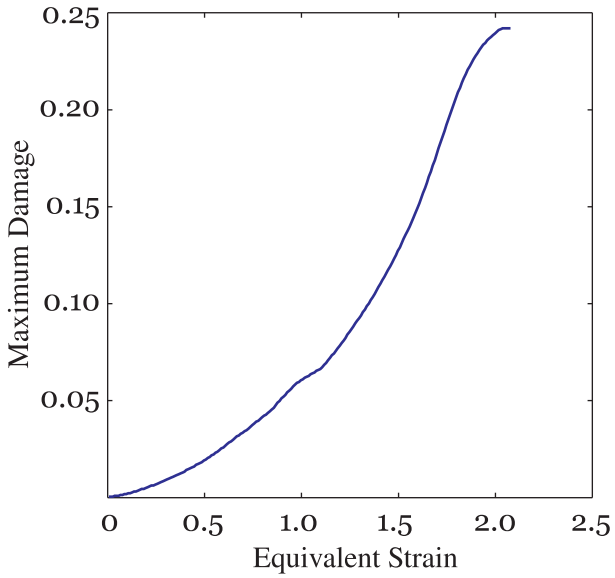

Figure 6.27: Maximum damage versus equivalent strain for the amorphous phase (Model B).

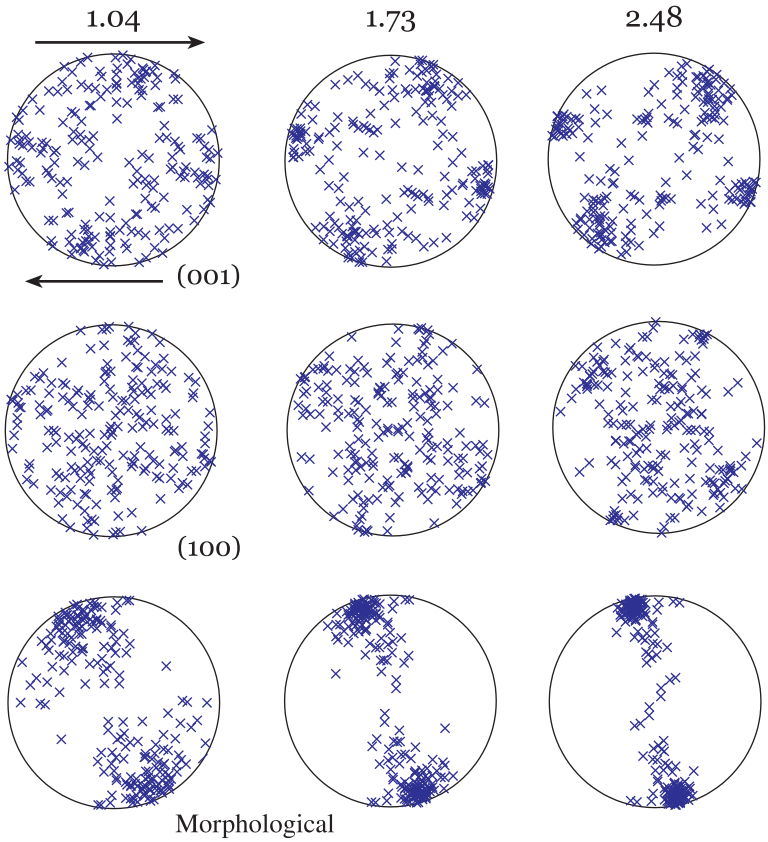

Figure 6.28: Pole figures of the (001) and (100) lattice directions and of the morphological textures at the equivalent strains of 1.04, 1.73, and 2.48 (Model A). The loading direction is indicated by the arrows.

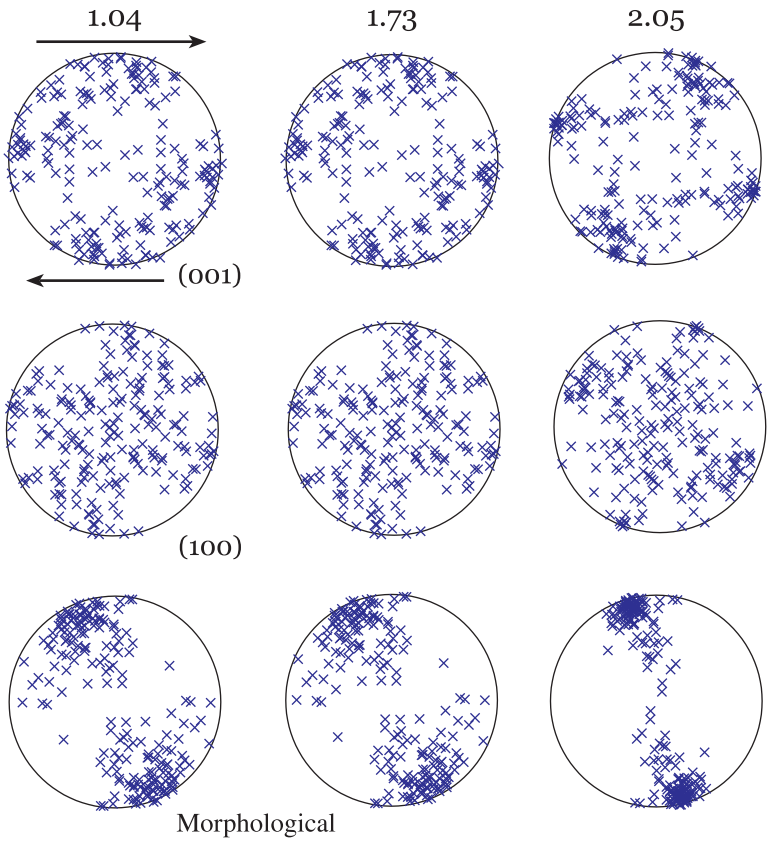

Figure 6.29: Pole figures of the (001) and (100) lattice directions and of the morphological textures at the equivalent strains of 1.04, 1.73, and 2.05 (Model B).

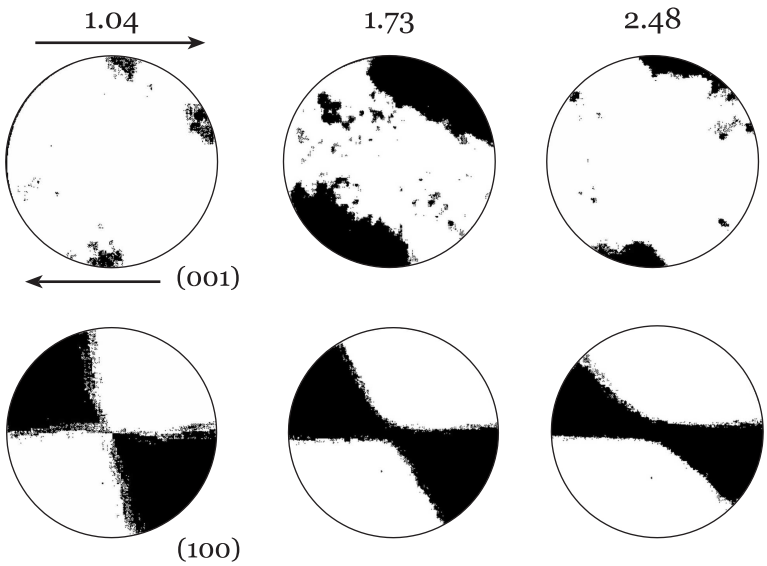

Figure 6.30: Experimental pole figures of the (001) and (100) lattice directions at the equivalent strain of 1.04, 1.73, and 2.48, as reported by Bartczak et al. (1994).

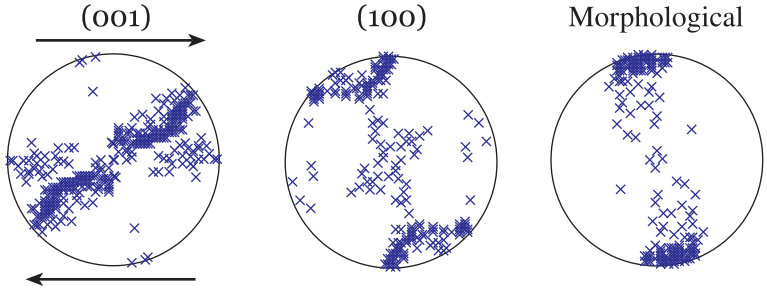

Figure 6.31: Pole figures of the (001) and (100) lattice directions and of the morphological texture at an equivalent strain of 2.0, as predicted by Lee et al.'s (1993b) model.

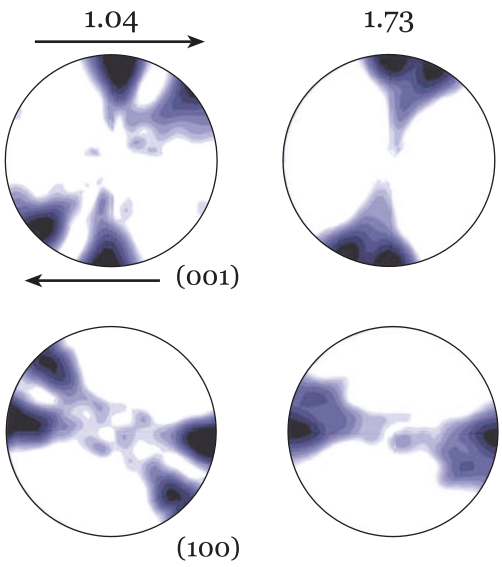

Figure 6.32: Pole figures of the (001) and (100) lattice directions at the equivalent strains of 1.04 and 1.73, as predicted by Nikolov et al.'s (2006) model.

CHAPTER
SEVEN

Computational procedure for modelling of semicrystalline polyethylene

7.1 Introduction

This chapter is intended to present the numerical implementation of the damage-coupled model for semicrystalline polyethylene proposed previously. Organized into two sections, the chapter outlines a comprehensive description of (*i*) how the constitutive equations describing the mechanical behaviour of the inclusion constituents are resolved (local problem) and (*ii*) how the macroscopic stress-strain response is related to the microscopic behaviour of the aggregate of inclusions (global problem). In the second section, some numerical examples showing the influence of the different model parameters on the predictions for stresses, damage, and texture evolution are presented and discussed.

7.2 Solution strategy

The computation of the stress state involves a twice-iterative scheme. The first iteration occurs in the calculation of the local stress state of each one of the inclusion constituents; the amorphous and crystalline phases. The second iteration takes place to determine the stress state that satisfies overall equilibrium in the aggregate at time t_{n+1}. This last algorithm uses a constant time increment, Δt, where $\Delta t \equiv t_{n+1} - t_n$. For the local problem, the equation set to be solved at time t_{n+1} is

$$S^a_{ij} = S^a_{ij}(\bar{S}_{ij}) \tag{7.1}$$

$$S^c_{ij} = S^c_{ij}(\bar{S}_{ij}) \tag{7.2}$$

$$D_{ij}^{a} = \frac{3}{2}\dot{\epsilon}_0 \left(\frac{\sigma_{eq}}{\sigma_0}\right)^{n^a-1} \frac{\frac{S_{ij}^{a}}{1-\Omega} - H'_{ij}}{\sigma_0} \tag{7.3}$$

$$D_{ij}^{c} = M_{ijkl} S_{lk}^{c} \tag{7.4}$$

where $\bar{S}_{ij}$ is the global stress state, and S_{ij}^{a}, S_{ij}^{c}, D_{ij}^{a}, and D_{ij}^{c} are the local stresses and deformation rates for the amorphous and crystalline phases, respectively.

Once the local stresses and deformation rates are estimated, the equations to consider for the global problem are

$$\bar{S}_{ij} = \bar{S}_{ij}(S_{ij}^{a}, S_{ij}^{c}) \tag{7.5}$$

$$\bar{D}_{ij} = \bar{D}_{ij}(D_{ij}^{a}, D_{ij}^{c}) \tag{7.6}$$

7.2.1 Inclusion orientations

As illustrated in *Figure* 7.1, to characterize an inclusion, a set of two orthogonal coordinate systems is specified relative to a fixed coordinate system $X_1X_2X_3$. Let $x_1^i x_2^i x_3^i$ and $x_1^c x_2^c x_3^c$ be coordinate systems describing the inclusion and crystal orientations at any time t, respectively. Using the approach adopted in *Section* 5.2.2, the rotation of the inclusion coordinate system is given by three Eulerian angles: φ, θ, and ψ. This permits a second-order transformation tensor $[Q^i]$ to be written as follows[1]:

$$[Q^i] = \begin{bmatrix} \cos\varphi\cos\psi - \sin\varphi\cos\theta\sin\psi & \sin\varphi\cos\psi + \cos\varphi\cos\theta\sin\psi & \sin\theta\sin\psi \\ -\cos\varphi\sin\psi - \sin\varphi\cos\theta\cos\psi & -\sin\varphi\sin\psi + \cos\varphi\cos\theta\cos\psi & \sin\theta\cos\psi \\ \sin\varphi\sin\theta & -\cos\varphi\sin\theta & \cos\theta \end{bmatrix} \tag{7.7}$$

Then, to describe crystal orientations, the corresponding transformation tensors $[Q^c]$ are defined following the steps:

1. Generate four independent random numbers r_i (i=1,...,4) uniformly distributed on [-1,1]

[1] As in *Chapter* 4, $[\bullet]$ and $\{\bullet\}$ are used to indicate the standard matrix and vector notations, respectively.

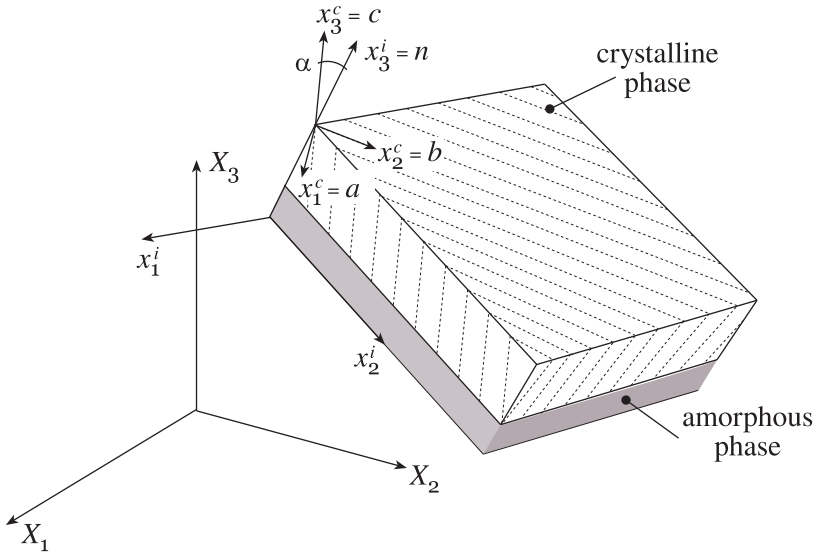

Figure 7.1: Global, inclusion, and crystal coordinate systems.

2. Define the orientation of the vector $\{c\}$ describing the molecule orientation in the crystalline phase

$$c_1 = r_1\sqrt{1-\cos^2\alpha}, \quad c_2 = \sqrt{1-\cos^2\alpha - n_1^2}, \quad \text{and} \quad c_3 = \cos\alpha \tag{7.8}$$

where α is the angle between the chain direction c and plane normal n, as shown in *Figure* 7.1

3. Define an auxiliary vector with an orientation given by the random numbers r_i (i=2,3,4)

$$\{u\} = \{u_1, u_2, u_3\}^{\mathrm{T}} = \{r_2, r_3, r_4\}^{\mathrm{T}} \tag{7.9}$$

4. Define the vectors $\{a\}$ and $\{b\}$ as

$$\{a\} = \frac{\{c\}\times\{u\}}{|\{c\}\times\{u\}|} \quad \text{and} \quad \{b\} = \frac{\{c\}\times\{a\}}{|\{c\}\times\{a\}|} \tag{7.10}$$

5. Compute the transformation tensor representing the crystal orientation

$$[Q^c] = \begin{bmatrix} \{a\}^{\mathrm{T}} \\ \{b\}^{\mathrm{T}} \\ \{c\}^{\mathrm{T}} \end{bmatrix} = \begin{bmatrix} a_1 & a_2 & a_3 \\ b_1 & b_2 & b_3 \\ c_1 & c_2 & c_3 \end{bmatrix} = \begin{bmatrix} Q_{11} & Q_{12} & Q_{13} \\ Q_{21} & Q_{22} & Q_{23} \\ Q_{31} & Q_{32} & Q_{33} \end{bmatrix} \tag{7.11}$$

6. Repeat steps 1 to 5 to generate the remainder of crystal orientations

Once reduced to five-dimensional vectors, stresses $\{S\}$ and deformation rates $\{D\}$ are supposed to be transformed under a change in coordinate system as

$$\{D'\} = [\tilde{Q}]\{D\} \tag{7.12}$$

where $[\tilde{Q}]$ is a 5×5 reduced transformation matrix given as a function of the rotation matrix components of *Equation* 7.11 as

$$[\widetilde{Q}] = \begin{bmatrix} \frac{1}{2}(Q_{11} - Q_{21} - Q_{12} + Q_{22}) & \frac{\sqrt{3}}{6}(-Q_{11} - Q_{21} + 2Q_{31} + Q_{12} + Q_{22} - 2Q_{32}) & \frac{\sqrt{2}}{2}(Q_{41} - Q_{42}) & \frac{\sqrt{2}}{2}(Q_{51} - Q_{52}) & \frac{\sqrt{2}}{2}(Q_{61} - Q_{62}) \\ \frac{\sqrt{3}}{6}(-Q_{11} + Q_{21} - Q_{12} + Q_{22} + 2Q_{13} - 2Q_{23}) & \frac{1}{6}(Q_{11} + Q_{21} - 2Q_{31} + Q_{12} + Q_{22} - 2Q_{32} - 2Q_{13} - 2Q_{23} + 4Q_{33}) & \frac{\sqrt{6}}{6}(-Q_{41} - Q_{42} + 2Q_{43}) & \frac{\sqrt{6}}{6}(-Q_{51} - Q_{52} + 2Q_{53}) & \frac{\sqrt{6}}{6}(-Q_{61} - Q_{62} + 2Q_{63}) \\ \frac{\sqrt{2}}{2}(Q_{14} - Q_{24}) & \frac{\sqrt{2}}{2}(Q_{15} - Q_{25}) & \frac{\sqrt{2}}{2}(Q_{16} - Q_{26}) & & \\ \frac{\sqrt{6}}{6}(-Q_{14} - Q_{24} + 2Q_{34}) & \frac{\sqrt{6}}{6}(-Q_{15} - Q_{25} + 2Q_{35}) & \frac{\sqrt{6}}{6}(-Q_{16} - Q_{26} + 2Q_{36}) & & \\ Q_{44} & Q_{45} & Q_{46} & & \\ Q_{54} & Q_{55} & Q_{56} & & \\ Q_{64} & Q_{65} & Q_{66} & & \end{bmatrix} \tag{7.13}$$

7.2.2 Local iterative procedure

The local problem object is to determine the stress state of each one of the inclusions in the aggregate. To do that, a Newton-Raphson iterative approach is used to solve the constitutive equations governing the behaviour of the amorphous and crystalline phases. After enforcing traction equilibrium across the amorphous-crystalline interface, the principal unknowns of the local problem are the S^c_{11}, S^c_{22}, and S^c_{12} stress components of the crystalline phase. For each iteration, internal variables are assumed to remain invariant and chosen to be at the values of the previous time step. Only local stresses are updated by following the next iterative algorithm:

1. Rotate the global stress into the inclusion coordinate system,

$$\{\bar{S}\}^i = [\tilde{Q}^i]\{\bar{S}\} \tag{7.14}$$

2. Guess an initial trial stress,

$$\{S^g\} = \{S_1^g, S_2^g, S_3^g\}^{\mathrm{T}} \tag{7.15}$$

3. Compute the stress state for the amorphous and crystalline phases,

$$\{S^a\} = \left\{\frac{1}{1-f^c}(\bar{S}_1^i - f^c S_1^g), \frac{1}{1-f^c}(\bar{S}_2^i - f^c S_2^g), \bar{S}_3^i, \bar{S}_4^i, \frac{1}{1-f^c}(\bar{S}_5^i - f^c S_3^g)\right\}^{\mathrm{T}} \tag{7.16}$$

$$\{S^c\}^i = \{S_1^g, S_2^g, \bar{S}_3^i, \bar{S}_4^i, S_3^g\}^{\mathrm{T}} \tag{7.17}$$

4. Compute the amorphous deformation rate $\{D^a\}$ following the steps given in *Section* 7.2.3
5. Compute the crystalline deformation rate $\{D^c\}$ according to the steps given in *Section* 7.2.4
6. Evaluate the equation system residual,

$$\begin{cases} H_1 = \frac{\sqrt{2}}{2}(D_1^c - D_1^a) - \frac{\sqrt{6}}{6}(D_2^c - D_2^a) \\ H_2 = \frac{\sqrt{2}}{2}(D_1^c - D_1^a) + \frac{\sqrt{6}}{6}(D_2^c - D_2^a) \\ H_3 = D_5^c - D_5^a \end{cases} \tag{7.18}$$

7. Compute the Jacobian matrix,

$$[J]_k = \partial\{H\}_k / \partial\{S^g\}_k \tag{7.19}$$

8. Solve the equation system,

$$[J]_k\{\Delta S^g\} = -\{H\}_k, \tag{7.20}$$

where $\{\Delta S^g\}$ is the stress increment between iterative steps k and $k+1$

9. Compute the new residual,

$$\{H\}_{k+1} = \{H\}_k + [J]_k\{\Delta S^g\} \tag{7.21}$$

10. Update the reduced stress,

$$\{S^g\}_{k+1} = \{S^g\}_k + \{\Delta S^g\} \tag{7.22}$$

11. Repeat steps 3 to 10 until the norm of the residual $\|\{H\}_{k+1}\|$ becomes smaller than the given tolerance
12. Compute the inclusion deformation rate and stress states once local convergence is reached, *i.e.*,

$$\{D^i\} = (1-\chi^c)\{D^a\} + \chi^c\{D^c\} \tag{7.23a}$$

$$\{S^i\} = (1-\chi^c)\{S^a\} + \chi^c\{S^c\} \tag{7.23b}$$

13. Repeat above steps to calculate the local deformation and stress states for the remainder of inclusions

7.2.3 Amorphous phase modelling

The following steps describe how deformation rates as well as back stress tensors and damage evolution are determined. The constitutive equations for the amorphous phase are determined in the inclusion coordinate system $x_1^i x_2^i x_3^i$.

Back stress tensor and damage updating

1. Rotate the deformation gradient tensor from the global into the inclusion coordinate system

$$[F^a] = [Q^i][F^a][Q^i]^{\mathrm{T}} \tag{7.24}$$

2. Compute the left Cauchy-Green deformation tensor

$$[B^a] = [F^a] \cdot [F^a]^{\mathrm{T}} \tag{7.25}$$

3. Vectorize the left Cauchy-Green deformation tensor

$$[B^a] \rightarrow \{B^a\}_6 \tag{7.26}$$

4. Compute the first invariant

$$I_1 = B_1^a + B_2^a + B_3^a \tag{7.27}$$

5. Compute the Langevin function

$$\mathcal{L}^{-1}\left(\sqrt{I_1/3N}\right) \tag{7.28}$$

6. Compute the deviatoric back stress tensor

$$\{H'\} = \frac{C_R}{3}\sqrt{\frac{3N}{I_I}}\mathcal{L}^{-1}\left(\sqrt{\frac{I_I}{3N}}\right)(\{B^a\} - \tfrac{1}{3}I_I\{I\}) \tag{7.29}$$

7. Compute the strain energy,

$$W = C_R N\left[\beta\sqrt{\frac{I_I}{3N}} + \ln\frac{\beta}{\sinh\beta}\right] \tag{7.30}$$

8. Compute damage value for the amorphous phase,

$$\Omega = \Omega_\infty[1 - \exp(-\alpha W^2)] \tag{7.31}$$

Stress-deformation rate relationship

1. Compute the equivalent stress

$$\sigma_{eq} = \sqrt{\frac{3}{2}\left(\frac{\{S^a\}}{1-\Omega} - \{H'\}\right)^{\mathrm{T}} \cdot \left(\frac{\{S^a\}}{1-\Omega} - \{H'\}\right)} \tag{7.32}$$

2. Compute the amorphous deformation rate

$$\{D^a\} = \frac{3}{2}\dot{\epsilon_0}\left(\frac{\sigma_{eq}}{\sigma_0}\right)^{m-1}\frac{\frac{\{S^a\}}{1-\Omega} - \{H'\}}{\sigma_0} \tag{7.33}$$

7.2.4 Crystalline phase modelling

The stress-deformation rate relationship and damage evolution for the crystalline phase are obtained from the damage-coupled constitutive model proposed, assuming a deformation driven case. The related equations are solved in the crystal coordinate system $x_1^c x_2^c x_3^c$.

Stress-deformation rate relationship

1. Rotate the crystal stress tensor from the inclusion to the crystal coordinate system

$$\{S^c\} = [\tilde{Q}^c][\tilde{Q}^i]^{\mathrm{T}}\{S^c\}^i \tag{7.34}$$

2. Compute the reduced crystal stress tensor

$$\{S^{c*}\} = \{S^c_{1i}, 0, S^c_{3i}, S^c_{4i}, S^c_{5i}\}^{\mathrm{T}} \tag{7.35}$$

3. Compute the 5×5 crystal compliance tensor

$$[M_c]_k = \dot{\gamma}_0 \sum\nolimits_\alpha \frac{|\{S^{c*}\}_k \{R^\alpha\}|^{n-1}}{[(1-\Omega^\alpha) g^\alpha]^n} \{R^\alpha\}\{R^\alpha\}^{\mathrm{T}} \tag{7.36}$$

4. Compute the crystal deformation rate

$$\{D^c\} = [M]\{S^{c*}\} \tag{7.37}$$

where $\{D^c\} = \{D^c_1, D^c_2, D^c_3, D^c_4, D^c_5\}^{\mathrm{T}}$

5. Rotate the deformation rate to the inclusion coordinate system

$$\{D^c\}^i = [Q^i][Q^c]^{\mathrm{T}}\{D^c\} \tag{7.38}$$

Damage updating

1. Compute the damage rate for each slip system according to the following evolution law

$$\dot{\Omega}^\alpha_{n+1} = \dot{\Omega}_0 \left| \frac{\{S^*_c\}\{R^\alpha\}}{(1-\Omega^\alpha_n) g^\alpha} \right|^m \tag{7.39}$$

2. Update Ω^α_{n+1},

$$\Omega^\alpha_{n+1} = \Omega^\alpha_n + \dot{\Omega}^\alpha_{n+1} \Delta t \tag{7.40}$$

7.2.5 Global iterative procedure

After solving individually the stress-strain state in all the inclusions, the global stress $\{\bar{S}\}$ and deformation rate $\{\bar{D}\}$ are determined as the volume average of the corresponding local variables, $\{S^i\}$ and $\{D^i\}$ The volume fraction is given as $v^i = V^i/V$, where V^i and V represent the inclusion and aggregate volumes, respectively. The following iterative algorithm contains the key steps for integrating the global problem.

1. Compute the global deformation rate,

$$\{\bar{D}\} = \sum\nolimits_i v^i [\tilde{Q}^i]^{\mathrm{T}} \{D^i\} \tag{7.41}$$

2. Compute the global stress,

$$\{\bar{S}\} = \sum_i v^i [\tilde{Q}^i]^{\mathrm{T}} \{S^i\} \tag{7.42}$$

3. Compute the equivalent average and global deformation rate,

$$\hat{\bar{D}} = \sqrt{\tfrac{2}{3}\{\bar{D}\}^{\mathrm{T}} \cdot \{\bar{D}\}} \quad \text{and} \quad \hat{D} = \sqrt{\tfrac{2}{3}\{D\}^{\mathrm{T}} \cdot \{D\}} \tag{7.43}$$

4. Correct the unknown stress components

$$\bar{S}_u\big|_{k+1} = \omega \bar{S} + (1-\omega)\bar{S}\big|_k \tag{7.44}$$

where $\omega \in [0,1]$ is an under-relaxation parameter. The explicit and implicit integrations correspond to $\omega = 0$ and $0 < \omega \leq 1$, respectively

5. Repeat the local and global procedures until $\left|\hat{\bar{D}} - \hat{D}\right|$ satisfies the required tolerance

7.2.6 Texture updating

During the iterative process, crystallographic and morphological texture at time t_{n+1} are updated based on the corresponding ones at time t_n, once the global problem is satisfied. The new crystal orientations are described by following the steps outlined in *Section* 5.2.9. On the other hand, interface plane orientations are updated according to the following algorithm:

1. Update the deformation gradient tensor

$$[F^a]_{n+1} = [I - \omega L^a \Delta t]^{-1} [I + (1-\omega) L^a \Delta t][F^a]_n \tag{7.45}$$

Initially, $[F^a]_{n=1} = [I]$

2. Update the normal vector

$$\{n\}_{n+1} = [F^a]^{-T} \{n\}_n \tag{7.46}$$

3. Update the in-plane vectors

$$\{v\}_{n+1} = [F]\{v\}_n \quad \text{and} \quad \{w\}_{n+1} = \{n\} \times \{v\}_n \tag{7.47}$$

7.3 Numerical examples

In this section, the comparison of the influence of some of the model parameters on the overall behaviour is carried out. In the first part, the influence of the number of rigid links and of the tilt angle is studied. Then, in the second part, three examples of the influence of the three sets of parameters; crystalline phase damage rate and release parameter, amorphous phase damage rate and saturation damage, and rubber shear modulus and amorphous phase strength, are reviewed. An aggregate of 100 randomly oriented composite inclusions is considered for the simulations under uniaxial tension. As explained in *Section* 5.3, global deformation rate and deviatoric stress are assumed to have reduced forms, *i.e.*,

$$\{\bar{D}\} = \{?, \bar{D}_2, ?, ?, ?, ?\}^{\mathrm{T}}, \text{ and } \{\bar{S}\} = \{?, ?, ?, 0, 0, 0\}^{\mathrm{T}} \tag{7.48}$$

respectively, where $\bar{D}_2$ is the enforced deformation rate. The rest of the non-prescribed components, written as question marks, are the associated unknowns. The deformation rate components along the transverse directions are written as

$$\bar{D}_1 = \bar{D}_3 = -\tfrac{1}{2}\bar{D}_2 \tag{7.49}$$

7.3.1 Influence of the number of rigid links

Figures 7.2 to 7.4 show the influence of the average number of rigid links between entanglement points N on the global stress response and on the amorphous and crystalline phase damage, obtained in uniaxial tension after 0.5, 1.0, 1.5, 1.8, and 2.0 equivalent strains. For instance, *Figure* 7.2 shows the evolution of the equivalent stress for values of the number of links ranging from 10 to 200. From this figure, it is seen the model predicts (*i*) no significant influence on the stress state at low straining levels (below 1.0) and (*ii*) at large straining levels stress lessens as the number of links increases. This decrease is less significant when N is larger than 50; a value from which the curves gradually tend to level off. *Figure* 7.3 illustrates that damage evolution in the amorphous phase is roughly analogous to what happens to the global stress; however, at large deformations, damage continues decreasing slightly as the number of links increases. On the other hand, *Figure* 7.4 confirms that damage evolution in the crystalline phase is not directly affected by N. As can be seen, at least for the five responses shown, the damage values stay relatively constant for a given straining level. That is because no interrelations were

established between the number of rigid links and the damage evolution law proposed in the model. As a final remark, the responses of stress and damage indicate that the number of rigid links is an important parameter from the material morphology contributing to its mechanical behaviour. An explanation for the higher stress and damage values at low number of rigid links is that entanglements tend to keep molecules associated together, requiring more energy (larger forces) to stretch the molecular network.

7.3.2 Influence of the tilt angle

To test the sensitivity of the results to the ascribed tilt angle, its relative influence on the global stress and damage on the material phases is displayed in *Figures* 7.5 to 7.7 for a range of angles between 15 and 45° and for a selection of five different strain levels; $\hat{\varepsilon}$=0.5, 1.0, 1.5, 1.8, and 2.0. No attempts to describe the interfacial structure or to explain its mechanical properties were made. From the simulations, it can be inferred that tilt angle does not affect significantly model predictions. For instance, as shown in *Figure* 7.5, no significant changes of the global stress are observed for the deformations of 0.5, 1.0, 1.5, and 1.8, and only a minor decrease is observed for a straining level of 2.0. Nevertheless, no convergence is found when the tilt angle is larger than 35°. Similar behaviour is noticed in the damage plots (*Figures* 7.6 and 7.7). At large deformations, amorphous phase damage decreases slightly as the tilt angle increases; while for the crystalline phase, there is a gradual increase in damage between 15 and 30°, and a more marked rise after 30°.

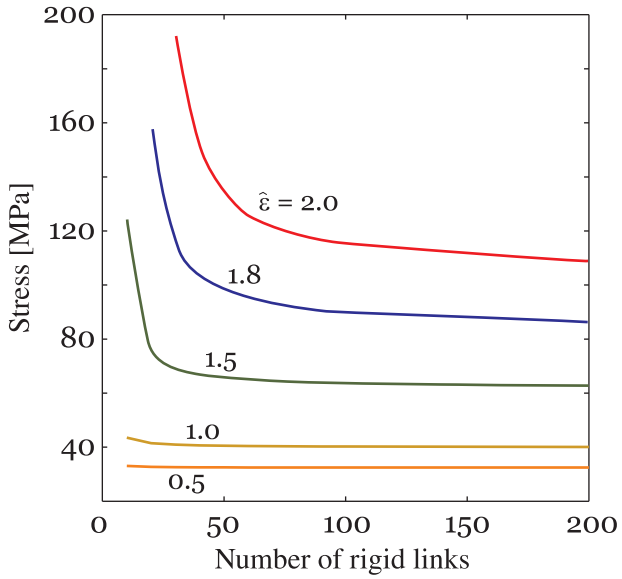

Figure 7.2: Influence of the number of rigid links on the global stress response.

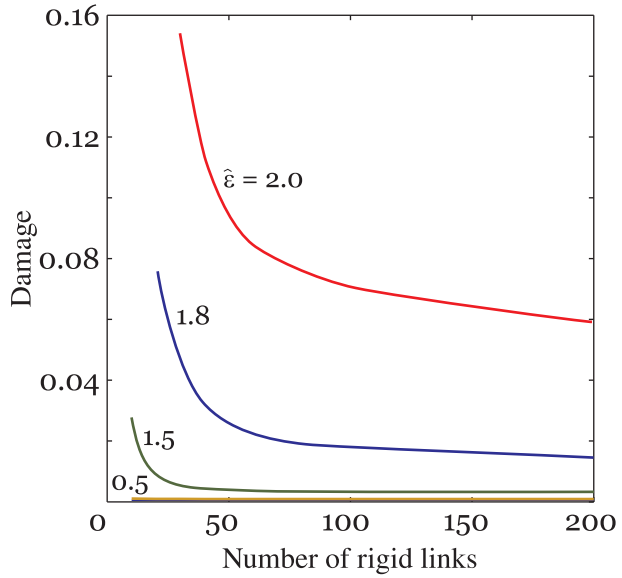

Figure 7.3: Influence of the number of rigid links on the amorphous phase damage.

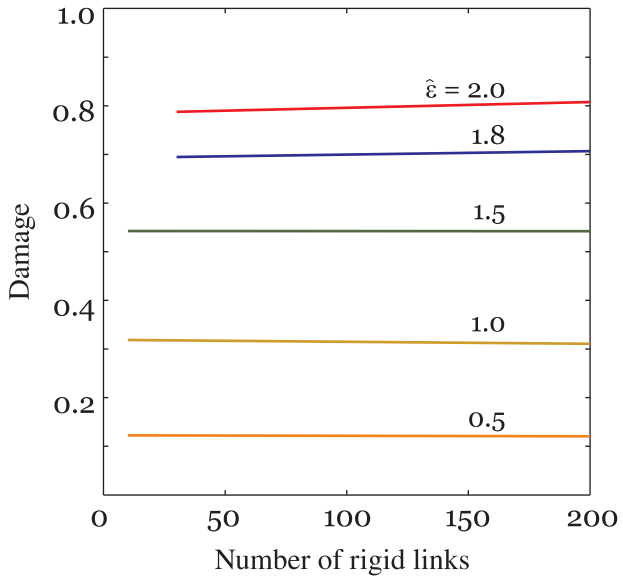

Figure 7.4: Influence of the number of rigid links on the crystalline phase damage.

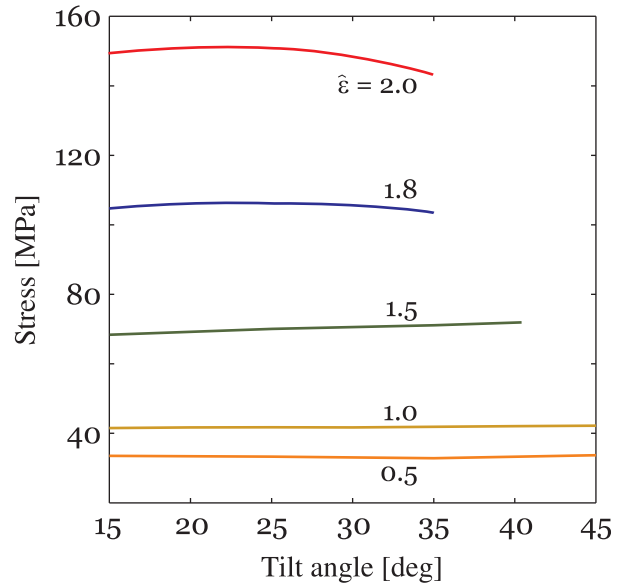

Figure 7.5: Influence of the tilt angle on the global stress response.

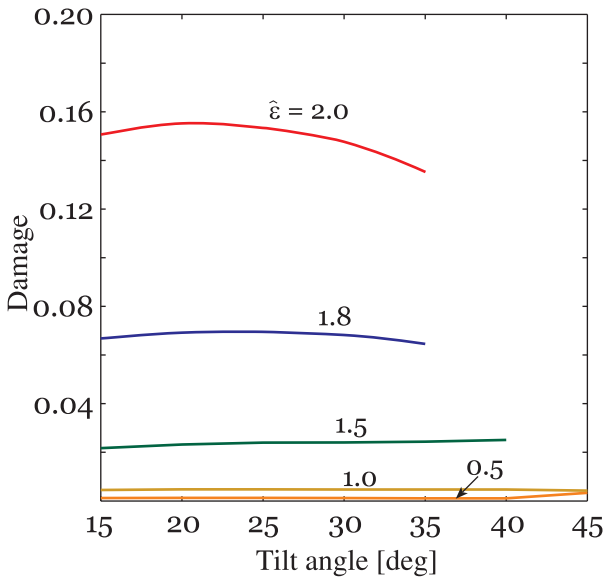

Figure 7.6: Influence of the tilt angle on the amorphous phase damage.

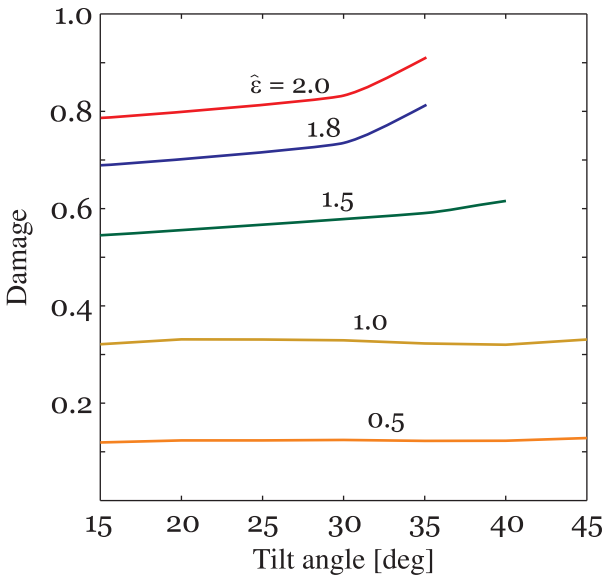

Figure 7.7: Influence of the tilt angle on the crystalline phase damage.

7.3.3 Influence of the damage rate $\dot{\Omega}_0$ and release parameter ζ

Figures 7.8 to 7.10 illustrate how much numerical predictions of global stress, crystalline phase damage, and texture are affected by the choice of the damage rate $\dot{\Omega}_0$ and release ζ parameters in the model. Considering damage rate values from 1.0×10^{-4} to 3.0×10^{-4} and release values from 4.0 to 8.0, the results shown were obtained assuming no damage of the amorphous phase at an equivalent strain of 1.8. *Figure* 7.8 shows that upon increasing the parameter values, global stress becomes larger. However, above a damage rate of 2.5×10^{-4}, global stress diminishes because of the damage levels reached; larger than 0.7, as shown in *Figure* 7.9. The plot of *Figure* 7.9 reveals that the release parameter does not have an important influence on damage evolution. From the contour plot of *Figure* 7.9, it can be seen that for a constant value of damage rate, damage in the crystalline phase practically remains invariant as the release parameter increases. Contrarily, as expected, damage rate increments speed up damage of the crystalline phase when the release parameter is kept constant. *Figure* 7.10 presents the (001) texture for nine simulations obtained by combining three different values of $\dot{\Omega}_0$ and three values of ζ. It is observed that as both $\dot{\Omega}_0$ and ζ increase, the poles rotate more rapidly towards the loading directions; the strongest texture occurs for the largest values of $\dot{\Omega}_0$ and ζ. It confirms the hypothesis that texture evolution can be numerically controlled by adjusting these two parameters.

7.3.4 Influence of the damage rate α and saturation damage Ω_∞

In the model, the parameters describing the damage evolution in the amorphous phase are the damage rate α and saturation damage Ω_∞. The influence of these two parameters on global stress and damage of the amorphous phase is analyzed in *Figures* 7.11 and 7.12, respectively. For values of damage rate and saturation damage ranging from 1.0×10^{-6} to 5.0×10^{-6} and from 0.75 to 0.95, respectively, the model results are quite more sensible to variations of α than of Ω_∞, as shown in *Figures* 7.11 and 7.12. Likewise, it can be seen from the respective figures that as damage rate increases, the amorphous phase becomes more highly damaged and the material carries less stress.

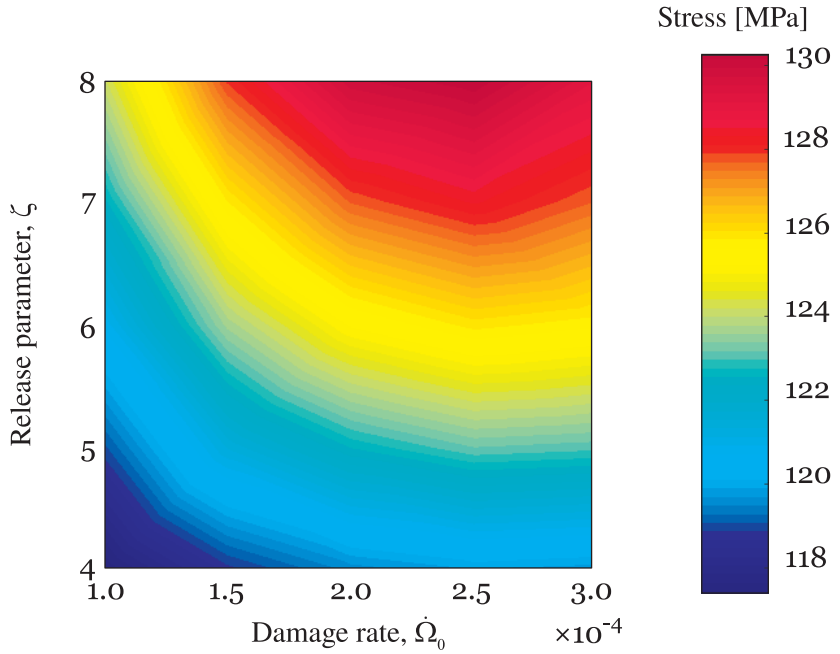

Figure 7.8: Effects of increasing damage rate and release parameters on the stress state.

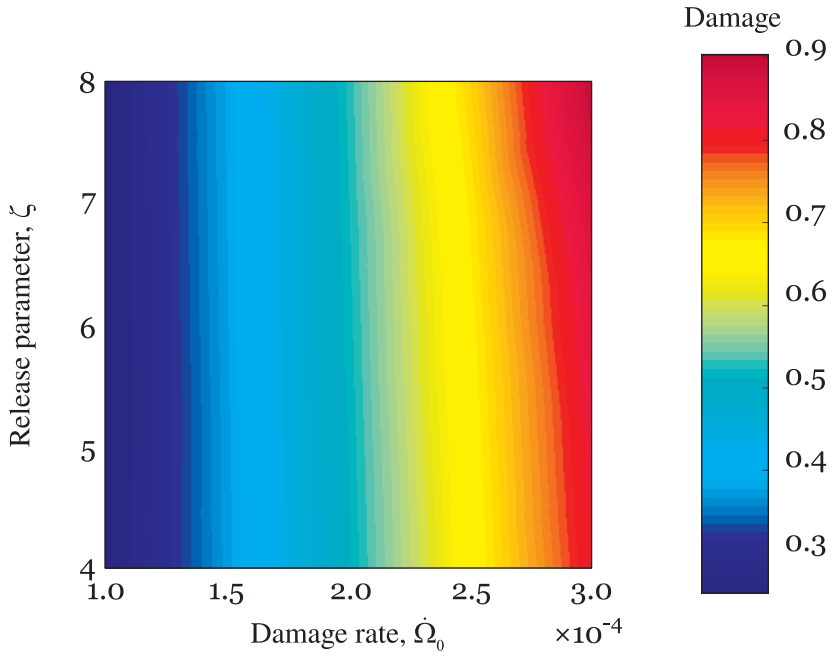

Figure 7.9: Effects of increasing damage rate and release parameters on damage of the crystalline phase.

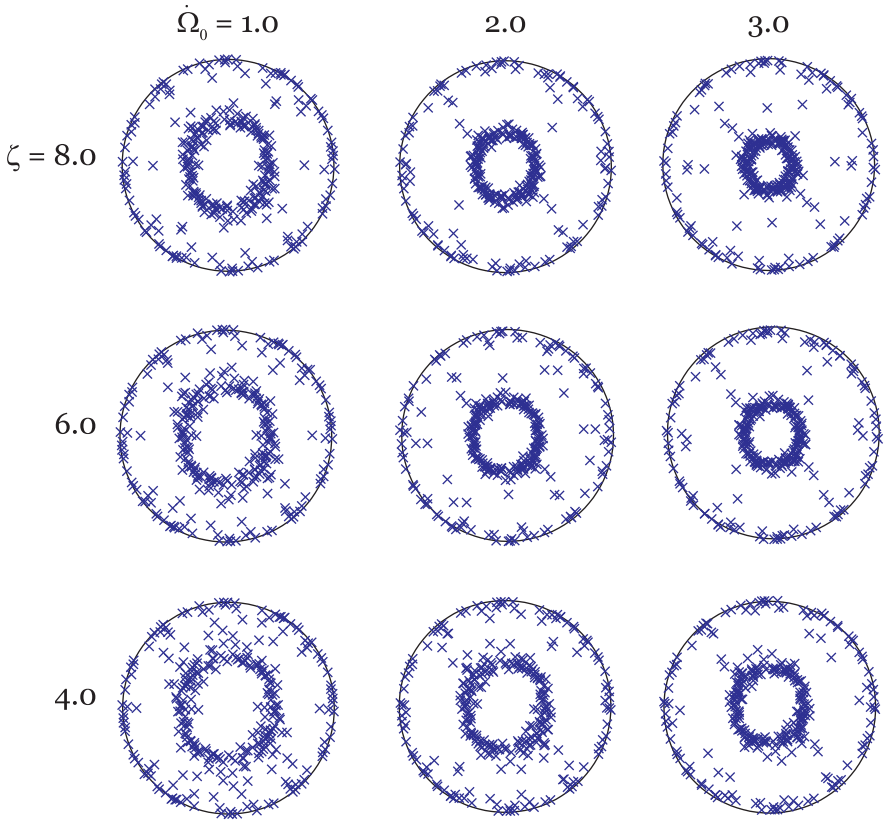

Figure 7.10: Effects of increasing damage rate and release parameters on texture evolution.

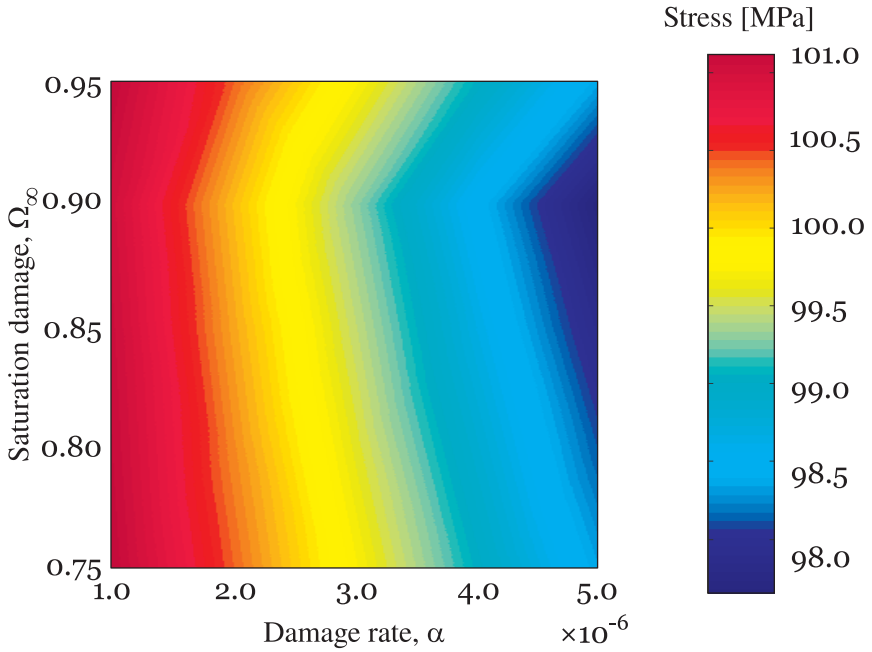

Figure 7.11: Effects of increasing damage rate and saturation damage on the stress state.

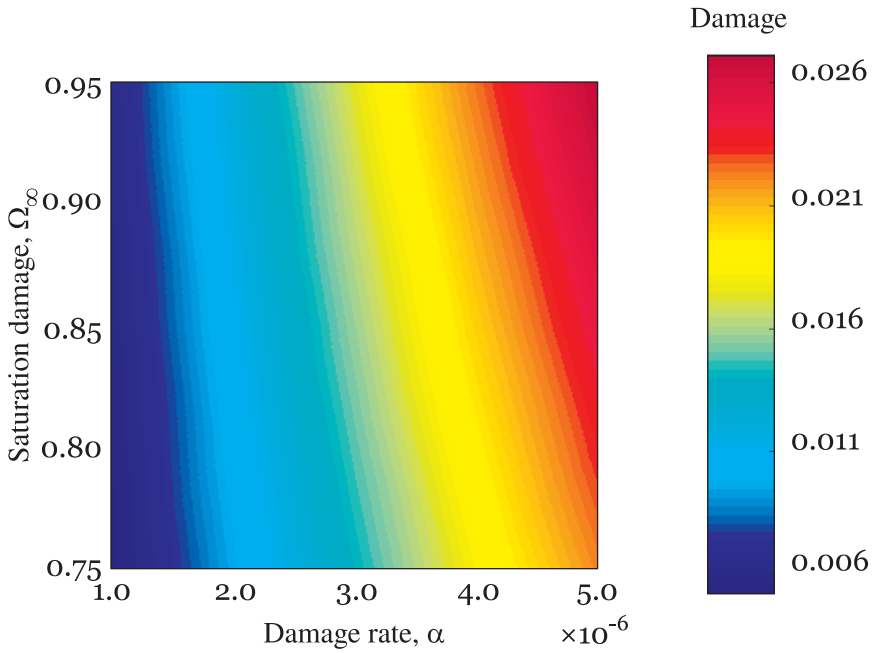

Figure 7.12: Effects of increasing damage rate and saturation damage on damage of the amorphous phase.

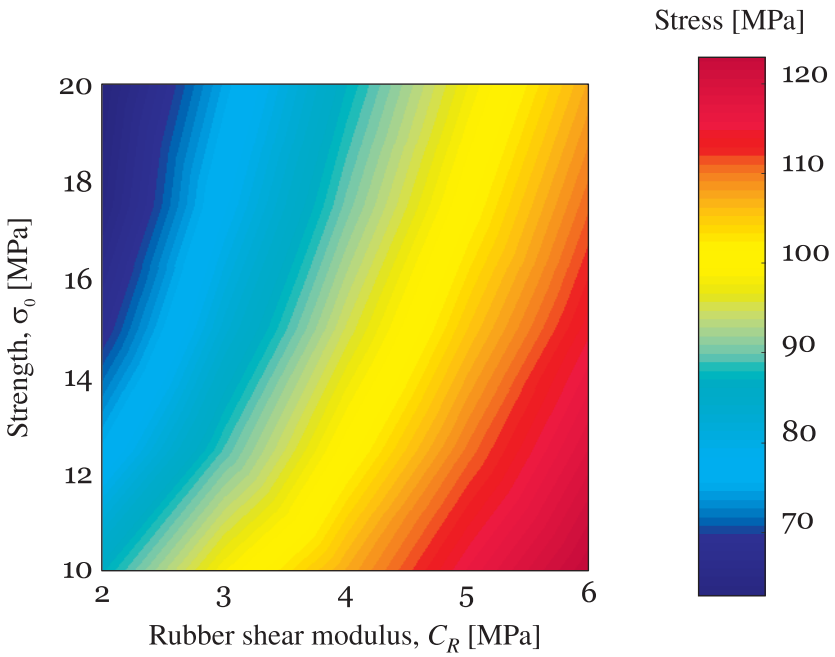

Figure 7.13: Effects of increasing rubber shear modulus and amorphous phase strength on the stress state.

7.3.5 Influence of the rubber shear modulus C_R and amorphous phase strength σ_0

Figures 7.13 to 7.15 show the contour plots of the influence of the rubber shear modulus C_R and amorphous phase strength σ_0 on the predicted global stress and damage evolution of the constitutive phases. Considering that rubber shear modulus and amorphous phase strength values range from 2.0 to 6.0 and from 10.0 to 20.0 MPa, the material becomes more stressed as C_R increases and σ_0 decreases. *Figures* 7.14 and 7.15 display the effects on the amorphous and crystalline phase damage. It is obvious from *Figure* 7.14 that damage in the amorphous phase becomes a little more pronounced for large values of strength. Similar behaviour is observed in the crystalline phase damage (*Figure* 7.15).

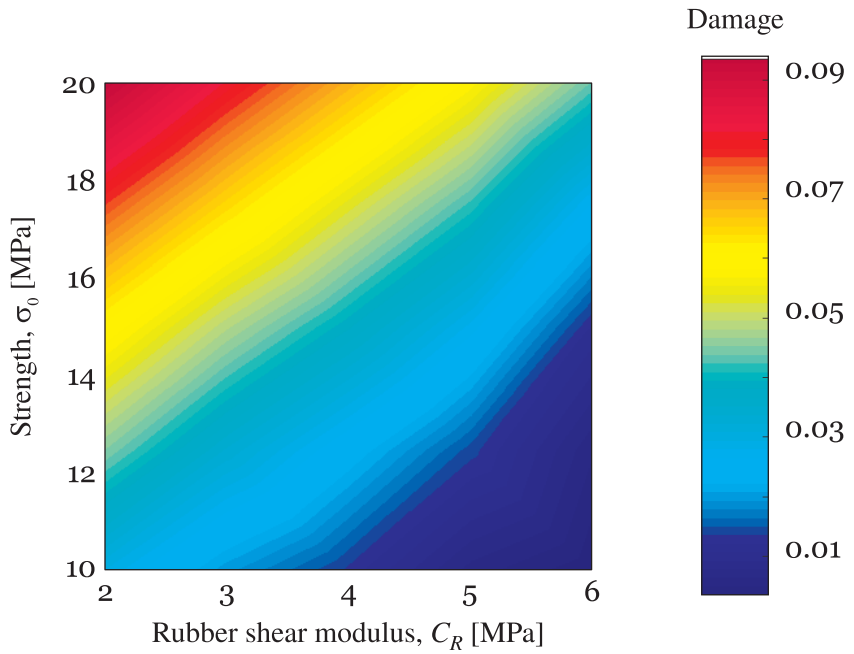

Figure 7.14: Effects of increasing rubber shear modulus and amorphous phase strength on the amorphous phase damage.

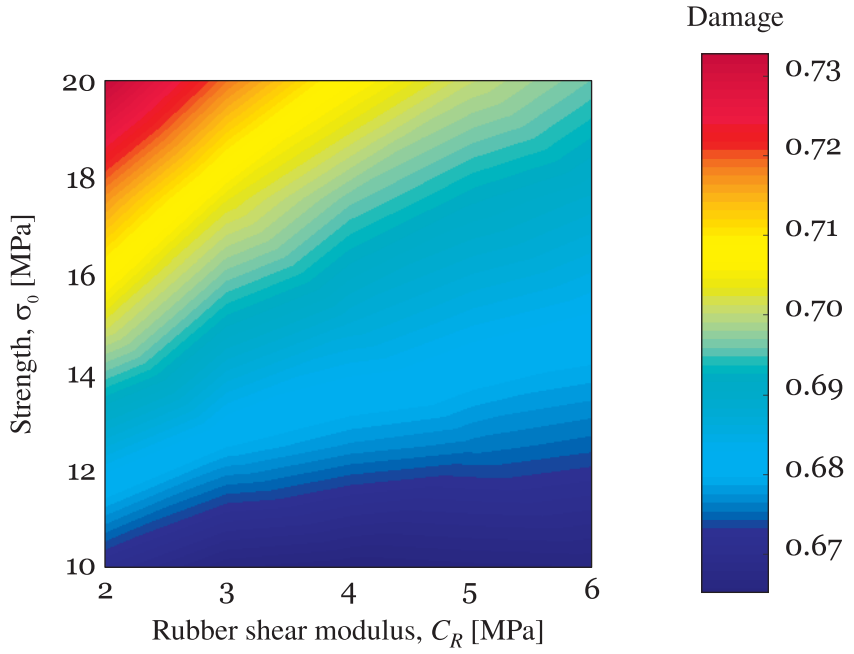

Figure 7.15: Effects of increasing rubber shear modulus and amorphous phase strength on the crystalline phase damage.

CHAPTER
EIGHT

Conclusions and recommendations

8.1 Conclusions

In this thesis, damage-based micromechanical models for high density polyethylene were proposed. The models predict the behaviour of polyethylene by relating mechanical properties and microstructure. Micromolecular parameters such as crystallinity, crystallite orientation, slip systems, and physical chain entanglements were considered in the formulations. Large deformation behaviour under uniaxial tension and simple shear was considered.

A three-dimensional micromechanical model considering progressive intracrystalline degradation was proposed in *Chapter* 4 to predict the overall stress-strain behaviour, texture evolution, and damage evolution in crystalline polyethylene. The governing constitutive equations were formulated considering the material microstructure. A damage mechanism based on the slip theory and an atomic debonding hypothesis was proposed to characterize the occurrence of crystal fragmentation. To incorporate damage on the constitutive equations, the so-called effective stress from Continuum Damage Mechanics was used. The stress-strain relationships at the microstructural level were derived in terms of a compliance tensor written as a damage and crystal orientation function. The resulting compliance tensor together with the assumed damage evolution and hardening laws provided the basic framework for the estimation of the effective behaviour of crystalline polyethylene.

To illustrate the proposed constitutive formulation, the model was used to predict the responses of the crystal aggregate under uniaxial tension and simple shear loading conditions. The results were compared with the experimental data reported by Hill-

mansen et al. (2000) for the uniaxial tension case and by G'Sell et al. (1983) for the simple shear case. Reasonable consistency is demonstrated between experimental curves and numerical simulations. The proposed model demonstrates that these types of damage constitutive models are appropriate for predicting large deformations and failure in polyethylene materials. It is believed that the discrepancies can be ascribed in part to the absence of the amorphous phase in the proposed formulation.

Aspects of the numerical implementation of the damage-coupled viscoplastic material law for crystalline polyethylene were addressed in *Chapter* 5. The governing constitutive equations were formulated considering the material microstructure as well as hardening and texture evolution. Incorporating a damage mechanics approach allowed to consider in the model the occurrence of crystal fragmentation. The material was represented as an aggregate of randomly oriented crystals. Representative numerical examples demonstrate the robustness of the proposed algorithms and the predictive capability of the model. The emphasis of the worked examples was placed on two aspects; first, the solution dependence on the number of crystals and loading direction, and second, the influence of the newly proposed material parameters on the description of the stress-strain behaviour and damage evolution.

The interplay between the material constituents is critical in the mechanical response of polyethylene. Therefore, in any mechanical analysis of polyethylene, it is essential to fully understand the deformation and failure mechanisms occurring at the microstructural level. In an attempt to expand the modelling capabilities of Lee et al.'s (1995) model, a new approach, which reflects the mechanical failure of the crystalline and amorphous phases, was proposed in *Chapter* 6. For the crystalline phase, a damage-coupled single crystal model based on the 100% crystalline formulation was chosen. Based on the concepts of Continuum Damage Mechanics, crystallite damage is assumed caused by the debonding of the crystallographic planes. On the other hand, for the amorphous phase, the constitutive model formulated within a thermodynamic framework tends to reproduce the different molecular configurations arising during the deformation process. Damage in amorphous polyethylene was seen as the appearance of material discontinuities which decrease the effective areas that transmit internal forces. The number density of active and inactive tie-molecules was considered to estimate the evolution of the fraction of discontinuities and the effective deviatoric stress. The corresponding damage evolution law was obtained by choosing a particular form based on internal energy and entropy. Besides the concepts behind the model, numerical simulations under uniaxial

tension and simple shear were performed and compared with experimental data previously obtained by Bartczak et al. (1994), G'Sell and Jonas (1981), G'Sell et al. (1983), and Li et al. (2001). The predictions obtained with the model show a consistently good agreement with the experimental results and a significant improvement with respect to the stress-strain predictions obtained by Lee et al. (1993b) and Nikolov et al. (2006).

In *Chapter* 7, a detailed explanation of the algorithms and numerical assumptions used to solve the constitutive equations of the semicrystalline approach was presented. The resolution of the so-called local and global problems was also described. For an unstrained state, the material was considered to be homogeneous and isotropic. An aggregate of inclusions was used to represent a material point. Each inclusion was assumed to be made of amorphous and crystalline material in perfect contact. The mechanical response of the equivalent homogenous medium was obtained by means of a volume average. To identify the influence of the most important parameters of the model, a series of simulations were completed. First, the influence of the number of rigid links and tilt angle on the stress-strain response was considered. Then, the influences of three sets of parameters; crystalline phase damage rate and release parameter, amorphous phase damage rate and saturation damage, and rubber shear modulus and amorphous phase strength, were reviewed. From the analysis on the influence of the tilt angle, it can be drawn that the model predictions are not sensitive to the values of the angle between the lamellar normal and the direction of polyethylene chains in the crystalline phase. Representative numerical examples demonstrate the influence of the material parameters on the description of the stress-strain and damage evolution in the crystalline and amorphous phases.

8.2 Recomendations

The proposed models should be regarded as a step forward for a better understanding of the mechanisms involved in inelastic deformation and degradation of polymers. Although the formulations adequately predict the material behaviour from a micromechanical viewpoint, many issues remain unsettled. The following comments list some general recommendations for future research derived from this thesis.

- Even though the proposed models were validated against experimental data obtained from samples of commercial polyethylene materials, the concepts and formulations presented herein could be extended to study mechanical damage in other

crystalline and semicrystalline polymeric materials

- The use of damage-coupled models to study creep in polymeric materials is a topic that can be explored further in order to analyze long term behaviour from a microscopic standpoint
- Although a general simple law that explains the mechanical behaviour of semicrystalline polyethylene is virtually inconceivable, the proposed models can be extended to include some important aspects not treated in this thesis, such as (1) elasticity and compressibility of the amorphous and crystalline phases, (2) contribution of the interaction among inclusions, (3) anisotropic damage of the amorphous phase, and (4) interdependence of damage evolution on the different slip systems
- Micromechanical modelling of polymers faces the challenge of efficiently representing the properties of crystalline and amorphous materials. The deformation behaviour of polyethylene materials depends in a rather complex manner on factors related to the morphology and loading conditions. Finding ingenious means to relate model parameters with physically measurable data is a major concern. For instance, small- or wide-angle scattering, or videometric testing systems should be used to observe the degradation processes occurring in the material as well as in both the crystalline and amorphous phases as inelastic deformations proceeds
- Efforts should be directed at improving computational efficiency. For instance, depending on the number of inclusions used, the models proposed herein can take from 2 to 8 hours of computing time. Parallel computing can be thought of as an alternative for the simultaneous execution of some of the programmed subroutines on multiple processors not only to reduce processing time but also to solve larger and more complex problems. Instead of solving a local problem after another, a practical option can be based on the fact that the process of solving the response of an aggregate at time t_n could be divided into smaller inclusion sets, which may be carried out concurrently

APPENDIX

A

Constitutive model summary for crystalline polyethylene (no amorphous phase)

Table A.1: Comparison between Parks and Ahzi's (1993b) and damage-coupled models for crystalline polyethylene

	Parks and Ahzi's model	**Damage-coupled model**
Stress-strain relationship	$D_{ij} = M_{ijkl} S_{lk}$	$D_{ij} = M_{ijkl} S_{lk}$
Compliance tensor	$M_{ijkl} = \dot{\gamma}_0 \sum_\alpha \frac{1}{g^\alpha} \left\lvert \frac{S^*_{mn} R^\alpha_{nm}}{g^\alpha} \right\rvert^{n-1} R^\alpha_{ij} R^\alpha_{kl}$	$M_{ijkl} = \dot{\gamma}_0 \sum_\alpha \frac{1}{(1-\Omega^\alpha) g^\alpha} \left\lvert \frac{S^*_{mn} R^\alpha_{nm}}{(1-\Omega^\alpha) g^\alpha} \right\rvert^{n-1} R^\alpha_{ij} R^\alpha_{kl}$
Damage evolution law	No damage	$\frac{d\Omega^\alpha}{d\tau^\alpha} = \dot{\Omega}_0 \left\lvert \frac{\tau^\alpha}{(1-\Omega^\alpha) g^\alpha} \right\rvert^m$ $\tau^\alpha = S^*_{ij} R^\alpha_{ji}$
Hardening evolution law	No hardening	$\dot{g}^\alpha = h \sum_\beta \dot{\gamma}^\beta$ $h = h_0 \operatorname{sech}^2(h_0 \hat{\gamma}/c)$ $\hat{\gamma} = \int_0^t \sqrt{2 \bar{D}_{ij} \bar{D}_{ij}}\, dt$
Total spin	$W_{ij} = W^m_{ij} + W^p_{lk}$	$W_{ij} = W^m_{ij} + R W^p_{lk}$ $R = \tanh(\zeta \bar{\Omega})$ $\bar{\Omega} = \frac{1}{8} \sum_\alpha \Omega^\alpha$

APPENDIX
B

Constitutive model summary for semicrystalline polyethylene (crystalline plus amorphous phases)

Table B.1: Comparison between Lee et al.'s (1993a) and damage-coupled models for semicrystalline polyethylene

	Lee et al.'s model	Damage-coupled model
Stress-strain relationship (Crystalline phase)	$D_{ij} = M_{ijkl} S_{lk}$	$D_{ij} = M_{ijkl} S_{lk}$
Compliance tensor	$M_{ijkl} = \dot{\gamma}_0 \sum_\alpha \frac{1}{g^\alpha} \left\lvert \frac{S^*_{mn} R^\alpha_{nm}}{g^\alpha} \right\rvert^{n-1} R^\alpha_{ij} R^\alpha_{kl}$	$M_{ijkl} = \dot{\gamma}_0 \sum_\alpha \frac{1}{(1-\Omega^\alpha) g^\alpha} \left\lvert \frac{S^*_{mn} R^\alpha_{nm}}{(1-\Omega^\alpha) g^\alpha} \right\rvert^{n-1} R^\alpha_{ij} R^\alpha_{kl}$
Damage evolution law	No damage	$\dot{\Omega}^\alpha = \dot{\Omega}_0 \left\lvert \frac{\tau^\alpha}{(1-\Omega^\alpha) g^\alpha} \right\rvert^m$ $\tau^\alpha = S^*_{ij} R^\alpha_{ji}$
Total spin	$W_{ij} = W^m_{ij} + W^p_{lk}$	$W_{ij} = W^m_{ij} + R W^p_{lk}$ $R = \tanh(\zeta \bar{\Omega})$ $\bar{\Omega} = \frac{1}{8} \sum_\alpha \Omega^\alpha$
Stress-strain relationship (Amorphous phase)	$D_{ij} = \frac{1}{2} \dot{\gamma}_0 \left(\frac{\sigma_{eq}}{\tau_0} \right)^{n^a - 1} \frac{S_{ij} - H'_{ij}}{\tau_0}$	$D_{ij} = \frac{3}{2} \dot{\epsilon}_0 \left(\frac{\sigma_{eq}}{\sigma_0} \right)^{n^a - 1} \frac{\frac{S_{ij}}{1-\Omega} - H'_{ij}}{\sigma_0}$
Hardening law	$H'_{ij} = \frac{C_R}{3} \sqrt{\frac{3N}{I_I}} \mathcal{L}^{-1} \left(\sqrt{\frac{I_I}{3N}} \right) (B_{ij} - \frac{1}{3} I_I I_{ij})$	$H'_{ij} = \frac{C_R}{3} \sqrt{\frac{3N}{I_I}} \mathcal{L}^{-1} \left(\sqrt{\frac{I_I}{3N}} \right) (B_{ij} - \frac{1}{3} I_I I_{ij})$
Damage evolution law	No damage	$\Omega = \Omega_\infty [1 - \exp(-\alpha W^2)]$

REFERENCES

Acharya, A. and Bassani, J. L. (2000). Lattice incompatibility and gradient theory of crystal plasticity. *Journal of the Mechanics and Physics of Solids*, 48:1565–1595.

Addiego, F., Dahoun, A., G'Sell, C., and Hiver, J. M. (2006). Characterization of volume strain at large deformation under uniaxial tension in high-density polyethylene. *Polymer*, 47:4387–4399.

Ahzi, S. (1999). Modelling of deformation plasticity and texture evolution in NiAl polycrystals. *Modelling and Simulation in Materials Science and Engineering*, 7:841–850.

Ahzi, S., Asaro, R. J., and Parks, D. M. (1993). Application of crystal plasticity theory for mechanically processed BSCCO superconductors. *Mechanics of Materials*, 15(3):201–222.

Ahzi, S., Lee, B. J., and Asaro, R. J. (1994). Plasticity and anisotropy evolution in crystalline polymers. *Materials Science and Engineering*, A189:35–44.

Ahzi, S., Parks, D. M., and Argon, A. S. (1990). Modeling of plastic deformation and evolution of anisotropy in semi–crystalline polymers. In Singh, B., Im, Y. T., Haque, I., and Altan, C., editors, *Computer Modeling and Simulation of Manufacturing Processes*, volume MD–Vol. 20/PED–Vol. 48, pages 287–292, New York. The American Society of Mechanical Engineers, ASME.

Alvarado-Contreras, J., Polak, M. A., and Penlidis, A. (2005). Damage modelling of polyethylene. In *2005 CSCE Conference*, pages GC185 1–10, Toronto.

Alvarado-Contreras, J., Polak, M. A., and Penlidis, A. (2006a). Simulation of crystalline polyethylene under tension and shear loading conditions. In Gámez, B., Ojeda, D., Larrazábal, G., and Cerraloza, C., editors, *Simulación y Modelado en Ingeniería y Ciencias*, pages M25–M31, Margarita Island – Venezuela. VIII International Congress

on Numerical Methods in Engineering and Applied Sciences, The Venezuelan Society of Numerical Methods in Engineering.

Alvarado-Contreras, J., Polak, M. A., and Penlidis, A. (2007a). Micromechanical approach to modeling damage in crystalline polyethylene. *Polymer Engineering and Science*, 47(4):410–420.

Alvarado-Contreras, J., Polak, M. A., and Penlidis, A. (2007b). Micromechanical approach to modeling damage in semicrystalline polyethylene. *In preparation*.

Alvarado-Contreras, J., Polak, M. A., and Penlidis, A. (2007c). Micromechanical modelling of damage at large deformation in semicrystalline polyethylene. In *Twenty-Ninth Annual Symposium on Polymer Science/Engineering*, Waterloo. Institute for Polymer Research - University of Waterloo.

Alvarado-Contreras, J., Polak, M. A., and Penlidis, A. (2008). Numerical simulation of damage at large deformation in semicrystalline polyethylene (*in preparation*). In *Simulación y Modelado en Ingeniería y Ciencias*, Margarita Island – Venezuela. IX International Congress on Numerical Methods in Engineering and Applied Sciences, The Venezuelan Society of Numerical Methods in Engineering.

Alvarado-Contreras, J. A., Liu, H., Polak, M. A., and Penlidis, A. (2006b). Micro- and macro-mechanical approaches for modelling of polyethylene material for pipes. In Pandey, M., Xie, W. C., and Xu, L., editors, *Advances in Engineering Structrures, Mechanics & Construction*, volume SMIA 140 of *Solid mechanics and its applications*, pages 449–458, The Netherlands. Springer.

Alvarado-Contreras, J. A., Polak, M. A., and Penlidis, A. (2007d). A computational procedure for a damage-coupled viscoplastic material law for semicrystalline polyethylene. *In preparation*.

Alvarado-Contreras, J. A., Polak, M. A., and Penlidis, A. (2007e). Computational study on a damage-coupled model for crystalline polyethylene. *Submitted for review*.

Andrews, E. H. (1972). The influence of morphology on the mechanical properties of crystalline polymers. *Pure and Applied Chemistry*, 31:91–109.

Angeles, J. (1988). *Rational Kinematics*. Springer–Verlag, New York.

Argon, A. S. (1973). Physical basis of distortional and dilational plastic flow in glassy polymers. *Journal of Macromolecular Science*, 8(3 & 4):573–596.

Argon, A. S. (1997). Morphological mechanism and kinetics of large–strain plastic deformation and evolution of texture in semicrystalline polymers. *Journal of Computer-Aided Materials Design*, 4:75–98.

Argon, A. S., Galeski, A., and Kazmierczak, T. (2005). Rate mechanisms of plasticity in semi–crystalline polyethylene. *Polymer*, 46:11798–11805.

Arruda, E. M. and Boyce, M. C. (1993). A three–dimensional constitutive model for the large stretch behavior of rubber elastic materials. *Journal of the Mechanics and Physics of Solids*, 41:389–412.

Arruda, E. M., Boyce, M. C., and Jayachandran, R. (1995). Effects of strain rate, temperature and thermomechanical coupling on the finite strain deformation of glassy polymers. *Mechanics of Materials*, 19:193–212.

Asaro, R. J. (1983). Micromechanics of crystals and polycrystals. *Advances in Applied Mechanics*, 23:1–111.

Asaro, R. J. and Needleman, A. (1985). Texture development and strain hardening in rate dependent polycrystals. *Acta Metallurgica*, 33:923–953.

Asaro, R. J. and Rice, J. R. (1977). Strain localization in ductile single crystals. *Journal of the Mechanics and Physics of Solids*, 25:309–338.

ASTM (2005). *Standard Specification for Polyethylene Plastics Extrusion Materials For Wire and Cable (ASTM D1248)*. American Society for Testing and Materials.

Bartczak, Z. (2002). Deformation of high-density polyethylene produced by rolling with side constraints. i. orientation behavior. *Journal of Applied Polymer Science*, 86(6):1396–1404.

Bartczak, Z. (2005a). Effect of chain entanglements of plastic deformation behavior of linear polyethylene. *Macromolecules*, 38:7702–7713.

Bartczak, Z. (2005b). Influence of molecular parameters on high-strain deformation of polyethylene in the plane-strain compression. part ii. strain recovery. *Polymer*, 46(23):10339–10354.

Bartczak, Z., Argon, A. S., and Cohen, R. E. (1992a). Deformation mechanisms and plastic resistance in single–crystal–textured high–density polyethylene. *Macromolecules*, 25:5036–5053.

Bartczak, Z., Argon, A. S., and Cohen, R. E. (1994). Texture evolution in large strain simple shear deformation of high density polyethylene. *Polymer*, 35:3427–3441.

Bartczak, Z., Cohen, R. E., and Argon, A. S. (1992b). Evolution of the crystalline texture of high–density polyethylene during uniaxial compression. *Macromolecules*, 25:4692–4704.

Bartczak, Z., Galeski, A., Argon, A. S., and Cohen, R. E. (1996a). On the plastic deformation of the amorphous component in semicrystalline polymers. *Polymer*, 37:2113–2123.

Bartczak, Z. and Kozanecki, M. (2005). Influence of molecular parameters on high-strain deformation of polyethylene in the plane–strain compression: Part I. Stress–strain behavior. *Polymer*, 46:8210–8221.

Bartczak, Z., Krashikova, N. P., and Galeski, A. (1996b). Morphology and texture of high–density polyethylene–polystyrene blens deformed by plane–strain compression. *Journal of Applied Polymer Science*, 62:167–179.

Bartczak, Z. and Lezak, E. (2005). Evolution of lamellar orientation and crystalline texture of various polyethylenes and ethylene–based copolymers in plane–strain compression. *Polymer*, 46:6050–6063.

Bassani, J. L. (1994). Plastic flow of crystals. *Advances in Applied Mechanics*, 30:191–258.

Bensason, S., Minick, J., Moet, A., Chum, S., Hiltner, A., and Baer, E. (1996). Classification of homogeneous ethylene–octene copolymers based on comonomer content. *Journal of Polymer Science*, B34:1301–1315.

Bevis, M. and Crellin, E. B. (1971). The geometry of twinning and phase transformations in crystalline polyethylene. *Polymer*, 12:666–684.

Bolotin, V. (1999). *Mechanics of Fatigue*. CRC Press, USA.

Bowden, P. B. and Young, R. J. (1974). Review: Deformation mechanisms in crystalline polymers. *Journal of Materials Science*, 9:2034–2051.

Boyce, M. A. and Arruda, E. M. (2000). Constitutive models of rubber elasticity: A review. *Rubber Chemistry and Technology*, 73:504–523.

Boyce, M. C., Parks, D. M., and Argon, A. S. (1988a). Large inelastic deformation of glassy polymers: Part I. Rate dependent constitutive model. *Mechanics of Materials*, 7:15–33.

Boyce, M. C., Parks, D. M., and Argon, A. S. (1988b). Large inelastic deformation of glassy polymers. Part II: Numerical simulation of hydrostatic extrusion. *Mechanics of Materials*, 7:35–47.

Boyce, M. C., Parks, D. M., and Argon, A. S. (1989). Plastic flow in oriented glassy polymers. *International Journal of Plasticity*, 5:593–615.

Brady, J. M. and Thomas, E. L. (1989). Deformation of oriented high density polyethylene shish-kebab films. *Journal of Materials Science*, 24(9):3311–3318.

Brown, N. and Ward, M. (1983). The influence of morphology and molecular weight on ductile-brittle transitions in linear polyethylene. *Journal of Materials Science*, 18(5):1405.

Budiansky, B. (1983). Micromechanics. *Computers and Structures*, 16:3–12.

Bunn, C. W. (1944). The crystal structure of ethylene. *Transactions of the Faraday Society*, 40:23–25.

Bunn, C. W. (1954). Molecular structure and the crystallinity of long–chain polymers. *Journal of Applied Physics*, 25(7):820–825.

Butler, M. F., Donald, A. M., and Ryan, A. J. (1997). Time resolved simultaneous small- and wide-angle x-ray scattering during polyethylene deformation: 1. cold drawing of ethylene-a-olefin copolymers. *Polymer*, 38(22):5521–5538.

Callister, W. (1996). *Materials Science and Engineering: An Introduction.* John Wiley and Sons, New York.

Capaccio, G. and Ward, I. (1975). Effect of molecular weight on the morphology and drawing behaviour of melt crystallized linear polyethylene. *Polymer*, 16(4):239–243.

Carr, S. H., Crist, B., and Marks, T. J. (1998). Structural basis for the mechanical properties of polyethylenes. Technical report, Defense Technical Information Center.

Cohen, A. (1991). A Padé approximant to the inverse Langevin function. *Rheologica Acta*, 30:270–273.

Cotton, J. D. and Kaufman, M. J. (1991). A simplified method for determining the number of independent slip systems in crystals. *Scripta Metallurgica et Materialia*, 25:2395–2398.

Cowking, A. and Rider, J. G. (1969). On molecular and textural reorientations in polyethylene caused by applied stress. *Journal of Materials Science*, 4:1051–1058.

Cowking, A., Rider, J. G., Hay, I. L., and Keller, A. (1968). A study on the orientation effects in polyethylene in the light of crystalline texture: Part 3. *Journal of Materials Science*, 3:646–654.

Craig, J. J. (1989). *Introduction to Robotics: Mechanics and Control*. Series in Electrical and Computer Engineering: Control Engineering. Addison–Wesley Publishing Company.

Dohrer, K. K., G., H. L., and Whiteman, N. F. (1988). Short chain branching distribution of uldpe. *Journal of Plastic Film and Sheeting*, 4:214–226.

Eyring, H. (1932). The resultant electric moment of complex molecules. *Physical Review*, 39(4):746–748.

Fanggao, C., Saunders, G. A., Hampton, R., Moody, S., and Clark, A. (1996). The effect of hydrostatic pressure and temperature on the permittivity of crosslinked polyethylene. In *Seventh International Conference on Dielectric Materials, Measurements and Applications*, pages 267–270.

Fellahi, S., Favis, B. D., and Fisa, B. (1995). Tensile dilatometry of injection-moulded HDPE/PA6 blends. *Journal of Materials Science*, 30(21):5522–5530.

Flory, P. (1988). *Statistical Mechanics of Chain Molecules*. Oxford University Press, New York.

Fotiu, P., H., I., and Zeigler, F. (1990). Dynamic plasticity: Strustural drift and modal projections. In W., S., editor, *Nonlinear Dynamics in Engineering Systems*, pages 75–82, Berlin. Springer-Verlag.

Frank, F. C., Keller, A., O'connor, A., and Wills, H. H. (1958). Deformation processes in polyethylene interpreted in terms of crystal plasticity. *Philosophical Magazine*, 3(25):64–74.

Galeski, A. and Bartczak, Z. (2003). Cavitation and cavity–free deformation of filled crystalline polymer systems. *Macromolecular Symposia*, 194:47–62.

Galeski, A., Bartczak, Z., Argon, A. S., and Cohen, R. E. (1992). Morphological alterations during texture–producing plastic plane strain compression of high–density polyethylene. *Macromolecules*, 25:5705–5718.

Groves, W. G. and Kelly, A. (1963). Independent slip systems in crystals. *Philosophical Magazine*, 8:877–887.

G'Sell, C., Boni, S., and Shrivastava, S. (1983). Application of the plane simple shear test for determination of the plastic behaviour of solid polymers at large strains. *Journal of Materials Science*, 18:903–918.

G'Sell, C. and Dahoun, A. (1994). Evolution of microstructure in semi–crystalline

polymer under large plastic deformation. *Materials Science and Engineering*, A175:183–199.

G'Sell, C., Hiver, J. M., and Dahoun, A. (2002). Experimental characterization of deformation damage in solid polymers under tension, and its interrelation with necking. *International Journal of Solids and Structures*, 39:3857–3872.

G'Sell, C. and Jonas, J. J. (1981). Yield and transient effects during the plastic deformation of solid polymers. *Journal of Materials Science*, 16(7):1956–1974.

Haward, R. N. and Thackray, G. (1968). The use of a mathematical model to describe isothermal stress–strain curves in glassy thermoplastics. *Proceedings of the Royal Society of London. Series A, Mathematical and Physical Sciences*, 302:453–472.

Hillmansen, S., Hobeika, S., Haward, R. N., and Leevers, P. S. (2000). The effect of strain rate, temperature, and molecular mass on the tensile deformation of polyethylene. *Polymer Engineering and Science*, 40:481–489.

Hiss, R., Hobeika, S., Lynn, C., and Strobl, G. (1999). Network stretching, slip processes, and fragmentation of crystallites during uniaxial drawing of polyethylene and related copolymers: A comparative study. *Macromolecules*, 32:4390–4403.

Hobeika, S., Men, Y., and Strobl, G. (2000). Temperature and strain rate independence of critical strains in polyethylene and poly(ethylene-co-vinyl acetate). *Macromolecules*, 33:1827–1833.

Horie, K., Barón, M., Fox, R. B., He, J., Hess, M., Kahovec, J., Kitayama, T., Kubisa, P., Maréchal, E., Mormann, W., Stepto, R. F. T., Tabak, D., Vohlídal, J., Wilks, E. S., and Work, W. J. (2004). Definitions of terms relating to reactions of polymers and to functional polymeric materials. *Pure and Applied Chemistry*, 76(4):889–906.

Hutchinson, J. W. (1970). Elastic-plastic behaviour of polycrystalline metals and composites. *Proceedings of the Royal Society of London. Series A, Mathematical and Physical Sciences*, 319:247–272.

Hutchinson, J. W. (1976). Bounds and self–consistent estimates for creep of polycrystalline materials. *Proceedings of the Royal Society of London. Series A, Mathematical and Physical Sciences*, 348:101–127.

Jenkins, A. D., Kratochvfl, P., Stepto, R. F. T., and Suter, U. W. (1996). Glossary of basic terms in polymer science. *Pure and Applied Chemistry*, 68(12):2287–2311.

Kachanov, L. M. (1958). Time of the rupture process under creep conditions. *Izvestiya Akademii Nauk SSSR*, 8:26–31.

Kachanov, L. M. (1986). *Introduction to Continuum Damage Mechanics*. Martinus Nijhoff Publishers, Amsterdam.

Kasatkin, B. S. and Grinyuk, V. D. (1968). Relationship between the fine structure of polyethylene and the mechanism of plstic deformation and fracture. *Mekhanika Polimerov*, 4(1):3–10.

Kazmierczak, T., Galeski, A., and Argon, A. S. (2005). Plastic deformation of polyethylene crystals as a function of crystal thickness and compression rate. *Polymer*, 46:8926–8936.

Keller, A. (1968). Polymer crystals. *Reports on Progress in Physics*, 31:623–704.

Keller, A. and Pope, D. P. (1971). Identification of structural processes in deformation of oriented polyethylene. *Journal of Materials Science*, 6:453–478.

Kelly, A., Groves, G., and Kidd, P. (2000). *Crystallography and Crystal Defects*. John Wiley & Sons Ltd.

Kim, B. K., Kim, M. S., Jeong, H. M., Kim, K. J., and Jang, J. K. (1992). Characterization of ultra low density polyethylenes (pe-uld). *Angewandte Makromolekulare Chemie*, 194:91–101.

Kitagawa, M., Onoda, T., and Mizutani, K. (1992). Stress-strain behaviour at finite strains for various strain paths in polyethylene. *Journal of Materials Science*, 27(1):13–23.

Krajcinovic, D. (1995). Continuum damage mechanics: when and how. *International Journal of Damage Mechanics*, 4:217–229.

Krajcinovic, D. (1996). *Damage Mechanics*. Elsevier Science, Amsterdam.

Krause, S. J. and Hosford, W. F. (1989). Texture development in polyethylene. i. uniaxial extension and uniaxial compression. *Journal of Polymer Science Part B: Polymer Physics*, 27(9):1853 – 1865.

Kurtz, S. (2004). *The UHMWPE Handbook: Ultra-High Molecular Weight Polyethylene in Total Joint Replacement*. Academic Press.

Lambert, F. L. (2002). Entropy is simple, qualitatively. *Journal of Chemical Eduation*, 79(10):1241–1246.

Lee, B. J., Ahzi, S., and Asaro, R. J. (1995). On the plasticity of low symmetry crystals lacking five independent slip systems. *Mechanics of Materials*, 20:1–8.

Lee, B. J., Argon, A. S., Parks, D. M., Ahzi, S., and Bartczak, Z. (1993a). Simulation of large strain plastic deformation and texture evolution in high density polyethylene. *Polymer*, 34:3555–3575.

Lee, B. J., Parks, D. M., and Ahzi, S. (1993b). Micromechanical modeling of large plastic deformation and texture evolution in semi-crystalline polymers. *Journal of the Mechanics and Physics of Solids*, 41:1651–1687.

Lee, E. H. (1969). Elasto–plastic deformation at finite strains. *Journal of Applied Mechanics*, 36:1–6.

Lee, S. Y., Bassett, D. C., and Olley, R. H. (2003). Lamellar deformation and its variation in drawn isolated polyethylene spherulites. *Polymer*, 44:5961–5967.

Lemaitre, J. (1984). How to use damage mechanics. *Nuclear Engineering and Design*, 80:233–245.

Lemaitre, J. (1996). *A Course on Damage Mechanics*. Springer-Verlag, Berlin.

Lemaitre, J. and Chaboche, J. L. (1994). *Mechanics of Solid Materials*. Cambridge University Press, Cambridge.

Lemaitre, J. and Dufailly, J. (1987). Damage measurements. *Engineering Fracture Mechanics*, 28:643–661.

Lequeu, P., Gilormini, P., Montheillet, F., Bacroix, B., and Jonas, J. J. (1987). Yield surfaces for textured polycrystals: I. Crystallographic approach. *Acta Metallurgica*, 35:439–451.

Lewis, G. (2001). Properties of crosslinked ultra-high-molecular-weight polyethylene. *Biomaterials*, 22(4):371–401.

Li, D., Garmestani, H., Kalidindi, S. R., and Alamo, R. (2001). Crystallographic texture evolution in high-density polyethylene during uniaxial tension. *Polymer*, 42(11):4903–4913.

Lin, L. and Argon, A. S. (1994). Review: Structure and plastic deformation of polyethylene. *Journal of Materials Science*, 29(2):294–323.

Lustiger, A. and Markham, R. L. (1983). Importance of tie molecules in preventing polyethylene fracture under long-term loading conditions. *Polymer*, 24:1647–1654.

Malvern, L. (1969). *Introduction to the Mechanics of a Continuous Medium*. Prentice-Hall, Inc, New Jersey. QA 808.2 M3 1969.

Morawiec, A. (2004). *Orientations and Rotations: Computations in Crystallographic Textures*. Springer, New York.

Nichetti, D. and Manas-Zloczower, I. (1999). Influence of molecular parameters on material processability in extrusion processes. *Polymer Engineering and Science*, 39(5):887–895.

Nicolis, G. and Prigogine, I. (1977). *Self-organization in Nonequilibrium Systems*. Wiley-Interscience.

Nikolov, S. and Doghri, I. (2000). A micro/macro constitutive model for small-deformation behavior of polyethylene. *Polymer*, 41:1883–1891.

Nikolov, S., Doghri, I., Pierard, O., Zealouk, L., and Goldberg, A. (2002). Multi-scale constitutive modeling of the small deformations of semi-crystalline polymers. *Journal of the Mechanics and Physics of Solids*, 50:2275–2302.

Nikolov, S., Lebensohn, R., and Raabe, D. (2006). Self-consistent modeling of large plastic deformation, texture and morphology evolution in semi-crystalline polymers. *Journal of the Mechanics and Physics of Solids*, 54:1350–1375.

Nitta, K. and Takayanagi, M. (2003). Novel proposal of lamellar clustering process for elucidation of tensile yield behavior of linear polyethylenes. *Journal of Macromolecular Science*, B42:107–126.

Pang, T. (2006). *An introduction to Computational Physics*. Cambridge University Press, New York.

Parks, D. M. and Ahzi, S. (1990). Polycrystalline plastic deformation and texture evolution for crystals lacking five independent slip systems. *Journal of the Mechanics and Physics of Solids*, 38:701–724.

Parks, D. M. and Ahzi, S. (1991). Micromechanical modeling of plasticity and texture evolution in semi–crystalline polymers. In Dvorak, G. J., editor, *Inelastic Deformation of Composite Materials*, pages 325–340, New York. International Union of Theoretical and Applied Mechanics, Springer-Verlag.

Perkins, W. G., Capiati, N. J., and Porter, R. S. (1976). The effect of molecular weight on the physical and mechanical properties of ultra-drawn high density polyethylene. *Polymer Engineering and Science*, 16(3):200–203.

Peterlin, A. (1971). Molecular model of drawing polyethylene and polypropylene. *Journal of Materials Science*, 6:490–508.

Pickover, B. H. (1983). Linear low density polyethylene: An overview. *Advances in Polymer Technology*, 3(3):271–275.

Popov, V. P. and Bal'tenas, R. A. (1974). Effect of the molecular and supramolecular structure of low pressure polyethylene on its mechanical properties. *Materials Science*, 7(6):680–682.

Rabotnov, Y. (1969). *Creep Problems in Structural Members*. North–Holland, Amsterdam.

Rennie, A. R. (1997). Building with snakes: the physics of long-chain molecules. *Physics Education*, 32:155–159.

Rosen, S. L. (1993). *Fundamental Principles of Polymeric Materials*. John Wiley and Sons, Inc, New York.

Russell, K. E., Hunter, B. K., and Heyding, R. D. (1997). Monoclinic polyethylene revisited. *Polymer*, 38(6):1409–1414.

Salençon, J. (2001). *Handbook of Continuum Mechanics. General Concepts Thermoelasticity*. Springer–Verlag Berlin Heidelberg, New York.

Sanchez-Palencia, E. and Zaoui, A., editors (1985). *Homogenization Techniques for Composite Media*. Springer–Verlag, Udine–Italy.

Schoenfeld, S. E., Ahzi, S., and Asaro, R. J. (1995). Elastic-plastic crystal mechanics for low symmetry crystals. *Journal of the Mechanics and Physics of Solids*, 43:415–446.

Schrauwen, B. A. G. (2003). *Deformation and failure of semicrystalline polymer systems: Influence of micro and molecular structure*. PhD thesis, Eindhoven University of Technology.

Schwarzenbach, D. (1996). *Crystallography*. John Wiley & Sons, West Sussex–England.

Séguéla, R. (2001). Dislocation approach to the plastic deformation of semicrystalline polymers: Kinematic aspects for polyethylene and polypropylene. *Journal of Polymer Science*, B40:593–601.

Shaw, M. and MacKnight, W. (2005). *Introduction to Polymer Viscoelasticity*. John Wiley & Sons.

Simo, J. and Hughes, T. (1998). *Computational Inelasticity*, volume 7 of *Interdisciplinary Applied Mathematics*. Springer, New York.

Takayanagi, M., Nitta, K., and Kojima, O. (2003). Application of lamellar clustering theory to isotactic polypropylene and direct observation of lamellar cluster morphology by electron microscopy. *Journal of Macromolecular Science*, B42(5):1049–1059.

Taylor, G. I. (1934). The mechanism of plastic deformation of crystals. Part I. Theoretical. *Proceedings of the Royal Society of London. Series A, Mathematical and Physical Sciences*, 145:362–387.

Tomita, Y. (2000). Constitutive modelling of deformation behavior of glassy polymers and applications. *International Journal of Mechanical Sciences*, 42:1455–1469.

Tomita, Y., Adachi, T., and Tanaka, S. (1997). Modelling and application of constitutive equation for glassy polymer based on nonaffine network theory. *European Journal of Mechanics - A/Solids*, 16:745–755.

Tomita, Y. and Uchida, M. (2003). Characterization of micro– to macroscopic deformation behavior of amorphous polymer with heterogeneous distribution of microstructures. *International Journal of Mechanical Sciences*, 45:1703–1716.

Treloar, L. R. (1975). *The Physics of Rubber Elasticity*. Oxford University Press, London.

Treloar, L. R. G. (1954). The photoelastic properties of short-chain molecular networks. *Transactions of the Faraday Society*, 50:881–896.

van Dommelen, J. A. W., Brekelmans, W. A. M., and Baaijens, F. P. T. (2000). Computational visco–plasticity for kinematically constrained crystals. *International Journal for Numerical Methods in Engineering*, 48:1311–1330.

van Dommelen, J. A. W., Brekelmans, W. A. M., and Govaert, L. E. (2007). Multiscale modelling of the mechanical behaviour of oriented semicrystalline polymers. *Material Science Forum*, 539-543:2607–2612.

van Dommelen, J. A. W., Parks, D. M., Boyce, M. C., Brekelmans, W. A. M., and Baaijens, F. P. T. (2003a). Micromechanical modeling of intraspherulitic deformation of semicrystalline polymers. *Polymer*, 44:6089–6101.

van Dommelen, J. A. W., Parks, D. M., Boyce, M. C., Brekelmans, W. A. M., and Baaijens, F. P. T. (2003b). Micromechanical modeling of the elasto–plastic behavior of semi–crystalline polymers. *Journal of the Mechanics and Physics of Solids*, 51:519–541.

van Dommelen, J. A. W., Schrauwen, B. A. G., Breemen, L. C. A., and Govaert, L. E. (2004). Micromechanical modeling of the tensile behavior of oriented polyethylene. *Journal of Polymer Science*, B42:2983–2994.

Wang, M. C. and Guth, E. (1952). Statistical theory of networks of non-Gaussian flexible chains. *Journal of Chemical Physics*, 20:1144–1157.

Wecker, S. M. (1975). Independent slip systems and the deformation behavior of semi-crystalline polymers. *Journal of Polymer Science*, B13:1651–1653.

Wissbrun, K. F. (1985). A model for domain flow of liquid-crystal polymers. *Faraday Discussions of the Chemical Society*, 79:161–173.

Xuejun, L., Mingrui, L., and Wenbin, H. (2001). Finite deformation elasto-plastic theory and consistent algorithm. *Acta Mechanica Solida Sinica*, 14(1):31–40.

Yamada, M., Miyasaka, K., and Ishikawa, K. (1971). Redrawing of oriented polyethylene film. *Journal of Polymer Science Part A-2: Polymer Physics*, 9(6):1083–1096.

Yang, W. and Chen, M. X. (2001). Modeling of large plastic deformation in crystalline polymers. *Journal of the Mechanics and Physics of Solids*, 49(11):2719–2736.

Young, R. J. (1981). *Introduction to Polymers*. Chapman and Hall, New York.

Young, R. J., Bowden, P. B., Ritchie, J. M., and Rider, J. G. (1973). Deformation mechanisms in oriented high-density polyethylene. *Journal of Materials Science*, 8(5):23–36.

Zbib, H. M. and Aifantis, E. C. (1988). On the concept of relative and plastic spins and its implications to large deformation theories. *Acta Mechanica*, 75:15–33.

Zheng, Q. S. and Betten, J. (1996). On damage effective stress and equivalent hypothesis. *International Journal of Damage Mechanics*, 5:219–240.

Zyczkowski, M. (2000). Creep damage evolution equation expressed in terms of dissipated power. *International Journal of Mechanical Sciences*, 42:755–769.